UNIVERSITY OF WARSAW

DOCTORAL THESIS

Hybrid systems of magnetic molecules and two-dimensional layered materials - theoretical and computational studies of stability, electronic, and magnetic properties

Author:
Aleksei KOSHEVARNIKOV

Supervisor:
Prof. dr hab. Jacek MAJEWSKI

A thesis submitted in fulfillment of the requirements for the degree of Doctor of Philosophy

in the

Institute of Theoretical Physics
Faculty of Physics

2022

Abstract

Hybrid systems of magnetic molecules and two-dimensional layered materials - theoretical and computational studies of stability, electronic, and magnetic properties

The magnetic tetrapyrrole molecules (such as porphyrins and phthalocyanines) with an active transition metal atom in their centre are currently intensively studied as prosperous potential elements of devices for high-density information storage and processing, It has been recently proved that by means of external factors one could induce two stable fully controllable molecular states. Therefore, hybrid systems consisting of such magnetic molecules and suitable carriers from family of two-dimensional materials are often considered as promising highly scalable spintronic systems that could in the near future lead to novel industrial applications.

The main goal of this dissertation is to provide understanding of physical mechanisms that determine the stability of such hybrid systems and shed light on their electronic and magnetic properties, on one hand, and deliver reliable quantitative predictions that could facilitate the design of devices, on the other hand. To reach this goal, the methodology based on the first-principles theory is necessary. The computations in the frameworks of the density functional theory (DFT) have been employed for issues of the hybrid systems' stability and morphology, and the multireference method going beyond the standard DFT has been used to study the magnetism in the hybrid systems. Two hybrid systems have been chosen as the case studies: iron phthalocyanine (FePc) on graphene, FePc/Graphene, and FePc on titanium carbide (Ti_2C) MXene magnetic 2D system, FePc/Ti_2C.

The FePc/Graphene hybrid system has been studied in the first part of the thesis. In these studies the adsorption of the FePc to pristine and defected graphene layer is investigated. We consider typical defects in graphene, such as Stone-Wales (SW) defect, substitutional impurities, of boron, nitrogen, and sulphur, and also complex defects involving SW defect and B, N, and S impurities in its interior. We determine first the stability and geometry of these defects in graphene, and then we study whether these defects can facilitate the adsorption of FePc, and finally the defect induced modifications of the electronic and magnetic properties of the hybrid systems.

The DFT studies of the FePc/Graphene hybrid systems have been carried out within two types of boundary conditions: (i) superlattice geometry with periodic boundary conditions, and (ii) cluster geometry, where the carbon dangling bonds at the edges of the graphene layer are saturated with hydrogen atoms. In the case of superlattice and cluster geometries, the numerical packages *Quantum Espresso* and *ORCA* have been employed, respectively. We observe fairly good agreement between geometries of the studied systems as obtained with two kinds of boundary conditions. This allows us to use the results obtained with the DFT calculation involving the cluster boundary conditions as a starting point for studies of excited states employing multireference methods, which is a prerequisite of the correct description of the magnetic states of the FePc/Graphene hybrid system.

For the multireference calculations, the graphene layer has been mimicked by pyrene molecule consisting of four carbon hexagons. This concept makes it possible for the first time to go beyond the one-determinant approximation in studies of such complex system as the FePc/Graphene hybrid structures, even with very restricted computer resources available. As it turns out, in systems with B and N impurities, only multi-reference method leads to reliable results.

In the second part of the thesis, we perform the spin polarised DFT studies of FePc/Ti_2C hybrid system. The most relevant issue in this part is the interaction between magnetic atoms: Ti from MXene substrate and Fe from phthalocyanine. Four various magnetic configurations of FePc/Ti_2C have been considered. The significant ferromagnetic interaction between the iron atom and the upper titanium layer plays important role in the reorientation of the iron atom magnetic moment. We also analyse a model of the system in which the FePc molecule is in a quintet state (the ground state of an isolated molecule is a triplet). To get a better understanding of the physics of the FePc/Ti_2C hybrid system, we also study the hybrid systems with single iron atom and non-magnetic H_2 phthalocyanine on the Ti_2C layer, Fe/Ti_2C and H_2Pc/Ti_2C, respectively, which nicely explains the role of the Pc ligand in the FePc/Ti_2C hybrid system.

Streszczenie

Układy hybrydowe molekuł magnetycznych i materiałów dwuwymiarowych - badania teoretyczne i obliczeniowe stabilności właściwości elektronowych i magnetycznych

Magnetyczne cząsteczki tetrapirolu (takie jak porfiryny i ftalocyjaniny) z aktywnym atomem metalu przejściowego w centrum są obecnie intensywnie badane jako potencjalne elementy urządzeń do przechowywania i przetwarzania informacji o dużej gęstości. Ostatnio pokazano, że w takich molekułach można indukować dwa stabilne, kontrolowane czynnikiem zewnętrznym stany magnetyczne. Układy hybrydowe składające się z takich cząsteczek magnetycznych i odpowiedniego podłoża na bazie dwuwymiarowych materiałów są powszechnie uważane za obiecujące, wysoce skalowalne układy spintroniczne, które mogą w niedalekiej przyszłości doprowadzić do nowych zastosowań.

Celem niniejszej pracy doktorskiej jest zrozumienie mechanizmów fizycznych determinujących stabilność oraz własności elektronowe i magnetyczne takich układów hybrydowych oraz dostarczenie wiarygodnych ilościowych przewidywań teoretycznych, które mogłyby pomóc w projektowaniu urządzeń na bazie takich układów hybrydowych. Osiągnięcie postawionego w dysertacji celu wymaga zastosowania metod z pierwszych zasad. Obliczenia na bazie teorii funkcjonału gęstości (DFT) zastosowano do zbadania stabilności, morfologii , oraz własności układów hybrydowych. Dodatkowo do zbadania własności magnetycznych układów hybrydowych zastosowano metodę wielokonfiguracyjną, wychodzącą poza standardowe obliczenia w ramach teorii DFT. W pracy doktorskiej rozważano dwa prototypowe układy hybrydowe, które ilustrują ważne dla tych układów zagadnienia fizyczne. Jako pierwszy układ wybrano ftalocyjaninę z centralnym atomem żelaza (FePc) na niemagnetycznym podłożu grafenu (FePc/Grafen), a drugim badanym układem hybrydowym była molekuła FePc na podłożu trójwarstwowego karbidka tytanu (Ti_2C) MXenes - FePc/Ti_2C.

Układ hybrydowy FePc/Grafen badano w pierwszej części pracy, gdzie rozważano adsorpcję molekuły FePc na grafenie idealnym i grafenie z typowymi defektami. Przeprowadzono obliczenia dla defektu Stone-Wales (SW), podstawieniowych domieszek boru, azotu, i siarki, oraz defektów złożonych, gdzie w rdzeniu defektu SW podstawiono dodatkowo domieszkę B, N, lub S w miejsce atomu węgla. Najpierw przeanalizowano stabilność defektów w grafenie, a następnie stabilność układów hybrydowych z czystym grafenem oraz grafenem z defektami. Sprawdzono czy adsorpcja FePc w okolicach defektu jest silniejsza oraz jak obecność defektów w grafenie wpływa na własności elektronowe i magnetyczne układów hybrydowych.

Obliczenia DFT dla układów hybrydowych FePc/Grafen zostały przeprowadzone stosując dwa rodzaje warunków brzegowych: (i) geometria supersieci z periodycznymi warunkami brzegowymi, oraz (ii) geometria klastra, gdzie zerwane wiązania w węglach na brzegu klastra zostały wysycone atomami wodoru. W przypadku obliczeń w geometrii supersieci zastosowano pakiet numeryczny *Quantum Espresso*, a w przypadku obliczeń klastrowych pakiet *ORCA*. Obliczenia z zastosowaniem obu typów warunków brzegowych prowadzą do dobrej zgodności w przewidywanej geometrii układów hybrydowych. Pozwala to na wykorzystanie wyników uzyskanych w warunkach brzegowych typu klaster jako punktu wyjścia

do badań stanów wzbudzonych metodami wieloreferencyjnymi, co, jak się okazuje, jest warunkiem prawidłowego opisu stanów magnetycznych układu hybrydowego FePc/Grafen.

W obliczeniach wieloreferencyjnych układów hybrydowych podłoże grafenowe było reprezentowane przez molekułę pirenu składającą się z czterech sześciokątów węglowych. Zastosowanie takiego uproszczonego modelu podłoża pozwala po raz pierwszy na wykonanie obliczeń wielokonfiguracyjnych dla hybrydowego sytemu FePc/Grafen i wyjście poza przybliżenie stanu wieloelektronowego jednym wyznacznikiem Slatera, nawet dysponując bardzo ograniczonymi zasobami komputerowymi. W układów hybrydowych zawierających domieszki B i N, tylko obliczenia wieloreferencyjne prowadzą do poprawnych wyników.

W drugiej części pracy, wykonano spinowe spolaryzowane obliczenia DFT dla układu hybrydowego FePc/Ti_2C. Tutaj najważniejszym zagadnieniem jest oddziaływanie między magnetycznymi atomami Ti z warstwy podłoża oraz atomem Fe z ftalocyjaniny. Rozważono struktury z czterema różnymi konfiguracjami momentów magnetycznych atomu Fe i dwóch warstw tytanowych. Oddziaływanie ferromagnetyczne między atomem żelaza a górną warstwą tytanu odgrywa ważną rolę w reorientacji momentu magnetycznego atomu żelaza. Przeanalizowano również model układu, w którym cząsteczka FePc jest w stanie kwintetowym (podczas gdy stanem podstawowym wyizolowanej cząsteczki jest tryplet). Dla lepszego zrozumienia fizyki układu hybrydowego FePc/Ti_2C, przeprowadzono również obliczenia dla układów hybrydowych złożonych z pojedynczego atomu żelaza oraz niemagnetycznej molekuły H_2Pc na podłożu Ti_2C, odpowiednio Fe/Ti_2C oraz H_2Pc/Ti_2C, stwierdzając dominującą rolę Pc w stabilizacji FePc/Ti_2C.

Acknowledgements

I would like to acknowledge all the people who contributed to the fact that this thesis was done and published.

First of all, I want to thank my supervisor, prof. dr hab. Jacek Majewski, for valuable advice, support and endless patience. The professor's approach to students incredibly develops self-discipline and responsibility. I would like to acknowledge prof. dr hab. Jacek Majewski for providing guidance through the complicated world of material science.

I would like to thank dr Alexandra Siklitskaia for recommending me to choose this project. Dr Alexandra Siklitskaia shared her scientific experience, helped me out in difficult situations, and gave friendly advice. Dr Manel Mabrouk and dr Tomi Ketolainen worked with me in the same group as postdocs and I am grateful to them for the exchange of experience.

My gratitude extends to the University of Warsaw. Of course, this is the University of a very high level and it was an honour to study there. The faculty of Physics is on the cutting-edge of science and is an incredible source of inspiration. I am grateful to the Polonicum centre. Thanks to them, I was able to write the thesis abstract in Polish on my own. Thanks to the PhD student community for litres of coffee and informative conversations in the social space.

Finally, I would like to thank my family and friends for their support and belief in me.

This research has been supported by the National Science Centre, within the OPUS 12 grant (UMO-2016/23/B/ST3/03567).

Contents

List of Figures

List of Tables

List of Abbreviations

2D	two-dimensional
AE	All electron
AO	Atomic orbitals
CAS(N,M)	Complete active space with M orbitals and N electrons
CASSCF	Complete active space self-consistent field
CI	Configurational interaction
D3	Grimme dispersion correction
def2	Second-generation default Karlsruhe basis set
DFT	Density functional theory
DFT+U	Hubbard model of an orbital-dependent correction to DFT potentials
DOS	Density of states
Fcc	Face-centered cubic
GGA	generalised gradient approximation
Hcp	Hexagonal closest packed
HF	Hartree-Fock
HOMO	Highest occupied molecular orbital
KS	Kohn-Sham
LCAO	Linear combination of atomic orbitals
LDA	Local density approximation
LUMO	Lowest unoccupied molecular orbital
MCSCF	multi-configurational self-consistent field
miRNA	Micro ribonucleic acid
NEVPT	n-electron Valence State Perturbation Theory
NEVPT2	Second order n-electron Valence State Perturbation Theory
OLED	organic light-emitting diode
PAW	Projected augmented waves
PBE	Perdew-Burke-Ernzerhof functional
Pc	Phthalocyanine
PDOS	Projected density of states
QE	Quantum Espresso
RAM	Random access memory
RHF	Restricted Hartree-Fock
RI	Repulsion integrals
RKS	Restricted Kohn-Sham
STM	Scanning tunnelling microscope
SVP	Polarised valence double-zeta basis set
SW	The Stone-Wales defect
TM	Transition metal
TZVPD	Diffuse polarised valence triple-zeta basis set
TZVPPD	Diffuse doubly polarised valence triple-zeta basis set
UHF	Unrestricted Hartree-Fock
UKS	Unrestricted Kohn-Sham

USPP	Ultrasoft pseudopotentials
VDW	van der Waals
XC	Exchange correlation

Chapter 1

Introduction

The modern technology industry is hard at work developing and fabrication ever-smaller storage devices. The pace of this miniaturisation has already led to modern semiconductor memory devices with a unit cell size of about 10 nm.[1] However, such size is not considered as a limit, and systems for smaller cells are pursued intensively.

In general, the operation of the memory device can be based on any physical effect that brings the system to two or more stable states. For example, single-molecule magnets exhibit magnetic hysteresis below a certain temperature.[2] These molecules are approximately 1 to 2 nm in size, which makes the ordered structure of such elements incredibly attractive as systems for the computer memory.

A substrate for planting such organometallic molecules is important, since upon contact the magnetic properties of molecules can change for better or worse. The nature of the adhesion and the change of molecules morphology also depend on the properties of the substrate. In thiss thesis, we will study the interaction of a magnetic organometallic FePc molecule on two-dimensional surfaces. Such structures are quite compact; their thickness is especially attractive; so they are actively studied for use in modern spintronic devices.

1.1 Background

1.1.1 Transition Metal Phthalocyanines

Transition metal phthalocyanines (TMPc's) (Fig. 1.1) are widely known class of tetrapyrrole organometallic compounds that have been well known since the 1930s.[3] They consist of isoindole rings interconnected via an sp^2-hybridized nitrogen atom and a transition metal atom in the centre. The first commercial implementation of these compounds was as a blue pigment. Over the years, this type of molecule has attracted attention of researchers in the field of molecular electronics. The ease of preparation, the simple molecular structure, and the possibility of functionalisation have made TMPc's one of the leading species for applications in the modern fields of spintronics and optoelectronics.[4, 5, 6] Such molecules can also act as a part of an organic photodetector,[7] and as a hole injection layer in OLED displays.[8]

1.1.2 2D materials

In the first half of the 20th century, it was thought that two-dimensional (2D) crystal structures [9] are thermodynamically unstable and cannot exist. However, theoretical discoveries in the field of solid state physics cast doubt on this point of view, and in the 21st century, the first 2D material was experimentally obtained.[10] The discovery and synthesis of dozens of new 2D materials have followed quickly.[**prasad2021introduction**

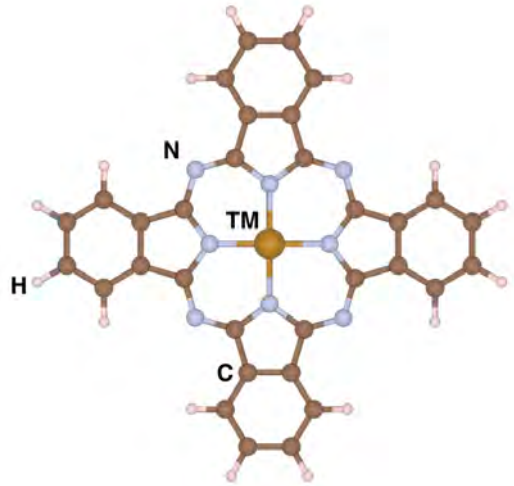

FIGURE 1.1: TMPc molecule.

The family of these planar materials includes systems being just a single atomic layer (e.g. graphene, silicene, black phosphorus) or structures consisting of a few atomic layers (e.g. MXenes, TM-dichalcogenides). Aditionally, it has been possible to obtain lateral and vertical heterostructures consisting of several 2D materials.[**wang2014two**] The vastness of this topic does not allow us to include a broader discussion of 2D-materials issues into this thesis. Therefore, we limit ourselves to description of the materials studied as substrates in the thesis.

Graphene

Graphene (Fig. 1.2) is a layer of one carbon atom thick, consisting of condensed six-membered rings, constituing a honeycomb lattice. Carbon atoms in graphene are linked by sp^2-bonds in a hexagonal two-dimensional (2D) lattice. The first description of the production of graphene was published in 2004.[10] A separate layer of graphene was obtained by mechanical peeling a graphite rod on a silicon dioxide surface. Graphite is a multilayer structure of graphene layers interconnected by weak van der Waals forces. Graphene flakes chipped off from graphite remain on the SiO_2 surface. The thickness of the atomic layers of graphene can be checked by the interference pattern of an optical microscope. In turn, the SiO_2 surface mechanically stabilises the monatomic layers of graphene.

Currently, there exist several sophisticated methods to obtain graphene. The most common are:

- *Exfoliated graphene.*[11] The same technique by which the first graphene was obtained. The undoubted advantage of this technique today is to obtain the highest quality graphene monolayer. Such samples are ideally suited for perfoming experiments on electronic properties of graphene, for measuring its conductivity, or creating prototypes of graphene-based devices, for example, a quantum transistor. The only and very significant drawback of this method is the lack of the possibility of use for large-scale production of graphene, because of the specific feature of the method, namely, the need for manual work.

- *Chemical graphene.*[12] This method implies several possible options for the preparation of suspensions containing graphene. The earliest chemical method

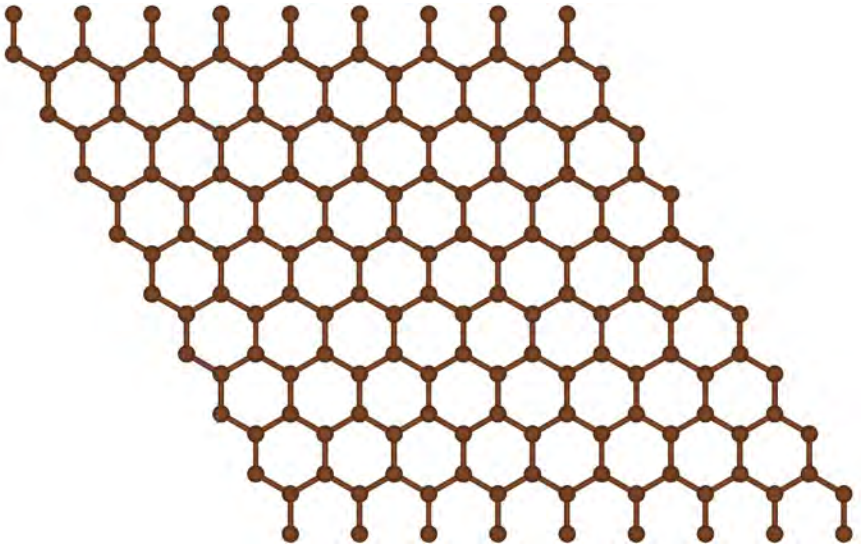

FIGURE 1.2: Graphene.

is considered to be the production of graphene by the reduction of graphite oxide. Another type of chemical method for producing graphene is the liquid phase separation of graphite.

- *Epitaxial graphene on metals*[13] *or SiC.*[14] At temperatures greater than 1000 °C, in the presence of any carbon source as a result of the chemical precipitation of carbon from the gas phase, the metal is saturated. Furthermore, in high or ultra-high vacuum, at pressure of the order of the 10^{-10} mbar, lowering of the substrate's temperature causes the solubility of carbon in the metal to drop significantly. The carbon atoms reach the surface and form graphene domains of a large area.

- *Chemical vapour deposition (CVD) graphene.*[15] In this process, vapours of one or more substances react in the chamber, decompose and then form a layer of the required substance on the substrate. This method makes it possible to synthesise the largest layers of graphene.[16]

Graphene is famous for its extraordinary physical properties.[17] The valence and the conduction bands touch in one *k*-point, making graphene a semimetal with unusual electronic properties. Charge transport in graphene can be ballistic over long distances. Graphene conducts heat and electricity very efficiently along its plane. The material strongly absorbs light of all visible wavelengths; however, a single sheet of graphene is almost transparent due to its extreme thinness. Graphene is also many times stronger than other materials of similar thickness.

MXenes Family and its Generic Representative Ti_2C

MXene is a class of 2D compounds obtained from MAX phases (layered hexagonal carbides or nitrides with a formula $M_{n+1}AX_n$, where n=1-3, M indicates a transitional metal, A - elements mostly from groups 13 and 14, and Xs are C or N atoms) by etching A elements. Firstly discovered experimentally in 2011,[18] this class of compounds has been developed rapidly. A lot of new species and their functionalised derivatives have been synthesised. Soon potential applications in thermoelectricity, catalysis, and energy storage have been found.[19, 20] Here, we are interested in the

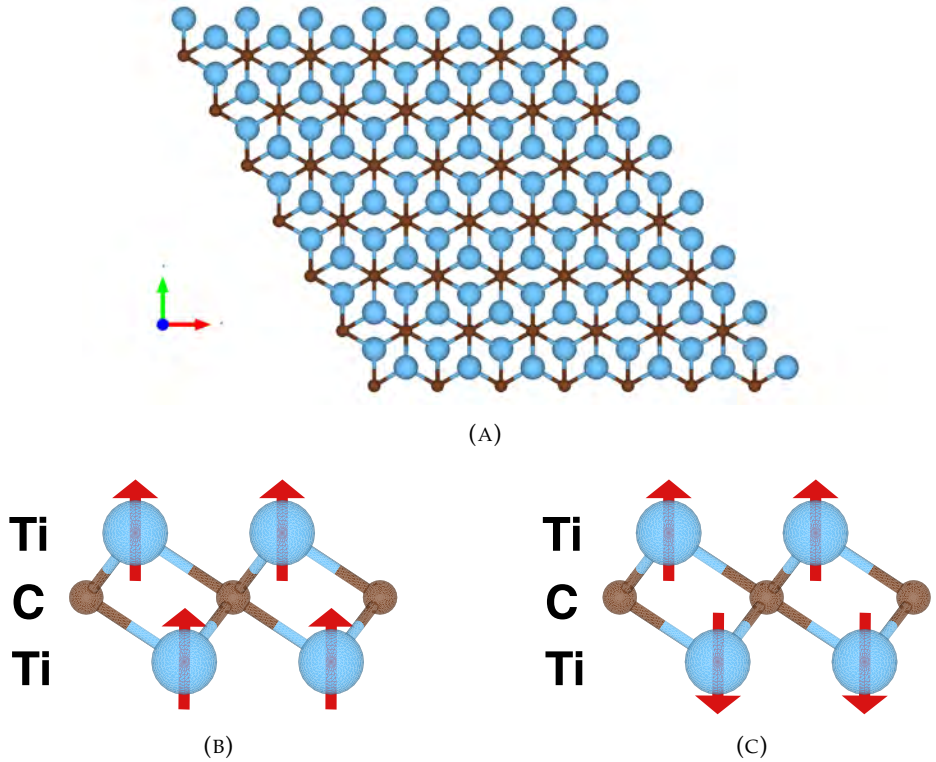

(A) (B) (C)

FIGURE 1.3: The Ti_2C 2D-three-layered system: (a) view from above; and side views of (b) ferromagnetic and (c) antiferromagnetic configurations. Red arrows indicate the internal magnetic moment of Ti atoms.

magnetic properties of MXenes and especially of the Ti_2C (Fig. 1.3). It was shown [21] that this layer exhibits several magnetic configurations where the most stable are the configurations with co-directional (ferromagnetic, Fig. 1.3B) and counter-directional (antiferromagnetic, 1.3C) magnetic moments of the Ti sublayers. The energy of the antiferromagnetic configuration is predicted to be lower just by 10 meV per primitive cell.

1.1.3 TMPc on 2D materials

Recent studies have shown the possibility of changing the magnetisation of a single metal-organic molecule. The control of the magnetic moment of the MnPc molecule lying on the $BiAg_2$ nanostructure using an external electric field was demonstrated.[22] It was theoretically predicted that control of the spin state of a structurally similar iron porphyrin molecule by stretching and compressing a graphene substrate would be also possible.[23] In both studies, the central metal atom has two adaptive states with different magnetic moments. Computational predictions [24] also indicate that ZrPc or HfPc deposited on the graphene/Ni(111) substrate have two different structural conformations, for which the molecules attain different magnetic states depending on the position of the centre metallic ion, either above the Pc or between the Pc and the substrate. Such bistability lets us to represent these molecules as elementary keepers of a bit of information. Creating a controlled array of such molecules will bring us closer to creating a storage device based on single-molecular excitations, which in turn will lead to a significant increase in the density of information.

Recently, the TMPc/2D-material hybrid structures have also been actively investigated as catalysts for redox reactions. The emerging field of hydrogen energetics needs cheaper catalysts for fuel cells to reduce the cost of commercial production. Currently, the most popular catalysts are based on platinum group metals,[25] and the cost of producing such cells is quite high. Recent laboratory studies already show that the use of the FePc/2D materials hybrid structures shows a higher specific activity of redox reactions. In such catalysts, the iron atom is used as a centre for trapping oxygen. Then, this atomic oxygen attaches to itself two protons (the result of the splitting of a hydrogen molecule) and forms water. Among 2D materials, the best results were obtained using $Ti_3C_2T_2$ [26] (where T are functional groups adsorbed to MXene from the atmosphere), but there are also many studies with graphene as a substrate for FePc molecules.[27, 28]

Also, FePc/Graphene hybrid structures can be tuned in various ways. The use of substituents on the periphery of the phthalocyanine isoindole rings helps to change the electron density around the central iron atom.[29] Si-FePc-Graphene sandwich structures [30] can also serve as catalysts, with the outer graphene layer protecting the device from external poisons. Axial Fe-O coordination improves oxygen adsorption and thus increases redox productivity.[31] The use of defects in the graphene layer increases the catalytic efficiency of the elements. For example, FePc/Graphene systems with nitrogen impurities on the surface demonstrated [32] better specific activity than platinum catalysts, while such systems were characterised by a higher current density.

The interaction between graphene and TMPc molecules is fairly well understood. The results show that phthalocyanine molecules are attracted to the surface by van der Waals forces, and the electronic configuration of metal atoms in the centre does not change significantly. The presence of the TMPc molecule does not open the graphene band gap.[33] FePc and CoPc molecules on the top of MoS_2 and graphene 2D layers were studied theoretically [34] and it was found that while the adsorption energy of a molecule to a surface in the MoS_2 cases is about 2.5 eV higher than in the graphene cases, both layers do not significantly change magnetic anisotropy parameters and metallic *d*-orbitals distributions. When using graphene as a layer between the FePc molecule and a metal surface, graphene weakens their ferromagnetic interaction.[35]

In experiments, FePc molecules found on pure graphene tend to form self-connecting structures based on the attraction of molecules to each other by van der Waals forces.[36] For artificial isolation of a single molecule from the film, injection of defects on graphene can be used. Theoretical calculations of the FePc molecule adsorped to the defected graphene were carried out for single vacancy, double vacancy,[37] and (B, N, S)-dopings,[38] whereas the N-doping was also experimentally studied.[36] The above studies show a little bit higher adsorption energy of FePc to defected graphene compared to pristine graphene. Scanning tunnelling microscopy images clearly show the FePc molecule adsorped on top of a defect. Moreover, it turns out that the magnetic moment of the system depends on the type of defect. In particular, B-dopants induce the increase of the magnetic moment, N-doping leads to decrease of the magnetic moment, whereas introducing of S impurities causes the quenching the magnetic moment.

In the literature, a similar interaction of TMPc molecules with a Stone-Wales defect [39] in graphene was considered. This defect (Fig. 1.4), which consists of two pairs of five and seven carbon polygons, occurs due to the rotation of two adjacent carbon atoms relative to their centre by 90 degrees. Thus, when a defect is formed, there is no change in the chemical composition of the material. This fact may lead to

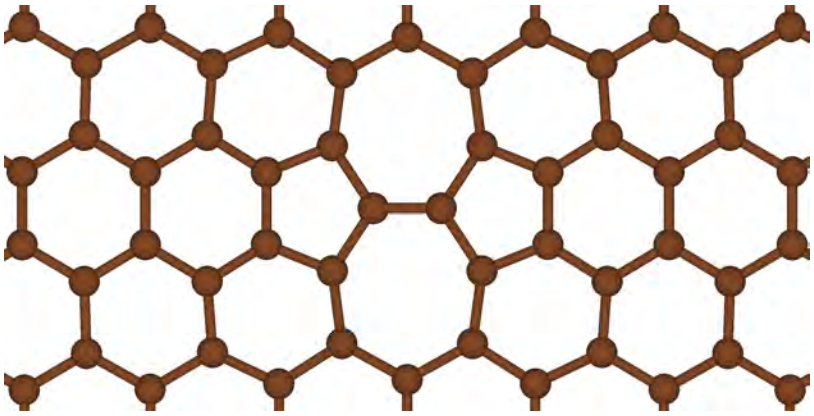

FIGURE 1.4: The Stone-Wales defect in graphene.

the idea of maintaining the magnetic moment of the TMPc - defected graphene system. The adsorption energy of TMPc to graphene with the Stone-Wales defect was calculated [40] to be 6% higher for Zn as TM in TMPc and 10% higher for Cu. Studies of the iron porphyrin/graphene/Ni(111) revealed [41] that when the Stone-Wales defect is formed the graphene layer is not flat anymore, just exhibiting a wavelike shape.

1.1.4 Metals on MXenes

Because MXenes are relatively new materials, there are not many quantum-chemical studies of the adsorption of molecules on a MXene's surface. Experimental studies of such systems are hampered by the fact that the outer layers of the material adsorb substances from the atmosphere, changing their chemical structure. Experimental studies of TMPc/MXene hybrid systems were carried out taking into account that the surface is saturated by atmospheric functional groups. In these cases, MXenes lose their magnetic properties. Nonetheless, the FePc/$Ti_3C_2T_2$ system was found to be a good catalyst for redox reactions.[26] In addition, the same complex works well in determining miRNAs and diagnosis of cancer biomarkers.[42] Computational studies of MXenes have gone further than experimental ones. Quantum-chemical methods make it possible to investigate compounds that are still difficult to obtain experimentally.

Theoretical studies of organometallic molecules on MXene surfaces were not found in the literature, but there are several theoretical studies devoted to the adsorption of atoms on the surface of Ti_2C and Ti_3C_2 2D MXene layers. It was found [43] that the adsorption energies of 3d, 4d, and 5d transition metal atoms on Ti_3C_2 are in the range of -7.98 to -1.05 eV. 3d-transition metals on M_2C layers (M = Ti, V, Cr, Zr, Nb, Mo, Hf, Ta, and W) were studied [44] as single-atom catalysts to find an alternative to Pt-based catalysts. Also, there are studies about metal atoms on functionalised layers for single-atom catalysts [45, 46] and Li-ion storage.[47] It should be noted that these studies did not take into account the spin polarisation of surfaces. The results of the studies are presented in Table 1.1. The calculation parameters given in parentheses will be explained in the next chapter.

1.1.5 Metals on Surfaces

Determination of the magnetic moment of each atom in a system is possible using spin-polarised scanning tunnelling microscopy.[48, 49, 50] In these works, the Fe

	Adsorption Energy, eV	Fe height from the layer, Å	μ(Fe)
Fe on Ti_3C_2 (PBE)[43]	Hcp: -3.849	Hcp: 2.373	—
	Fcc: -3.847	Fcc: 2.360	—
Fe on Ti_2C (PBE+D3)[44]	Hcp: -4.093	Hcp: 1.708	Hcp: -2.03
	Fcc: -3.897	Fcc: 1.644	Fcc: -2.28

TABLE 1.1: Energetic, geometric and magnetic characteristics of TM/MXene hybrid systems Fe/Ti_2C and Fe/Ti_3C_2. The sources of the data are indicated. Adsorption sites for Ti_3C_2: Hcp - on the higher C-atom, Fcc - on the middle Ti; for Ti_2C: Hcp and Fcc - on the bottom Ti, but with different symmetry surrounding.

atom was studied in the interaction with InSb(110) surface. In this study, the iron atom falls into the surface due to the large lattice constant. In the case of the iron atom on top of the Cu(001) surface, it was shown [51] that the electronic and magnetic properties of adatoms are strongly affected by the tip-surface distance.

In the purely theoretical study of iron chains on Cu(001) and Cu(111) surfaces [52] a single iron atom acts as a donor of spin momentum. It retains most of the spin momentum when it is in the so-called "ontop" position and loses it when the atom is in or inside the surface. The Bader charge transfer analysis for 3d TM atoms on graphene and graphene/Ni(111) surfaces [53] indicates that for all elements in the series electrons are transferred from the adatom to the graphene layer, leaving the net charge on the adatom positive. Magnetic atoms on the surface were also studied. Cobalt and iron atoms were placed onto the Pt(111) surface [54] and also on Pt(111) and Ir(111) surfaces.[55] There was shown that adatoms induce polarisation on nearby surface atoms. The magnetic anisotropy parameters also were calculated and they are in agreement with the experimentally determined ones, where inelastic tunnelling spectroscopy was implemented.[56]

The ability of an atom on a surface to have two stable states was studied in several articles. TM atoms on the graphene/Ni(111) surface can be ferromagnetic and antiferromagnetic toward the surface magnetisation.[53] It was found that for Ti, V and Cr antiferromagnetic alignment is preferable while for Mn, Fe and Co it is ferromagnetic (exchange energy for Fe, in this case, is 10 meV). By utilizing a combination of scanning tunnelling spectroscopy and DFT methods, it was shown that a Co atom on semiconducting black phosphorus [57] has two states: low-spin and high-spin. It was shown experimentally that the state of the atom can be switched electrically. A holmium atom on the MgO surface exhibits bistability property with up and down spin states.[58] It was shown that it is possible to read the states using a tunnel magnetoresistance and induce particular magnetic state of the iron atom (just to "write" it) with current pulses using a scanning tunnelling microscope.

1.2 Research Concept

TMPc molecules on 2D materials are extremely thin hybrid structures which possess magnetic moments. Understanding the nature of magnetism, as well as the ability to control magnetic properties, will help in creating super-thin magnetic devices. In this work, we contribute to the study of such structures using modern *ab initio* quantum chemistry methods.

In this thesis, we focus on two particular cases of hybrid systems consisting of the TMPc molecule grafted to the 2D material with the aim to understand the energetics

of these hybrid systems as well as magnetism of them paying particular attention to the influence of the substrate on magnetic states of the TM and the whole system.

It turns out that to get reliable predictions of the magnetism in these hybrid systems it is necessary to go beyond the standard DFT theory and develop a suitable multiconfigurational methodology, generally required for degenerated ground states of the systems.

The iron atom was chosen as a transition metal in TMPc because it was found that FePc possesses the biggest exchange energy among all TMPc molecules.[59] Other transition metals are also of interest and could be treated using the proposed techniques.

The research has two logical parts:

- first one is dedicated to the FePc/Graphene hybrid system and the influence of graphene defects on geometrical, energetic and magnetic properties of the system
- the second part is about magnetic interaction between the FePc molecule and the Ti_2C layer in the FePc/Ti_2C complex.

These two chosen systems can be treated as case studies to explore relevant physico-chemistry of the important class of hybrid systems consisting of magnetic molecules and 2D materials functioning as substrates.

In the next two paragraphs, we are going to summarise, first, the state-of-the-art of the research of these two systems, and, second, the theory and computational methodology required to study such systems.

1.2.1 FePc/Graphene

Most of the studies of systems consisting of a two-dimensional surface and a metal-organic molecule were carried out using the Kohn-Sham realisation of the density functional theory (DFT), and employing plane-waves as the basis set. This method reproduces well the geometry of a two-dimensional surface due to the fact that periodic conditions are used but does not allow one to study not completely filled shells of the d, f - orbitals of metal atoms, which are of direct interest for such structures.

Nowadays, the computational capabilities allow us to carry out studies of 2D-surface - metal-organic molecule complexes using multireference methods. For example, the iron porphyrin molecule and a graphene ribbon were treated separately with very high-level accuracy.[60] Porphyrin without a central metal on the graphene oxide was studied using multireference methods with 8 orbitals as active ones.[61] To employ multireference methods, the problem has to be reformulated in terms of finite, non-periodic systems, commonly used in quantum molecular chemistry. This problem can be easily solved in the case of graphene. A limited piece of the graphene layer, hereafter referred to as a cluster, can be limited by functionalising the extreme carbon atoms with hydrogen. With a sufficiently large graphene layer in the area, it is possible to create a structure very similar in physical and chemical properties to pure graphene.

In addition to the interaction of the FePc molecule on the pure sheet of graphene, the interaction of FePc with defects in graphene is also of interest. One of the main defect selection factors was the compliance of geometric parameters between the system with boundary conditions and the cluster. For example, it was found that graphene clusters, in the centre of which one (single valence) or two (double valence)

atoms are missing, do not repeat the flat structure of analogous periodic systems; stable states obtained after optimisation have strong curvatures. Therefore, further comparison of periodic and cluster systems with these defects is not possible.

Stone-Wales defects and various types of dopings are of particular interest for studying. The interaction of the Stone-Wales graphene defect with the FePc molecule has not been studied thoroughly enough, limiting itself to describing similar structures.[40, 41] Doping of atoms in the case of a graphene cluster requires special consideration, because, in contrast to a doped periodic structure, in which there may be no magnetic moment, the cluster must have an initial multiplicity in the case of adding an atom with an odd number of electrons. When a molecule with an intrinsic spin moment is added to a doped cluster, several options for choosing the spin moment arise. To study this situation, boron, nitrogen, and sulfur atoms were considered. Systems with the same doped atoms were studied previously [38] using density functional theory and these results could be compared with results obtained from cluster representation and multireference analysis.

The combined effects formed by replacing one of the atoms in the Stone-Wales defect were also studied. A theoretical study of such a multilevel defect using density functional theory predicts a slight broadening of the band gap, as well as an improvement in the accumulation of surface charge.[62] Also boron, nitrogen and sulfur were considered as dopants.

1.2.2 FePc/Ti_2C Study

As described earlier, the Ti_2C layer can be either ferromagnetic or antiferromagnetic, albeit the second option is slightly energetically favourable. By placing the FePc molecule, the magnetic moment of which is oriented in the same axis as the magnetic moments of the titanium layers, on the Ti_2C surface, we obtain a system that has several different magnetic configurations. Such systems have not been studied yet both theoretically and experimentally. And while experimental is complicated by the fact that the MXene layer comes into interaction with the atmosphere, theoretical predictions can describe such a system. A study of the single iron atom without the Pc ligand on Ti_2C was also carried out to understand the spin interaction of the iron atom with the MXene layer in more detail. Such a system does not have distortions caused by ligand fields. The study of FePc, Fe, and H_2Pc on Ti_2C provides understanding of the role of the flat Pc ligand in FePc and the benefit of its usage in comparison with a pure Fe atom.

Having presented the general background, the concept of the research, and two chosen case studies of hybrid systems involving magnetic molecules or 2D materials, we finish this chapter by introducing the outline of the thesis.

1.3 Outline of the Dissertation

- **Chapter 2** is devoted to the description of ab initio theoretical methods which are applied in the research. The general concept of the Hartree-Fock (HF) method is shown. Then, there is an explanation of how to go beyond one Slater-determinant wave function to describe the excited states of a system and what modern methods are used for it. The main idea of the density functional theory (DFT) is shown, and general approximations to take into account self-interaction error and dispersion forces are presented.

- Computational details for each used quantum chemical approach are presented in **Chapter 3**.
- In **Chapter 4** the description of the computations performed begins. Here, the results for the free FePc molecule are shown. The molecule was treated using multiple *ab initio* approaches, and differences in geometry and energetic properties are discussed.
- In **Chapter 5** the FePc/Graphene hybrid system is studied using the DFT method. The graphene layer is represented as a periodic material and as a restricted cluster with functionalised hydrogen atoms on boundaries. The geometric and energetic properties obtained by these two approaches are compared. Besides the system with a pure graphene layer, complexes with graphene defects (such as the Stone-Wales defect, B-doping, N-doping, and S-doping and combined B(N, S)-doped Stone-Wales defects) are studied. In addition, the possibility of reducing a graphene cluster to a simple pyrene molecule is studied. This FePc/Pyrene model will be explored in the next chapter.
- **Chapter 6** contains the description of the multiconfigurational analysis of the FePc/Pyrene complex. The defects considered in the previous chapter are also studied in the case of this hybrid system. We emphasise the study of transitions within the iron *d* shell and its interaction with pyrene defects. Excited states of systems are investigated.
- The study of the FePc molecule on the Ti_2C MXene layer is presented in **Chapter 7**. Here, we mostly focus on the magnetic properties of the formed system. Different magnetic configurations are modelled and compared. A single Fe atom on the top of Ti_2C is considered. It allows one to understand the role of the phthalocyanine ligand in the complex.
- In **Chapter 8**, we summarise the research and discuss future prospects.

Chapter 2

Theoretical background

2.1 Schrödinger Equation

The basic equation for molecular and solid state quantum chemistry is time-independent non-relativistic Schrödinger equation:[63]

$$\hat{\mathbf{H}}\,|\Psi\rangle = E|\Psi\rangle, \tag{2.1}$$

where $\hat{H}$ is the Hamiltonian of a system, Ψ is the wave function, E is the total energy.

The simplified non-relativistic Hamiltonian in the atomic units ($m = 1, e = 1, \hbar = 1$) has the following form:

$$\begin{aligned}\hat{\mathbf{H}} &= \hat{\mathbf{T}}_{\mathbf{n}}(\mathbf{R}) + \hat{\mathbf{T}}_{\mathbf{e}}(\mathbf{r}) + \hat{\mathbf{V}}_{\mathbf{ee}}(\mathbf{r}) + \hat{\mathbf{V}}_{\mathbf{ne}}(\mathbf{R}) + \hat{\mathbf{V}}_{\mathbf{nn}}(\mathbf{R}) = \\ &= -\sum_a \frac{1}{2M_a}\nabla_a^2 - \sum_i \frac{1}{2}\nabla_i^2 - \sum_{i,a}\frac{Z_a}{r_{ia}} + \sum_{i>j}\frac{1}{r_{ij}} + \sum_{b>a}\frac{Z_a Z_b}{R_{ab}},\end{aligned} \tag{2.2}$$

where $\mathbf{R} = \{\mathbf{R}_1, \cdots, \mathbf{R}_M\}$ are positions of M nuclei and $\mathbf{r} = \{\mathbf{r}_1, \cdots, \mathbf{r}_N\}$ are positions of N electrons; $T_n(\mathbf{R}), T_e(\mathbf{r}), V_{ee}(\mathbf{r}), V_{ne}(\mathbf{R}), V_{nn}(\mathbf{R})$ are kinetic energy operators of nuclei and electrons, and potential energy operator of Coulomb electron-electron, electron-nuclear, and internuclear interaction, respectively; M_a are masses of nuclei; i relates to electrons; a,b relate to nuclei, Z_a, Z_b are atomic numbers, r_{ij}, R_{ab}, r_{ia} are distances between electrons, nuclei, and an electron i and a nucleus a, respectively.

Since the translational motion of a system as a whole is not considered, the part of it that describes the translational motion is excluded from the exact wave function. Also, it can be assumed that slowly moving nuclei form an electrostatic field in which electrons move at a much higher speed, having time to instantly adjust to any change in the coordinates of the nuclei. Formally it means that one can represent wave function as a product of nuclear and electron functions: $\Psi(\mathbf{r}, \mathbf{R}) = \Psi_e(\mathbf{r}, \mathbf{R})\Psi_n(\mathbf{R})$. This approximation, essential for quantum chemistry, is called the Born-Oppenheimer approximation.[64] Assuming this, the total energy of a system is the sum of the electron energy calculated for a fixed configuration of the nuclei and the vibrational-rotational energy of the nuclei $E = E_e + E_n$. The quantum mechanical problem of N electrons in the field of nuclei at positions $\mathbf{R}$ reduces to the following Schrödinger equation

$$(\hat{\mathbf{T}}_{\mathbf{e}}(\mathbf{r}) + \hat{\mathbf{V}}_{\mathbf{ne}}(\mathbf{R}) + \hat{\mathbf{V}}_{\mathbf{ee}}(\mathbf{r}))\Psi_e(\mathbf{r}, \mathbf{R}) = E_e\Psi_e(\mathbf{r}, \mathbf{R}), \tag{2.3}$$

which results from Eq. (2.2), but where only electronic components are left.

2.2 Basis Sets

The many-electron wavefunction $\Psi_e(r, R)$ is extremely complicated, the whole Universe is not able to provide resources to store Ψ_e for systems consisting of even only few dozens of electrons.

Therefore, in all practical computational schemes, Ψ_e is approximated through objects based on one-electron states, which in turn are assumed to be built out of the suitably chosen basis functions sets, typically either localised orbitals or plane-waves.

For example, molecular orbitals ϕ_i describing one-electron states could be represented as a linear combination of atomic orbitals χ_μ (LCAO)

$$\phi_i(\mathbf{r}) = \sum_\mu c_{i\mu}\chi_\mu(\mathbf{r}). \tag{2.4}$$

Most computational codes use Gaussian type orbitals

$$g(\alpha, n, l, m, r, \theta, \phi) = Nr^{n-1}exp(-\alpha r^2)Y_{l,m}(\theta, \phi), \tag{2.5}$$

where N is a normalization factor; n, l, m are principal, angular and magnetic quantum numbers; $Y_{l,m}(\theta, \phi)$ are spherical harmonics. Atomic orbitals could be represented as a set of such primitives $\chi_i = \sum_i c_i g_i$. The benefit of such orbitals is ease of multiplication and integration of them. They are usually used for spatially restricted systems such as molecules or clusters.

To describe materials in a periodic cell the wave function should also be periodic. It means that $|\psi(\mathbf{r} - \mathbf{R_j})|^2 = |\psi(\mathbf{r})|^2$, where $\mathbf{R_i}$ is a lattice vector. Bloch's theorem states that in periodic potential the wave function takes the next form

$$\phi_\mathbf{k}(\mathbf{r}) = exp(i\mathbf{kr})u_\mathbf{k}(\mathbf{r}). \tag{2.6}$$

The periodic part of the Bloch function $u_\mathbf{k}$ (2.6) could be expanded in the plane waves

$$u_{j,\mathbf{k}}(\mathbf{r}) = \sum_{|\mathbf{G}|\leq G_{max}} e^{i\mathbf{Gr}}C_{\mathbf{G};j,\mathbf{k}}, \tag{2.7}$$

where $\mathbf{G} = n_1\mathbf{b_1} + n_2\mathbf{b_2} + n_3\mathbf{b_3}$ are reciprocal lattice vectors ($\mathbf{b_1}, \mathbf{b_2}, \mathbf{b_3}$ are primitive reciprocal lattice vectors), G_{max} is a maximum length of wave vectors $\mathbf{G}$, that are included into the expansion (2.7).

In practical calculations G_{max} is restricted by the energy cutoff parameter $E_{cutoff} = \frac{G_{max}^2}{2}$.

2.3 Hartree-Fock

To construct the wave function for solving the Schrödinger equation, one-election atomic orbitals (AO) wave functions $\phi_i(\mathbf{x_i}) = \phi_i(\mathbf{r})\eta(s_i)$ can be used. Here, $\phi_i(\mathbf{r})$ is the spatial part, and $\eta(s_i)$ is the spin part. In the simplest case, the N-electron wave function of the system is approximated by a single Slater determinant,[65] which is composed of atomic spin-orbitals occupied by electrons:

$$\Psi = \frac{1}{\sqrt{N!}} \begin{vmatrix} \phi_1(\mathbf{x_1}) & \phi_2(\mathbf{x_1}) & \dots & \phi_N(\mathbf{x_1}) \\ \phi_1(\mathbf{x_2}) & \phi_2(\mathbf{x_2}) & \dots & \phi_N(\mathbf{x_2}) \\ \vdots & \vdots & & \vdots \\ \phi_1(\mathbf{x_N}) & \phi_2(\mathbf{x_N}) & \dots & \phi_N(\mathbf{x_N}) \end{vmatrix} \tag{2.8}$$

$$= \frac{1}{\sqrt{N!}} \sum_{n=1}^{N!} (-1)^{p_n} P_n \{\phi_1(1)\phi_2(2)\dots\phi_N(N)\} \tag{2.9}$$

This approximation leads to the Hartree-Fock method.[66, 67] The Hartree-Fock equations for optimal atomic orbitals ϕ_i consisting the Slater determinant read

$$\hat{\mathbf{F}}_\mathbf{i}\phi_i(\mathbf{x_i}) = \epsilon_i\phi_i(\mathbf{x_i}) \quad (i = 1, ..., N), \tag{2.10}$$

where $\hat{\mathbf{F}}_\mathbf{i}$ is the Fock operator:

$$F_i = -\frac{1}{2}\nabla_i^2 - \sum_a \frac{Z_a}{r_{ai}} + \sum_{j=1}^{N} \int |\phi_j(x_j)|^2 \frac{1}{r_{ij}} d\mathbf{x_j} - \int \phi_j^*(\mathbf{x_j}) \frac{1}{r_{ij}} \phi_i(\mathbf{x_j}) d\mathbf{x_j}. \tag{2.11}$$

Each spin-orbital $\phi_i(x_i)$ has its Fock operator eigenvalue ϵ_i. The total energy of the system is:

$$E_{tot} = 2\sum_i^{N/2} \epsilon_i - \sum_{i\neq j}^{N/2} \sum_j^{N/2} (2J_{ij} - K_{ij}) + \sum_{a\neq b} \frac{Z_a Z_b}{R_{ab}}, \tag{2.12}$$

where one-electron AO orbitals energies ϵ_i are:

$$\epsilon_i = h_{ii} + \sum_{i\neq j}^{N} (2J_{ij} - K_{ij}), \tag{2.13}$$

and one-electron integral h_{ii} is the average value of one-electron operator $\hat{h}_i$:

$$\hat{h}_i = -\frac{1}{2}\nabla_i^2 - \sum_a \frac{Z_a}{r_{ai}}, \tag{2.14}$$

$$h_{ii} = \int \phi_j^*(\mathbf{x_j}) h_i \phi_i(\mathbf{x_j}) d\mathbf{x_j}. \tag{2.15}$$

Two-electron integrals J_{ij} (the Coulomb integral which describes the electron-electron repulsion energy) and K_{ij} (the exchange integral, which defines the decrease in the interaction energy of electrons with parallel spins in accordance with the Pauli principle) read:

$$J_{ij} = \int \phi_i^*(\mathbf{x_i}) \phi_i^*(\mathbf{x_i}) \frac{1}{r_{ij}} \phi_j(\mathbf{x_j}) \phi_j(\mathbf{x_j}) d\mathbf{x_i} d\mathbf{x_j} \tag{2.16}$$

$$K_{ij} = \int \phi_i^*(\mathbf{x_i}) \phi_j^*(\mathbf{x_i}) \frac{1}{r_{ij}} \phi_i(\mathbf{x_j}) \phi_j(\mathbf{x_j}) d\mathbf{x_i} d\mathbf{x_j} \tag{2.17}$$

The HF method has different versions, depending on whether the one-determinant wave function is an eigenfunction of the total spin square operator $\hat{S}^2$ or not. If it is, the wave function is constructed from spacial orbitals occupied by a pair of electrons with opposite spins, the method is called the restricted Hartree-Fock method (RHF). If there is no such requirement, then each spin-orbital corresponds

to a certain spin state, electrons with opposite spins occupy different spin orbitals. This method is applied to systems with unpaired high-orbital electrons and is called the unrestricted Hartree-Fock method (UHF).

2.4 Multireference Methods

2.4.1 Configuration Interaction

A disadvantage of the HF method is the treatment of the system of interacting electrons as independent particles and describing them by a one-determinant wave function; under these conditions, the interelectronic interaction is taken into account as the sum of the interaction of each electron with the average electron density of the remaining electrons. In fact, electron motion is correlated, there is an instantaneous Coulomb repulsion between particles that is missed in the HF approximation. There are dynamic correlation, correlation of electron motions, and static correlation, connected with the impossibility to describe the degenerated ground state with the help of one Slater determinant.

The expansion of the N-electron wave function in terms of a set of one-one-determinant wave functions describing various electronic configurations is a simple approach to account for electron correlation. Each electron configuration corresponds to a well-defined set of orbitals, and in the process of self-consistent solution of equations, the interelectronic interaction averaged over configurations covers various variants of the distribution of electrons at different distances between them.

In the configuration interaction (CI) method[68], the multielectron wave function is decomposed into a series of Slater determinants, each of which describes the system in a certain electronic state. Excited states are described by electronic configurations that take into account possible transitions of electrons from occupied molecular orbitals to various unoccupied orbitals. This means that each determinant is built from spin orbitals corresponding to the ground or one of the excited one-electron states of the molecule. The occupied and virtual molecular orbitals are orthonormal, the substituted determinants are orthogonal to the ground state determinant. For systems with open shells, the many-electron wave function is expanded into a series in linear combinations of Slater determinants, which are eigenfunctions of the operators S_z and S^2.

The total CI wave function Ψ_{CI} includes all possible electronic configurations

$$\Psi_{CI} = \sum_{k=0}^{\infty} a_k \Psi_k. \tag{2.18}$$

For practical implementation of the CI methods, the number of configurations in (2.18) should be restricted. The term "full CI" means taking into account all configurations of electrons on the molecular orbitals of the system. This approach could be implemented for small atomic systems but it is too costly for medium and large systems.

2.4.2 Complete Active Space Self-Consistent Field

The multiconfigurational self-consistent field method (MCSCF) is a variational approach in which both the HF molecular orbitals in the determinants and the coefficients a_k (2.18) are self-consistently optimised. The number of electronic configurations can be reduced to those that make the most significant relative contribution to the total energy. In the complete active space self-consistent field method (CASSCF) [69, 70, 71] among all molecular "active" orbitals, the highest occupied and the lowest unoccupied, are selected (fig. 2.1). Active orbitals are calculated using the CI method. Core orbitals, which are doubly occupied and have lower energy, and virtual orbitals, which are valence and have higher energy, are not used in the CI calculations and only active orbitals change is taken into account in Slater determinants Ψ_k (Eq. 2.18).

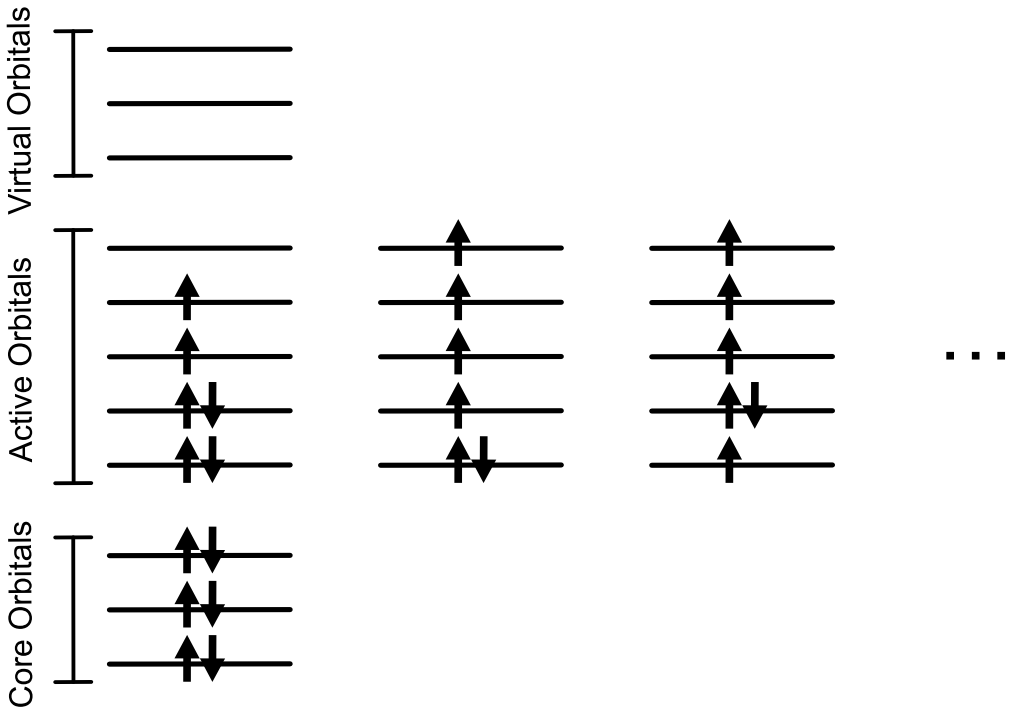

FIGURE 2.1: A scheme of the CASSCF approach. Inactive core and virtual orbitals are doubly occupied and not occupied, respectively. For active space, a set of Slater determinants with different electron configurations is used in CI calculations.

2.4.3 n-electron Valence State Perturbation Theory

As well as for the HF method, perturbation theory can be applied in the context of the CASSCF method.

The zero-order wave function $|\Psi_m^{(0)}\rangle$ in the multi-reference configurational theory is

$$|\Psi_m^{(0)}\rangle = \sum_{I \in \mathrm{CAS}} C_{I,m} |I\rangle , \tag{2.19}$$

where the summation runs over molecular orbitals I from the active space. It is rather obvious that the following relation holds:

$$\hat{\mathbf{P}}_{\mathrm{CAS}}\hat{\mathbf{H}}\hat{\mathbf{P}}_{\mathrm{CAS}}\left|\Psi_m^{(0)}\right\rangle = E_m^{(0)}\left|\Psi_m^{(0)}\right\rangle, \tag{2.20}$$

where $\hat{\mathbf{P}}$ is the projector onto the CAS-CI space.

It is possible to represent the $|\Psi_m^{(0)}\rangle$ wavefunction as a multiplication of core Φ_c (with n_c inactive electrons) and valence Ψ_m^v parts (with n_v active electrons),

$$\left|\Psi_m^{(0)}\right\rangle = |\Phi_c\Psi_m^v\rangle\,. \tag{2.21}$$

The perturbed wavefunction with k electrons moved from inactive orbitals to active ones is

$$\left|\Psi_{l,\mu}^k\right\rangle = \left|\Phi_l^{-k}\Psi_\mu^{v+k}\right\rangle, \tag{2.22}$$

where k is the order of perturbation. This method is called n-electron valence state perturbation theory (NEVPT) or NEVPT2 (where the last number 2 means the order of perturbation, $-2 \leq k \leq 2$).[72]

For NEVPT2, there are several possibilities of excitations:

- two electrons from core orbitals to virtual orbitals (the active space remains the same, $k = 0$),
- one electron from a core orbital to a virtual orbital, and one electron from a core orbital to an active orbital (the active space has one less electron, $k = +1$),
- one electron from a core orbital to a virtual orbital, and one electron from an active orbital to a virtual orbital (the active space has one more electron, $k = -1$),
- two electrons from core orbitals to active orbitals (the active space has two more electrons, $k = +2$),
- two electrons from active orbitals to virtual orbitals (the active space has two fewer electrons, $k = -2$),
- one electron from a core orbital to a virtual orbital, and an internal active-active excitation ($k = 0$),
- one electron from a core orbital to an active orbital, and an internal active-active excitation ($k = +1$),
- one electron from an active orbital to a virtual orbital, and an internal active-active excitation ($k = -1$).

2.5 Density Functional Theory

2.5.1 Hohenberg-Kohn Theorem

One-electron density, the probability of the presence of an electron in an infinitely small area around a point $\mathbf{r}$ in space, can be calculated as

$$\rho(\mathbf{r}) = N\sum_\sigma \int \mathrm{d}\mathbf{x}_2 \cdots \int \mathrm{d}\mathbf{x}_N\, |\Psi(\mathbf{r},\sigma,\mathbf{x}_2,...,\mathbf{x}_N)|^2, \tag{2.23}$$

where N is the number of electrons, and $\mathbf{x} \equiv (\mathbf{r}, \sigma)$ defines both spacial $\mathbf{r}$ and spin σ coordinates.

Using this quantity as the basis for determination of the total energy of multi-electron systems instead of the multielectron wave functions Ψ would reduce the number of dependent variables from 3N to N, and would be extremely attractive from computational point of view.

Excluding purely nuclear components from the full Hamiltonian (2.2), in accordance with the Born-Oppenheimer approximation, the Hamiltonian of the system of N electrons in the external potential of the all nuclei

$$\begin{aligned} \hat{\mathbf{H}} &= \hat{\mathbf{T}}_\mathbf{e} + \hat{\mathbf{V}}_\mathbf{ne} + \hat{\mathbf{V}}_\mathbf{ee} = \\ &= -\sum_i \frac{1}{2}\nabla_i^2 + \sum_i v_{ext}(\mathbf{r_i}) + \sum_{i>j} \frac{1}{r_{ij}}. \end{aligned} \tag{2.24}$$

where $v_{ext} = -\sum_a \frac{Z_a}{|\mathbf{r}-\mathbf{R}_a|}$. The Hohenberg-Kohn theorem [73] states that there exists an electron density ρ and a functional $F[\rho]$, such that

$$E_0 = min_\rho \{ \int d^3\mathbf{r} v_{ext}(\mathbf{r})\rho(\mathbf{r}) + F[\rho] \} = \int d^3 r v(\mathbf{r})\rho_0(\mathbf{r}) + F[\rho_0], \tag{2.25}$$

where E_0 and ρ_0 are the ground-state energy and ground-state density of the system characterised by the external potential $v_{ext}(\mathbf{r})$. This method of finding the total ground state energy of the system of N interacting electrons in terms of the one-electron charge density and functional formulation is called density functional theory (DFT).[74]

The DFT formulation provided by Hohenberg and Kohn, and later on in the so-called "constrained search" formulation proposed by Mel Levy [74] states only the existence of universal functional of the one-electron density $F[\rho]$, but unfortunately does not give it explicit form.

Instead, one can define solely the contributions to $F[\rho]$ corresponding to kinetic energy of the interactions electrons $T[\rho]$ and electron-electron interaction $U[\rho]$, so $F[\rho] = T[\rho] + U[\rho]$. The attempts to approximate $T[\rho]$ and $U[\rho]$ on the basis of known expressions for homogeneous electron gas have not provided reliable quantitative results for inhomogeneous systems such as atoms, molecules, and solids.

However, very soon after the appearance of the Hohenberg and Kohn paper, Kohn and Sham published the practical realisation of the DFT that has been the basis of all practical DFT computational tools developed since then.

2.5.2 Kohn-Sham Theory

W. Kohn and L.J. Sham showed [75] that the system of N-interacting electrons, characterised by the one-electron density $\rho(\mathbf{r})$ can be mapped on virtual system of non-interacting electrons with one-electron density $\rho_s(\mathbf{r})$ equal to $\rho(\mathbf{r})$, $\rho_s(\mathbf{r}) = \rho_(\mathbf{r})$.

It is well known that the many electron wave function of non-interacting Fermions is a Slater determinant $\Phi(\mathbf{x_1}, ..., \mathbf{x_N})$ defined through N one-electron spin-orbitals $\phi_i(\mathbf{x})$. Then the one-electron density

$$\rho(\mathbf{r}) = \rho_s(\mathbf{r}) = \sum_i^N |\phi_i(\mathbf{r})|^2. \tag{2.26}$$

The second advantage of employing the virtual system of non-interacting electrons is easiness to define and compute the kinetic energy functional for such case $T_s[\rho]$.

The well known is also classical Coulomb repulsion energy of the charge distribution described by $\rho(\mathbf{r})$

$$U_H[\rho] = \frac{1}{2}\int\int \frac{\rho(\mathbf{r})\rho(\mathbf{r}')}{|\mathbf{r}-\mathbf{r}'|}d\mathbf{r}d\mathbf{r}', \tag{2.27}$$

and also the exchange energy $E_X[\rho]$ for the system described by the Slater determinant Φ.

The only unknown component of the electron-electron interaction energy functional $U[\rho]$ remains, therefore, the correlation energy $E_C[\rho]$,

$$U[\rho] = U_H[\rho] + E_X[\rho] + E_C[\rho]. \tag{2.28}$$

One can write then the functional $F[\rho]$ in the following form

$$F[\rho] = T_s[\rho] + U_H[\rho] + E_X[\rho] + E_C[\rho] + T[\rho] - T_S[\rho]. \tag{2.29}$$

Customarily the last four terms of the functional $F[\rho]$ (2.29) are named exchange-correlaion functional

$$E_{XC}[\rho] := E_X[\rho] + E_C[\rho] + T[\rho] - T_S[\rho], \tag{2.30}$$

and this functional is approximated in various practical applications of the Kohn-Sham realisation of DFT. Nowadays, in computations there are used around 200 approximated versions of $E_{XC}[\rho]$.

The only question one needs to answer is how to determine the one-particle Kohn-Sham orbitals ϕ_i instead of minimising $E[\rho]$ with respect to ρ as in the original DFT.

The minimisation of the functional (2.29) with respect to one-electron wave functions leads to the Kohn-Sham (KS) equations for one-electron orbitals ϕ_i:

$$\hat{\mathbf{h}}_i^{KS}\phi_i(\mathbf{r}) = \epsilon_i\phi_i(\mathbf{r}) \quad (i = 1, ..., N), \tag{2.31}$$

where the one-electron Kohn-Sham operator $\hat{\mathbf{h}}$ is defined as:

$$\hat{\mathbf{h}}_i^{KS} = -\frac{1}{2}\nabla_i^2 + v_{ext}(\mathbf{r}_i) + \int \frac{\rho(\mathbf{r}')}{|\mathbf{r_i}-\mathbf{r}'|}d\mathbf{r}' + v_{XC}(\mathbf{r}_i), \tag{2.32}$$

with the exchange-correlation potential $v_{XC} = \delta E_{XC}[\rho]/\delta\rho$. The KS equations (2.31), together with the equation defining ρ in terms of ϕ_i (2.26), have to be solved in a self-consistent manner.

By the analogy with the Hartree-Fock approach, the restricted Kohn-Sham (RKS) and unrestricted Kohn-Sham (UKS) methods also exist, just to treat spin unpolarised and spin polarised systems, respectively.

2.5.3 Approximations

The crucial issue in the KS realisation procedure is the choice of the approximation for exchange-correlation energy functional $E_{XC}[\rho]$.

The simplest approximation for $E_{XC}[\rho]$ is based on a model of a homogeneous non-degenerate gas of non-interacting electrons located in the external field of nuclei. It is called the local density approximation (LDA). It is assumed that the density of non-homogeneous system at point $\mathbf{r}$, $\rho(\mathbf{r})$, is equal "locally" to the density of homogeneous electron gas is the same at any point in the system. For each point $\mathbf{r}$, the value of the electron density of the real system at this point is substituted into the formulas valid for a homogeneous electron gas. This can be done if the electron density of non-homogeneous system is a slowly varying function of the coordinates.

The LDA approximation for the exchange-correlation functional is

$$E_{XC}^{LDA}[\rho] = \int \epsilon(\rho(\mathbf{r}))\rho(\mathbf{r})d\mathbf{r}, \tag{2.33}$$

where $\epsilon(\rho(\mathbf{r})) = \epsilon_x(\rho(\mathbf{r})) + \epsilon_c(\rho(\mathbf{r}))$ is the exchange-correlation energy per particle, known for homogeneous electron gas.

The LDA approximation played important role in the development of reliable computational tools for quantum mechanical description of atomic, molecular, and solid state systems. However, the LDA approximation could be unsatisfactory for systems in which the electron density distribution is very inhomogeneous. To take into account the inhomogeneity, the generalized gradient approximation (GGA) is used where the dependence of the exchange-correlation energy on the density gradient is also taken into account. The general expression for the exchange-correlation energy in this approximation is

$$E_{XC}^{GGA}[\rho] = \int f_{XC}(\rho(\mathbf{r}), \nabla\rho)\rho(\mathbf{r})d\mathbf{r}, \tag{2.34}$$

A unified expression for the integrand f_{XC} does not exist but there are various approximate forms. These forms were found in a standard way: an *ab initio* calculation of noble atoms in the orbital approximation was carried out with the fullest accounting for exchange and correlation (for example, by methods of coupled clusters or configuration interaction in a wide basis), then the terms associated with the exchange and correlation energies, and approximate expressions for $\epsilon_x(\rho(\mathbf{r}))$ and $\epsilon_c(\rho(\mathbf{r}))$ were fitted to them.

2.5.4 Hubbard Correction

The standard DFT method described above has a disadvantage in that one electron interacts with its own contribution to the mean-field (self-interaction error). And, as in the HF method, when electrons are strongly localised their motion is correlated. In principle, the multiple Slater determinant wave function (2.18) solves this problem however for a big periodic system that method is bulky and difficult to apply. To correct the result it is possible to use the Hubbard +U correction where the standard DFT energy functional $F[\rho(\mathbf{r})]$ (2.29) changes by adding the correction

$$F_{DFT+U}[\rho(\mathbf{r})] = F[\rho(\mathbf{r})] + F_{Hub}[\{n_{mm'}^{I\sigma}\}] - F_{DC}[\{n^{I\sigma}\}]. \tag{2.35}$$

Occupation numbers $n_{mm'}^{I\sigma}$ (projections of occupied Kohn-Sham orbitals (ψ_{kv}^{σ}) on the states of a localized basis set (ϕ_m^I)) are defined as

$$n_{mm'}^{I\sigma} = \sum_{k,v} f_{kv}^{\sigma} \langle \psi_{kv}^{\sigma} | \phi_{m'}^{I} \rangle \langle \phi_m^I | \psi_{kv}^{\sigma} \rangle, \tag{2.36}$$

where f^{σ}_{kv} are the Fermi-Dirac occupations of the KS states (k is the k-point index, v is the band index), I means the site, n the main quantum number, m the magnetic number, and σ the spin index.

In the approach by Liechtenstein *et al.*[76] the local screen Coulomb correlation term F_{Hub} is taken as:

$$\begin{aligned} F_{Hub}[\{\mathbf{n}^{\sigma}\}] = \frac{1}{2}\sum_{\{m\},\sigma}\{&\langle m, m^{''}|V_{ee}|m^{'}, m^{'''}\rangle n^{\sigma}_{mm'} n^{-\sigma}_{m''m'''} + \\ &+ (\langle m, m^{''}|V_{ee}|m^{'}, m^{'''}\rangle - \\ &- \langle m, m^{''}|V_{ee}|m^{'''}, m^{'}\rangle) n^{\sigma}_{mm'} n^{\sigma}_{m''m'''}\}, \end{aligned} \tag{2.37}$$

and the DFT-double counting term F_{DC} is

$$F_{DC}[\{\mathbf{n}^{\sigma}\}] = \frac{1}{2}Un(n-1) - \frac{1}{2}J[n^{\uparrow}(n^{\uparrow}-1) + n^{\downarrow}(n^{\downarrow}-1)], \tag{2.38}$$

where $n^{\sigma} = Tr(n^{\sigma}_{mm'})$ and $n = n^{\uparrow} + n^{\downarrow}$. U and J are screened Coulomb and exchange parameters.

Cococcioni *et al.*[77] proposed a simplified correction assuming $J = 0$,

$$\begin{aligned} &F_{Hub}[\{n^{I}_{m,m'}\}] - F_{DC}[\{\mathbf{n}^{I}\}] = \\ &= \frac{U}{2}\sum_{I}\sum_{m,\sigma}\{n^{I\sigma}_{mm} - \sum_{m'} n^{I\sigma}_{mm'} n^{I\sigma}_{m'm}\} \\ &= \frac{U}{2}\sum_{I,\sigma} Tr[\mathbf{n}^{I\sigma}(1 - \mathbf{n}^{I\sigma})], \end{aligned} \tag{2.39}$$

where the U parameter can be calculated using the linear response method.

2.5.5 Pseudopotentials

The occupied electron shells in atoms can be divided into two categories: core, the lowest orbitals, which do not participate in the interaction within the system, and valence, which have the highest energy and actively participate in the formation of bonds and affect the physical and chemical characteristics of the system. All electron methods take into account both core and valence orbitals on an equal footing. But if electron transitions from deep energy levels are not so important for investigated properties of the systems studied, it is possible to describe core electrons using a nonlocal pseudopotential function. In this case, only valence electrons are taken explicitly into account. This approximation is widely used for all atoms in periodic systems and for heavy atoms (usually if $Z \geq 37$) in non-periodic LCAO calculations.

The special class of pseusopotentials constitute the so-called norm-conserving pseudopotentials,[78] where the norm of the atomic orbital is conserved, and $\psi^{\star}_{ps} = \psi^{\star}_{AE}$ for $|\mathbf{r}| > r_c$:

$$\int_0^{r_c} \psi^{\star}_{AE}(\mathbf{r})\psi_{AE}(\mathbf{r})d\mathbf{r} = \int_0^{r_c} \psi^{\star}_{ps}(\mathbf{r})\psi_{ps}(\mathbf{r})d\mathbf{r} \tag{2.40}$$

In this case, all electron $\psi^{\star}_{AE}$ and pseudo $\psi^{\star}_{ps}$ wavefunctions are fitted out of a chosen cutoff radius r_c (each shell has its own radius). Often such pseudopotentials lead to accurate results with medium size plane-wave basis set ($E_{cutoff} = 10 - 20Ry$). However, for atoms with oscillating wave function (first-row elements, elements

with $3d$ and $4f$ valence electrons) norm-concerning pseudopotential construction gives corresponding pseudo-functions that are nearly equal to all-electron states. The condition of conservation of the norm means that in some cases it is impossible to construct a pseudo-wave function that is much smoother than the all-electron wave function. Thus, employment of the norm-conserving pseudopotentials could require large plane-wave basis sets ($E_{cutoff} > 70Ry$).

Ultrasoft pseudopotentials (USPP), introduced by Vanderbilt,[79] were designed to solve this problem. There, the pseudo-wave function norm (2.40) differs from the all-electron one. The benefit of ultrasoft pseudopotentials is that they need fewer plane waves which improve the accuracy of calculations with the same available processing power.

Projected augmented waves (PAW) pseudopotentials[80] can be considered as all-electron pseudopotentials with frozen states of the core electrons such as those in free atoms. There is a linear transformation that relates the all-electron orbitals of the wave function to the pseudo-orbitals and it is possible to recover all-electron orbitals from pseudo-orbitals.

2.5.6 van der Waals Correction

The standard DFT method described above does not take into account dispersive van der Waals forces which are weaker than covalent forces but play important role in intramolecular interactions and molecular adsorption to a surface. The dispersion part of the van der Waals forces, forces of electrostatic attraction of instantaneous and induced dipoles of electrically neutral atoms or molecules, contributes a lot to a molecular-surface interaction and ignoring it yields very often to a wrong adsorption structure.

There are several approaches to include van der Waals interactions in DFT calculations. In principle, all of them add a correction $E_{XC}^{non-local}$ to the exchange-correlation functional E_{XC}. Performances of all methods are tested using comparison with high-quality post-HF methods such as the coupled-cluster.[81] Non-local functionals, like vdW-DF-04 and vdW-DF-10 by Langreth and Lundqvist,[82, 83] represent the exchange-correlation potential as

$$v_{XC}^{n-l}(\mathbf{r}) = \int f(\mathbf{r}, \mathbf{r}')d\mathbf{r}'. \tag{2.41}$$

Such functionals can describe the interaction of one atom at the point $\mathbf{r}$ with an atom at the point $\mathbf{r}'$ which could be far removed. This approach leads to a double integration in exchange-correlation energy calculation

$$E_{XC}^{n-l} = \int v_{XC}^{n-l}(\mathbf{r})d\mathbf{r} = \int\int f(\mathbf{r}, \mathbf{r}')d\mathbf{r}d\mathbf{r}'. \tag{2.42}$$

Although methods of integration of such potentials are well developed, they still make the use of non-local functionals for large systems quite expensive.

Meta-GGA functionals (like M06 [84]) are advanced GGA-type functionals (2.34) where not only the density and its first derivative but also its second derivative are included. Meta-GGA functionals can describe short-range interactions whenever a density overlap still exists. But these functionals do not include the correct description of van der Waals interaction and they show unsatisfactory results if long-range interactions play an important role.

Probably the computationally cheapest methods are interatomic van der Waals correction methods.[85, 86, 87] Usually, in these methods, a dispersion correction to

the exchange-correlation functional is given in a form of two-body energy

$$E_{AB}^{disp}(R) = -(f_6(R)\frac{C_6^{AB}}{R_{AB}^6} + f_8(R)\frac{C_8^{AB}}{R_{AB}^8} + f_{10}(R)\frac{C_{10}^{AB}}{R_{AB}^{10}} + \cdots), \tag{2.43}$$

where $f_6, f_8, f_{10}, \cdots$ are previously chosen damping functions; interaction coefficients $C_6^{AB}, C_8^{AB}, C_{10}^{AB}, \cdots$ and vdW radii R_{AB} are parameters which are unique for each atomic pair and were found based on fitting to higher quality quantum chemical computations. The popular Grimme DFT-D3 correction [85] includes into the dispersion correction also the three-body energy term

$$E_{ABC}^{disp}(R) = \frac{C_9^{ABC}(3cos\theta_a cos\theta_b cos\theta_c + 1)}{(r_{AB}r_{BC}r_{AC})^3}, \tag{2.44}$$

where θ_a, θ_b,and θ_c are the internal angles of the triangle formed by r_{AB}, r_{BC}, and r_{AC}, and C_9^{ABC} is the triple-dipole constant.

In comparison with non-local and meta-GGA functionals, interatomic van der Waals correction methods include highly parametrized forms of dispersion interaction. The interatomic dispersion parameters are provided which highly reduces the cost of employing these corrections. Such methods are mostly used for relatively big systems where the van der Waals interaction plays an important role and the size of a system requires simplification of computational methods.

Chapter 3

Computational Details

In the thesis, the FePc/Graphene and FePc/Ti_2C hybrid systems were studied employing the DFT computational scheme in the framework of DFT theory. Also, multiconfigurational methods were employed to investigate magnetic properties of the FePc/Graphene hybrid system. Here, we present the computational details of these calculations.

3.1 FePc/Graphene

3.1.1 Periodic System

The periodic DFT calculations were performed employing the Quantum Espresso 6.5 package[88] on the level of the generalized gradient approximation (GGA),[89] using the Perdew-Burke-Ernzerhof (PBE) exchange-correlation functional.[90] The Van der Waals interaction between a molecule and a layer was included using the Grimme DFT-D3 methodology.[85] To treat the strong on-site Coulomb interaction of TM d-electrons, we used DFT+U approach within the Hubbard model.[91] The U parameter value for the iron atom was taken from the results of linear response calculations for TMPc molecules.[92] The kinetic energy cutoff for wavefunctions was taken to be 45 Ry, and a corresponding parameter for charge density and potential was 450 Ry. Preliminary estimations, optimisation, and calculation of energy parameters were performed at the Γ point. Calculations of densities of states were performed using the $2 \times 2 \times 1$ Monkhorst–Pack k-point mesh. Optimisation was carried out until a force value of less than 0.001 Ry/a.u on every atom and in each cartesian direction was achieved, and simultaneously stress tensor components reached values smaller than 0.5 kbar.

3.1.2 Cluster System

The calculations of cluster systems were performed using the *ORCA* package,[93, 94] where the GGA-PBE functional and the D3 correction were used as in computations with periodic boundary conditions. The triple-ζ polarised def2-TZVP basis set [95] was implemented and a semi-empirical counterpoise-type correction [96] was used to decrease the basis set superposition error (BSSE).

The following equation was used to estimate the adsorption energy E_a:

$$E_a = E_{FePc+Gr} - E_{FePc} - E_{Gr}, \tag{3.1}$$

where $E_{FePc+Gr}$ denotes the total energy of the FePc/graphene hybrid system, whereas E_{FePc}, and E_{Gr} are energies of the free molecule, and the surface, respectively.

Cohesive energies for defected graphene clusters and pyrene were calculated using the formula

$$E_{coh} = \frac{E_{doped\ gr} - \sum_i^N E_i}{N} \tag{3.2}$$

where $E_{doped\ gr}$ is the total energy of the doped system, E_i is the total energy of the individual elements i (i = C, B, N, S, H), and N is the total number of atoms in the cluster. Cohesive energy shows the energy difference between the energy of atoms in the molecular state and in the gas state with all atoms separated from each other. This parameter allows for comparing the stability of defected structures. Similar calculations have also been done before.[97]

3.1.3 Multireference Calculations

The multireference calculations of cluster systems were performed using the *ORCA* package.[93, 94] Optimisation of systems geometry was performed using DFT methods. Multireference calculations were done using different basis sets for different types of atoms: polarised valence double-zeta basis set def2-SVP for hydrogen and carbon atoms, diffuse polarised triple-zeta basis set def2-TZVPD for nitrogen, boron and sulfur atoms and diffuse doubly polarised triple-zeta basis set def2-TZVPPD for the iron atom. This choice of basis sets is a compromise between the demand for random access memory (RAM) necessary to perform calculations and the accuracy that can be reached to satisfactorily describe the charge density in the region of the iron atom. Also, the RIJCOSX [98] algorithm that treats the Coulomb term via RI (repulsion integrals) and the exchange term via seminumerical integration was implemented. Corrected energetic states of the hybrid systems were found using strongly contracted NEVPT2 [99] perturbation theory.

3.2 FePc/Ti_2C

The DFT calculations for the studied hybrid FePc/Ti_2C system with periodic boundary conditions were performed employing the Quantum Espresso 6.5 numerical package [88] with the generalised gradient approximation (GGA) [89] realised through the Perdew-Burke-Ernzerhof (PBE) exchange-correlation functional.[90] The van der Waals interaction between the molecule and the Ti_2C layer was accounted for within the Grimme DFT-D3 ad-hoc scheme.[85] Rappe-Rabe-Kaxiras-Joannopoulos (RRKJ) ultrasoft pseudopotentials from pslibrary [100] were implemented. To treat the strong on-site Coulomb interaction of TM d-electrons, we used the DFT+U approach within the Hubbard model.[91] The U parameter value for the Fe atom (U = 4 eV) was taken from the previous results of linear response calculations for TMPc molecules.[92] To simulate the excited state with S = 2, the Hubbard parameter U was changed from 4 to 6 eV. The kinetic energy cutoff for wavefunctions was set to 45 Ry and the corresponding parameter for charge density and potential to 650 Ry. Preliminary estimations, optimisation, and calculation of energy parameters were performed at the Γ point. The chosen supercell for the FePc/Ti_2C hybrid system consisted of 7x7 Ti_2C primitive cells. Such size of the supercell makes it possible to place FePc molecules at a distance of 6.36 Å from each other, which practically excludes their spurious interaction. For the test case of a single Fe atom on the Ti_2C surface (Fe/Ti_2C), preliminary estimations, optimisation, and calculation of energy parameters were performed at the Γ point for 7x7 and 4x4 Ti_2C supercells. For the case with the primitive Ti_2C cell, a denser grid of 5x5 k-points was used.

The adsorption energy E_a was determined according to the formula

$$E_a = E_{Fe(Pc)+Ti_2C} - E_{Fe(Pc)} - E_{Ti_2C}, \tag{3.3}$$

where $Fe(Pc)$ indicates either a single iron atom (Fe) or iron phthalocyanine ($FePc$); Ti_2C - the substrate, and $Fe(Pc) + Ti_2C$ the whole system. To guarantee suitable accuracy of E_a, the energies of these three systems are calculated in the same supercell.

To investigate electron transfer, we performed an analysis of the laterally averaged electronic charge density $\rho_{charge} = \rho_\uparrow + \rho_\downarrow$ and spin density $\rho_{spin} = \rho_\uparrow - \rho_\downarrow$, where $\rho_\uparrow$ and $\rho_\downarrow$ are spin up and spin down electron charge densities, respectively. The methodology of charge transfer evaluation was inspired by the Bader charge analysis[101], where the borders between the charge densities of two atoms are determined along the local minimum of the charge densities. Here, we consider the charge transfer between the Ti_2C surface and the flat FePc molecule or the iron atom. For this purpose, the charge density ρ is integrated over xy-planes in each point along the z-axis, which gives laterally averaged charge density $\bar{\rho}(z)$

$$\bar{\rho}(z) = \frac{1}{S} \iint_S \rho(x, y, z)\, dx\, dy, \tag{3.4}$$

where S is the area of the unit cell. A similar approach has been previously implemented to study charge distribution in the hybrid system of VPc on gold surface.[102] The minimum of the laterally averaged charge density $\bar{\rho}(z)$ between the surface and the molecule could be then considered as a surface (or line) dividing the regions of the substrate and the molecule. The accurate minimum was found using the polynomial approximation in the vicinity of the boundary.

It is worth noting that the charge density analysis was performed only for valence electrons qualified as such in the employed pseudopotential. The chosen pseudopotentials have the following valence configurations: Ti($3s^2 4s^2 3p^6 3d^2$), C($2s^2 2p^2$), Fe($4s^1 3d^7$), N($2s^2 2p^3$), H($1s^1$).

Chapter 4

FePc: Geometry and Electronic Structure

Before we present results for studied hybrid structures, let us analyse the morphology, electronic structure, and magnetic properties of free standing iron phthalocyanine.

An isolated iron phthalocyanine molecule (Fig. 4.1) has a tetragonal D_{4h} symmetry. The central iron atom is in the square planar ligand field which is created by nitrogen atoms. The strong ligand field makes the iron $d_{x^2-y^2}$ orbital unfavourable, and, therefore, the ground state of the molecule is triplet. The exact ground state is a topic to study due to the energetic proximity of the two states. While it seems to be commonly accepted that the ground state of FePc is E_g with the iron $3d$-shell configuration $d^2_{xy}d^2_{xz}d^1_{yz}d^1_{z^2}d^0_{x^2-y^2}$ (Fig. 4.2c), there exist computations predicting A_{2g} state (with the $d^2_{xy}d^1_{xz}d^1_{yz}d^2_{z^2}d^0_{x^2-y^2}$ iron $3d$-shell configuration) as the ground state.[103]

The excited quintet and singlet states can be modelled using one-Slater-determinant DFT methods. Using LCAO basis sets for the free FePc molecule, it was found that quintet and singlet states are higher by 1.24 and 1.43 eV, respectively, in comparison to the ground state energy. The Fe-N distances in the molecule are similar for all states and are about 1.935 Å. Plane-wave methods with the molecule in the cubic cell with the 20 Å face show that the Fe-N bond lengths are 1.95 Å in the ground state, 2.01 Å in the quintet and 1.92 Å in the singlet. This elongation of the bonds was previously found for molecules with the Fe-N_4 centre.[23] The Fe-N bonds lengthening weakens the ligand field created by nitrogen atoms of tetragonal symmetry. Thus, the electrons of the d-shell of the iron atom occupy the higher energy orbitals. The quintet excited state is 0.44 eV higher than the triplet state and the singlet state is 2.68 eV higher. The precise multideterminant NeVPT2 method (Table 4.1) gives lower values of the transition energies than DFT. A more detailed discussion of the results will be made below in the part about multireference calculation analysis.

	Triplet-Quintet, eV	Triplet-Singlet, eV
DFT, LCAO	1.24	1.43
DFT, Plane Wave	0.44	2.68
NeVPT2(6,5)	0.41	1.28
NeVPT2(10,9)	0.4	0.85

TABLE 4.1: Energy differences between the FePc ground triplet state and excited quintet and singlet states calculated by different quantum chemistry methods.

The FePc symmetry is represented well in the cubic cell. Below, FePc will be studied on the hexagonal lattice structure surfaces. Therefore, the point symmetry of

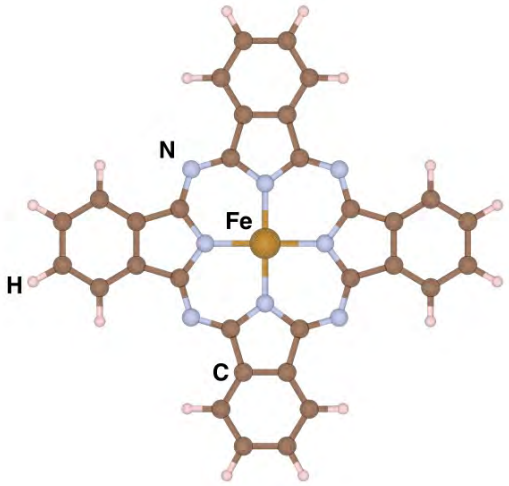

FIGURE 4.1: The FePc molecule.

the hybrid system consisting of FePc attached to a substrate is relatively low, the C_2 one. For that reason, optimisation of the geometries of the hybrid systems could lead to FePc geometry slightly distorted from the ideal one. The difference is seen in iron *d*-shell projected densities of states for FePc in cubic (Fig. 4.2B) and hexagonal (Fig. 4.2A) lattices. While in the cubic cell the FePc ground state is E_g, in the hexagonal cell it is A_{2g}. These results shed light on the previously mentioned discrepancies of theoretically predicted state of the FePc free standing molecule.

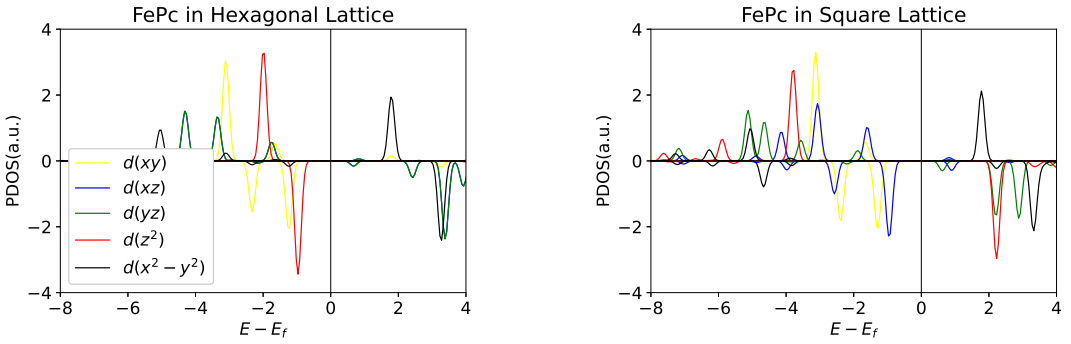

(A) (B)

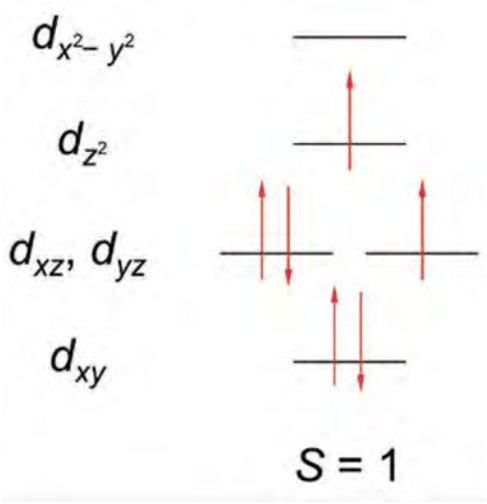

(C)

FIGURE 4.2: Spin-polarised PDOS of the 3d orbitals of the FePc iron atom in (a) hexagonal and (b) cubic cells; (c) iron 3*d* shell configuration in the E_g FePc ground state.

Chapter 5

FePc/Graphene: DFT studies

5.1 Graphene

5.1.1 Graphene Cell Choice for the Calculations with Periodic Boundary Conditions

The choice of the graphene surface size was dictated by a compromise between computational time and accuracy of calculations. In the case of the periodic systems, we wanted to get rid of the eventually possible spurious interaction between FePc molecules, both in lateral plane and the vertical direction, in order to study the interaction of strictly single molecule with the graphene layer. Such spurious interactions between the FePc molecule and its images in the neighbouring cell can be induced by periodic boundary conditions imposed on the system, if the dimensions of the employed supercell are not sufficiently large. The estimations of the effect mentioned above (Table 5.1) were performed using different graphene supersells, from the smallest possible supercell where FePc molecules can lie on the surface without overlapping each other up to considerably larger supercells. For purpose of such estimations, only the molecule was relaxed, while the graphene layer was frozen. That is why the estimations presented here slightly differ from the results presented in following chapters below. Gradually increasing the lattice size, it was found that when using a cell consisting of 9x9 unit cells of graphene, the intermolecular interaction is practically absent and does not affect the geometry and energy parameters of the complex. This supercell was chosen for further studies.

Supercell Size	Adsorption Energy, eV	Distance between FePc's, Å
6x6	-6.73	1.60
7x7	-4.72	2.27
8x8	-3.73	4.62
9x9	-3.01	7.07
10x10	-3.03	9.53
15x15	-3.33	21.68

TABLE 5.1: Adsorption energies and distances between FePc molecules (defined as the distance between the two closest hydrogen atoms of different molecules) for FePc/Gr systems as a function of supercell size.

5.1.2 Graphene Cluster Choice

In the case of the cluster calculations, the main test parameters were, like in the case of supercell calculations, geometry and physisorption energy. The structure with a cluster of 25 (5x5) rings (Fig. 5.1D) shows the similar physisorption energy (Table 5.2) and also completely covers the surface under the molecule. An enlargement of the graphene surface significantly increases the computational burden. The FePc/Gr 5x5 model is good for comparing the possibility of representing the FePc/Gr system as a cluster but too big to perform multireference NeVPT2 calculations. Even in the small def2-SVP basis set more than 2 TB of RAM is needed, and our avaliable at the University of Warsaw computer resources do not allow us to perform such calculations with sufficient accuracy. Therefore, we have also performed the DFT calculations with the smaller sizes of graphene flakes consisting of 16 (4x4), 9 (3x3), and 4 (2x2) carbon rings. These systems are depicted in Fig. 5.1C, 5.1B, and 5.1A, respectively. The smallest flake (the 2x2 graphene cluster) is just the pyrene molecule. The values of adsorption energy and geometrical parameters of hybrid systems are shown in Table 5.2. It is clearly seen that adsorption energy decreases with the cluster size, which means that the adhesion of the FePc molecule to the graphene flake gets stronger with flake's size. We ascribe this effect to the vdW interaction between carbon rings ("petals") in the molecule and the flakes. FePc-graphene and Fe-graphene distances differ for different complexes but the differences do not exceed standard deviations of FePc and clusters from the *xy*-plane. Both energetics and geometric parameters show that the van der Waals interaction determines the adsorption in all cases. These results strongly suggests that the system of FePc molecule on the smaller graphene flake can be taken for extremely costly computations with multiconfigutational approach, particularly, in the case when one focuses on iron atom and its closest surrounding.

	Adsorbtion Energy, eV	FePc-Gr dist, Å	Fe-Gr dist, Å
FePc/Gr5x5	-2.03	3.44±0.14	3.41±0.09
FePc/Gr4x4	-1.44	3.36±0.26	3.43±0.14
FePc/Gr3x3	-1.37	3.39±0.38	3.46±0.21
FePc/Pyrene	-1.00	3.28±0.19	3.36±0.07

TABLE 5.2: Adsorption energies and geometrical parameters of FePc/Graphene hybrid structures with various sizes of graphene flakes. The averaged distances between the graphene layer and FePc molecule are given in the third column, whereas the averaged distance between Fe atom and C atoms belonging to the graphene flake are depicted in the forth column. Absolute error values have been calculated as a standard deviation from a mean z-coordinate of the layer and the molecule.

5.1.3 Pyrene

Pyrene ($C_{16}H_{10}$, Fig. 5.2A) consists of four tight aromatic rings. It is the smallest carbon structure that can contain studied defects. Some of these defects have already been studied. The DFT study of the Stone-Wales defect in pyrene (Fig. 5.2B) shows[104] that the 8.26 eV energy barrier should be overcome to form a bond while the energy difference between pyrene and Stone-Wales pyrene is 2.35 eV. It has also been shown that the additional hydrogen atom on one of the central pyrene carbon atoms lowers the energy barrier to 6.6 eV. The substitution of two central carbon

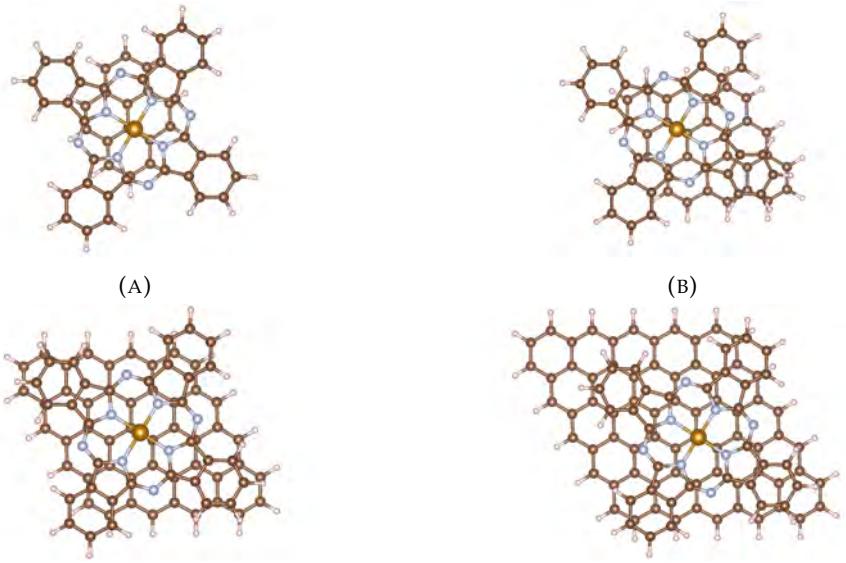

(A) (B)

(C) (D)

FIGURE 5.1: Structures of FePc/Graphene hybrid systems with various sizes of graphene flakes: different graphene areas: (A) FePc/Graphene2x2(Pyrene), (B) FePc/Graphene3x3, (C) FePc/Graphene4x4, (D) FePc/Graphene5x5.

atoms into boron and nitrogen atoms has been done experimentally[105, 106] and this system exhibits excellent stability.

(A) (B)

FIGURE 5.2: Structures of (A) pyrene and (B) pyrene with a Stone-Wales defect

5.1.4 Defects in Graphene

Let us now analyse various defects in graphene. First, we consider Stone-Wales 5-7 defect (hereafter indicated as graphene-SW), and substitutional impurities B,N, and S on carbon site. Further on, we consider more complex defects where B, N, or S substitute the carbon atom in the Stone-Wales defect area. These defects are indicated as B-SW, N-SW, and S-SW. The simple substitutional defects, as well as X-SW defects are depicted in Fig. 5.3A and 5.3B, respectively.

As the host of these defects we consider three systems: (i) graphene supercell with periodic boundary conditions, (ii) the graphene cluster with edge carbon atoms saturated by hydrogen, and (iii) pyrene molecule. For pristine graphene, the DFT calculations, for all three systems listed above, predict the carbon-carbon bond length to be 1.42 Å. The optimised geometry of all 7 types of defects in three host types is summerised in Tables 5.3 and 5.4. It should be noted that all defected structures have a flat geometry. Calculations using cluster and periodic conditions, as well as the pyrene molecule generally show similar results. In the case of a doping atom, the

bonds of the added atom with neighbouring carbon atoms are lengthened, whereas the bonds closest to the C-C defect are shortened. The Stone-Wales defect forms a bridge between pentagons and this bond is shorter than the standard bond in graphene. With the addition of a boron, nitrogen, or sulphur atom, this bridge bond increases, but remains shorter than the bonds of the doped atom with the rest of the carbon atoms. These effects are most visible in the case of sulphur doping, whereas for boron and nitrogen atoms these changes are rather tiny.

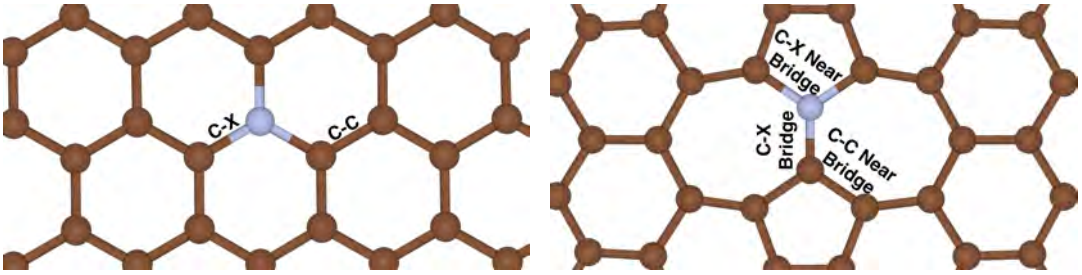

(A) (B)

FIGURE 5.3: Structures of studied graphene defects; (A) doped graphene, (B) graphene with the Stone-Wales graphene and doping.

	C-X bond length, Å			C-C bond length, Å		
	Periodic	Cluster	Pyrene	Periodic	Cluster	Pyrene
Gr-B	1.49	1.49	1.53	1.41	1.41	1.41
Gr-N	1.41	1.4	1.43	1.42	1.42	1.42
Gr-S	1.6	1.6	1.76	1.4	1.4	1.39

TABLE 5.3: Geometric parameters of substitutional impurities of boron, nitrogen, and sulphur atom. "C-X" bond length is an average length between the impurity atom and adjacent carbon atoms; "C-C" bond length is the average length of the closest to the defect carbon bonds.

It has been already recognised that the formation of the Stone-Wales defect in graphene leads to the displacement of atoms in the transverse direction.[107, 108, 39] Transverse bends can occur in the sinusoidal (sinlike) and cosinusoidal (coslike) phases. The first configuration corresponds to the energy minimum, however, a small barrier height between two positions leads to rapid transitions between the two configurations. Our calculations show that potential energies differ from the flat structure by 0.2 and 0.1 eV for sinlike and coslike configurations, respectively. The formation energy of the flat Stone-Wales defect (the difference between the energies of cells with and without the defect) is 4.34 eV. In particular, the out-of-plane effect is difficult to detect experimentally using STM methods, since the two structures are layered on top of each other and, as a result, the defect appears flat. The above effects were taken into account when optimising the FePc/Gr structure. As a result of optimisation, in both sinlike and coslike cases, the graphene layer was flattened, and the energy and geometric characteristics differ insignificantly from the optimised structural parameters of the FePc/Gr system with flat graphene. Therefore, in the future, the energy of graphene in the adsorption equation (Eq. 3.3) will be understood as the energy of flat graphene and all further optimisations will be carried out with the flat graphene structure as the initial one.

	Periodic	Cluster	Pyrene
C-X Bridge bond length, Å			
Gr-SW	1.33	1.35	1.38
Gr-B-SW	1.4	1.43	1.48
Gr-N-SW	1.33	1.36	1.4
Gr-S-SW	1.56	1.6	1.71
C-X Near Bridge bond length, Å			
Gr-B-SW	1.52	1.53	1.55
Gr-N-SW	1.42	1.42	1.42
Gr-S-SW	1.63	1.65	1.70
C-C Near Bridge bond length, Å			
Gr-SW	1.46	1.47	1.47
Gr-B-SW	1.43	1.44	1.44
Gr-N-SW	1.44	1.45	1.45
Gr-S-SW	1.41	1.42	1.40

TABLE 5.4: Geometric parameters of the Stone-Wales defect, as well as combined Stone-Wales defects with doped boron, nitrogen, and sulphur atom. "C-X Bridge" bond length is a length between the pentagons; "C-X Near Bridge" bond length is an average length of a doped atom with neighbouring carbon atoms; "C-C Near Bridge" bond length is an average length between a carbon atom located on the bridge with other carbon atoms.

To assess the stability of the studied defects, cohesion energies (Eq. 3.2) were calculated for cluster and pyrene models; the results of how much the energies of these models are higher than the energy of the cluster (pyrene) without defects are shown in Table 5.5. It can be seen from the results that the formation of defects leads to a decrease in the stability; nevertheless, the Stone-Wales defect and the implantation of a boron atom lead to minor decreases. Doping with a sulphur atom somewhat lowers the stability of the surface. Nevertheless, it has been shown that a formation with a doped sulphur atom is thermodynamically more favourable than a vacancy.[109]

	Cluster cohesive energy, eV	Pyrene cohesive energy, eV
Gr-SW	0.035	0.08
Gr-B	0.029	0.13
Gr-SW-B	0.059	0.17
Gr-N	0.037	0.20
Gr-SW-N	0.069	0.16
Gr-S	0.111	0.40
Gr-SW-S	0.132	0.39

TABLE 5.5: Cohesive energies relative to pristine graphene for the cluster and pyrene with studied defects.

5.2 FePc/Graphene

5.2.1 FePc on Graphene and Graphene-SW

The hybrid system FePc/Gr with the FePc molecule placed over the graphene layer has been studied theoretically.[37] One of the important issues is the molecule

position relative to the graphene layer. Typically, one considers the location of the iron atom above the centre of the carbon ring (Hex), above the carbon atom (Top), and between the carbon atoms at the hexagon's edge (Bridge). It turned out that the Top and Bridge positions are more favourable and have extremely similar physisorption energies. Optimisation performed in our QE computations does not allow us to really accurately point out the energetically most favourable structure, but the geometries of the Top and Bridge structures are nearly identical.

Since the interaction of TMPc's with Stone-Wales defected graphene (hereafter referenced to as graphene-SW) has not been experimentally studied with STM, the question of the molecule location is not obvious. When studying the location of different metal atoms on the Stone-wales defect, the most stable configurations were achieved at the centres of pentagons and heptagons, as well as at the rotated C-C bond.[110] Taking this into account, we calculated the two-dimensional potential energy surfaces of the system with a shift of the molecule by 2.25 Å along the vertical and horizontal axes from the centre of the defect with a step of 0.25 Å. The results obtained indicate that the most favourable position for all cases is where the metal atom of the TMPc molecule is located above the C-C defect-forming bond (Fig. 5.4A). A more accurate calculation with a step of 0.2 Å in the vicinity of the defect specifies the position of the molecule (Fig. 5.4B). Before optimising the system, the preliminary calculations were performed and the approximate distance between graphene and FePc was found. Also, the molecule's rotarions around its own axis were examined to find the preliminary molecule position relative to graphene layer, which is then used as the starting point for complete optimisation of the hybrid system's geometry performed automatically in the QE numerical code. Such two-step procedure of the geometry optimisation sheds light on the dependence of the system's energy on a particular geometric parameter.

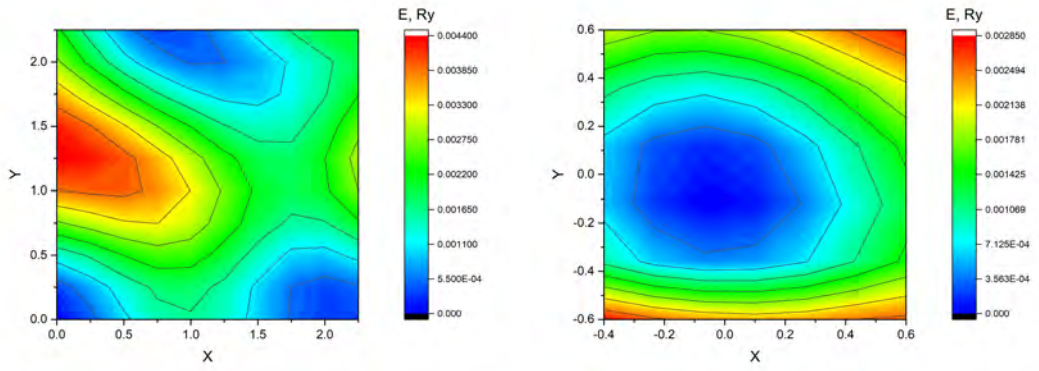

(A) (B)

FIGURE 5.4: Potential energy surfaces of FePc/Gr-SW. The shifts of the molecule on graphene in horizontal directions are marked along the axes. The position (0,0) corresponds to the location of the metal atom between two defect-forming carbon atoms. The step is (A) 0.25 Å, and (B) 0.2 Å.

The geometrically optimised structure of the FePc/Graphene-SW system (see Fig. 5.5B, and 5.6B) similar to the geometry for a structure without the defect (Fig. 5.5A, 5.6A) i.e. FePc/Graphene. The FePc molecule is flat and parallel to the graphene layer. The distances between the molecule and the surface are shown in Table 5.6. The cluster and periodic models give similar results. A decrease in the cluster size down to the pyrene molecule leads to a reduction in the distance between the molecule

and the cluster. The Stone-Wales defect does not significantly change the distance between the molecule and the layer. The FePc iron atom is slightly higher than the FePc middle plane in the FePc/Pyrene case. This is explained by the fact that the pyrene area is smaller than the area of FePc, the van der Waals forces do not act on the entire FePc molecule, and because of this, FePc bends slightly.

Energetic characteristics (Table 5.7) between the structures with and without the Stone-Wales defect also do not differ much. This allows us to predict that in experimental studies this defect will not play an important role in the localization of the molecule on the graphene's surface. Of course, this analysis does not take into account the influence of a possible material that is used to support the graphene layer.

	Periodic	Cluster	Pyrene
FePc - Graphene distance, Å			
FePcGr	3.45±0.01	3.44±0.13	3.28±0.19
FePcGr-SW	3.49±0.01	3.44±0.1	3.3±0.1
FePcGr-B	3.49±0.01	3.43±0.15	3.23±0.21
FePcGr-SW-B	3.49±0.03	3.38±0.42	3.26±0.32
FePcGr-N	3.49±0.02	3.41±0.2	3.04±0.28
FePcGr-SW-N	3.50±0.02	3.39±0.44	3.23±0.23
FePcGr-S	3.49±0.01	3.50±0.25	3.35±0.42
FePcGr57-SW-S	3.44±0.51	3.33±0.88	3.36±0.46
Fe - Graphene distance, Å			
FePcGr	3.50±0.01	3.41±0.09	3.37±0.07
FePcGr-SW	3.48±0.01	3.38±0.07	3.40±0.02
FePcGr-B	3.46±0.01	3.29±0.9	3.14±0.13
FePcGr-SW-B	3.45±0.02	3.19±0.26	3.28±0.25
FePcGr-N	3.5±0.01	3.38±0.14	3.21±0.08
FePcGr-SW-N	3.5±0.01	3.32±0.23	3.27±0.11
FePcGr-S	3.44±0.01	3.29±0.2	3.11±0.31
FePcGr57-SW-S	3.66±0.28	3.09±0.50	3.08±0.34

TABLE 5.6: Distances between the graphene layer and the FePc molecule and the Fe atom in FePc/Gr hybrid systems. The absolute error value was calculated as a standard deviation from a mean z-coordinate of the layer and the molecule.

	Periodic	Cluster	Pyrene
FePc/Gr	-2.1	-2.03	-1.00
FePc/Gr-SW	-2.25	-2.02	-0.98
FePc/Gr-B	-2.46	-2.05	-1.14
FePc/Gr-SW-B	-2.09	-2.13	-1.06
FePc/Gr-N	-2.75	-2.01	-1.80
FePc/Gr-SW-N	-1.56	-2.00	-1.09
FePc/Gr-S	-3.52	-4.70	-4.07
FePc/Gr-SW-S	-4.02	-4.40	-2.71

TABLE 5.7: Computed adsorptio energies (in eV) of the FePc molecule to graphene and different types of defected graphene.

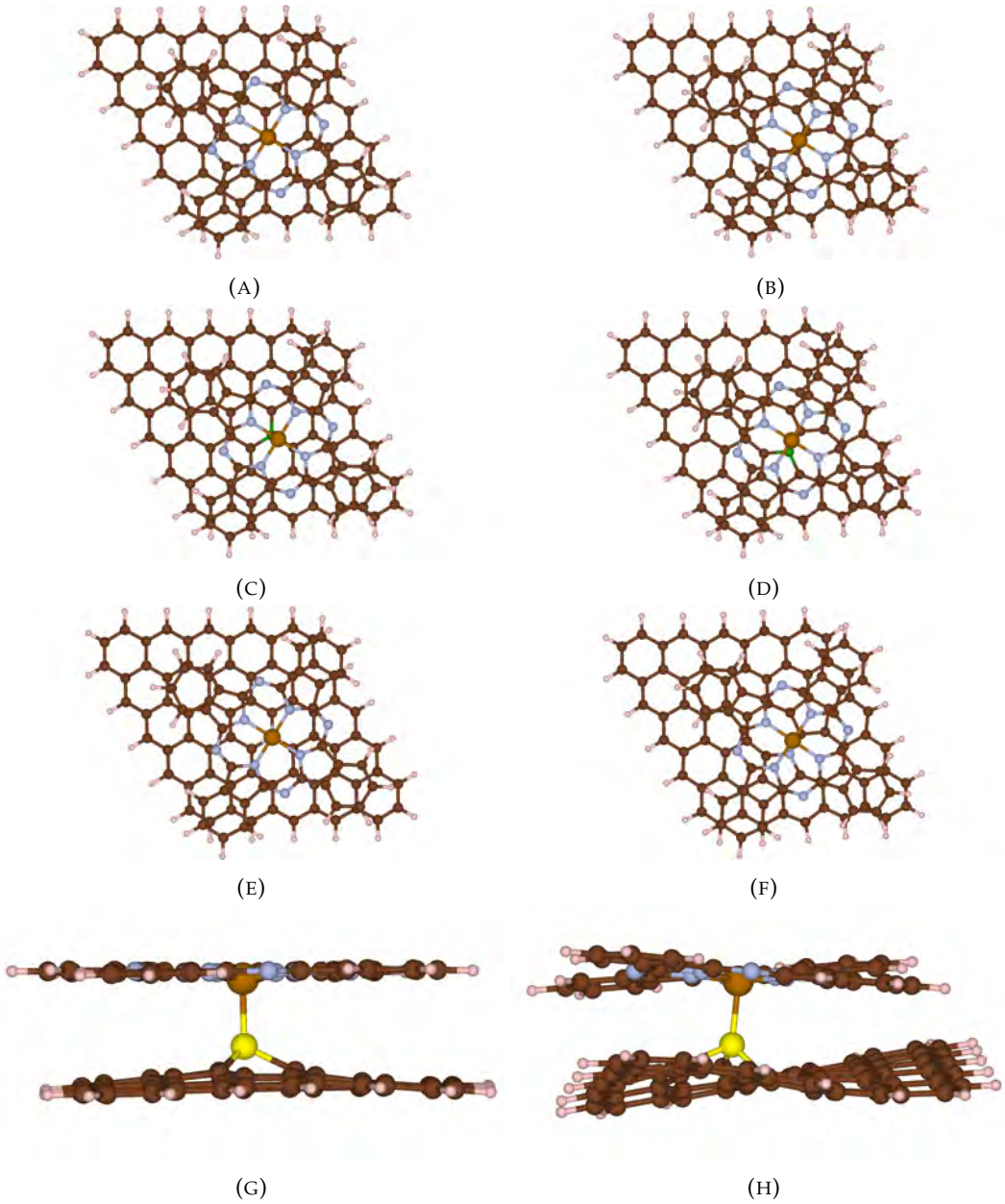

FIGURE 5.5: Views of FePc/Graphene cluster complexes with various types of defects in the graphene layer: A) pristine graphene; and graphene with B) the Stone-Wales defect,) B-doping, D) B-doping + the Stone-Wales defect, E) N-doping, F) N-doping + the Stone-Wales defect, G) S-doping, H) S-doping + the Stone-Wales defect.

5.2.2 FePc on Doped Graphene and Doped Graphene-SW

Doping of graphene with the boron atom also does not distort the flat geometry of the structure (Fig. 5.5C, 5.6C). The geometry of the system generally has the same form; the molecule remains bound to the graphene surface only by van der Waals forces. The same applies to the case of doping a boron atom into the Stone-Wales defect (Fig. 5.5D, 5.6D). The position of the FePc molecule over the defects is also retained in both cases. Adsorption energies are comparable to the cases without defects for all studied graphene representations.

FePc/Graphene hybrid structures with nitrogen doping (Fig. 5.5E, 5.5F, 5.6E,

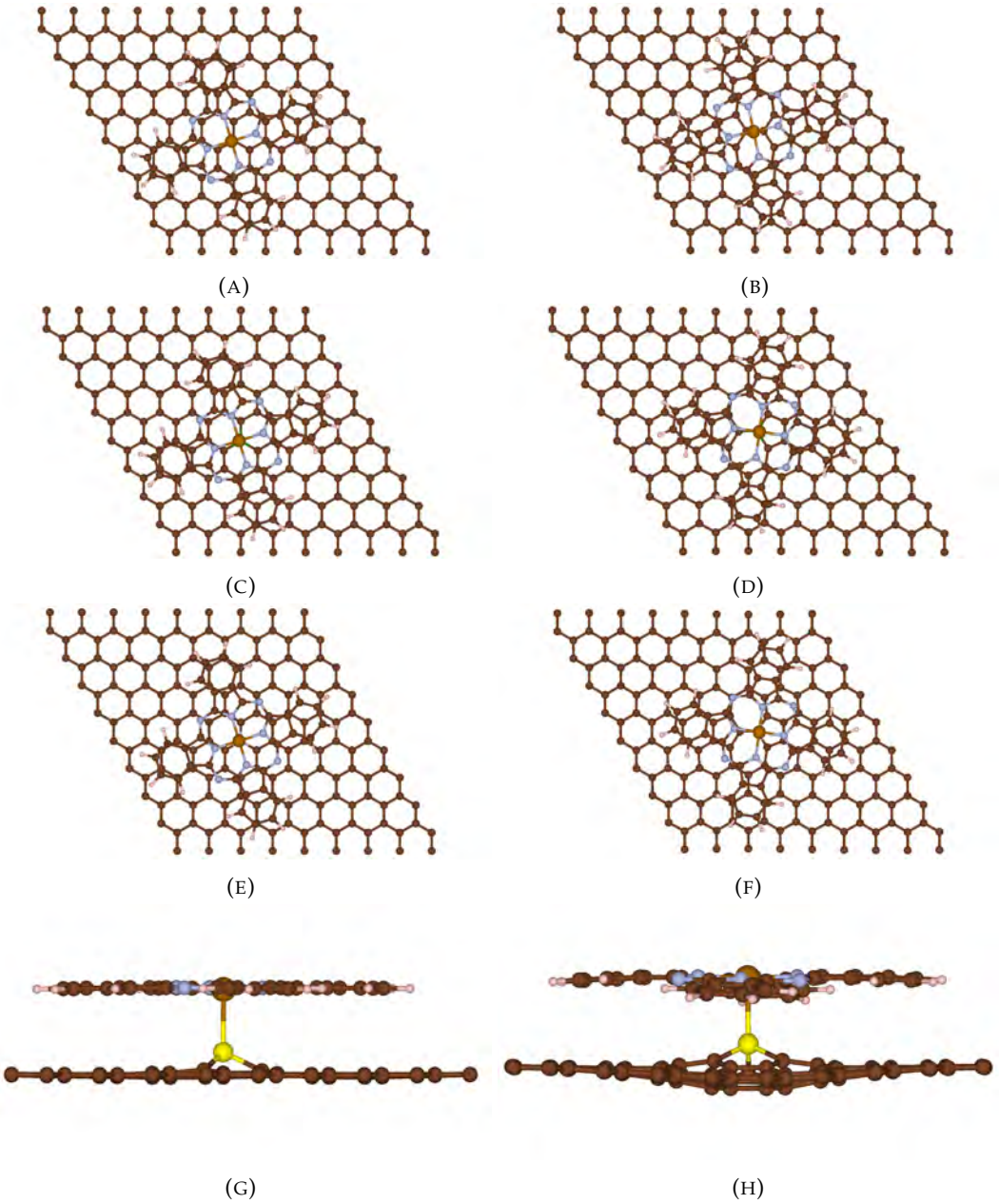

FIGURE 5.6: Periodic cell views of FePc/Graphene complexes with various types of graphene layer: A) pristine graphene; and graphene with B) the Stone-Wales defect, C) B-doping, D) B-doping + the Stone-Wales defect, E) N-doping, F) N-doping + the Stone-Wales defect, G) S-doping, H) S-doping + the Stone-Wales defect.

5.6F) also remain flat but the geometric and energetic parameters change more significantly. For the periodic FePc/Gr-N structure the adsorption energy is about 30% higher, while for FePc/Gr-SW-N it is 26% lower. The increase of adsorption energy for FePc/Pyrene-N is about 80%, while there is no energy decrease for FePc/Pyrene-SW-N case. In comparison with periodic and pyrene models, adsorption energies of B- and N- defected FePc/Graphene cluster models do not really differ from non-defected FePc/Graphene.

Doping the graphene layer with of the sulphur atom, in turn, leads to serious changes in the geometry of the hybrid system. The sulphur atom moves out of the

graphene plane and forms a bond with the iron atom. Figures 5.5G, 5.5H, 5.6G, 5.6H show side projections, which show the geometric transformations of these systems. In the case of the system with simple sulphur doping, the graphene layer retains a flat view, while the graphene with the sulphur atom doped into the Stone-Wales defect has a wavy shape. Due to the formation of the Fe-S bond the adsorption energy of the molecule onto the substrate increases substantially. It is observed for all substrate representations and the value of adsorption energies is similar are comparable.

5.2.3 The Density of States Analysis

Impurities and defects influence the conductive properties of graphene and make it possible to create devices with a controlled small band gap. Thus, the replacement of one of the carbon atoms with a boron or nitrogen atom leads to p- and n-type conductivity, respectively.[111, 112] According to theoretical studies, the formation of the SW defect leads to the appearance of a small band gap (0.08 eV), while the material is still characterized by high conductivity, and the graphene-SW-B and graphene-SW-S systems show conductive properties.[62] According to the calculations performed in this thesis (Fig. 5.7), the band gap for graphene with the SW defect is 0.16 eV. Doping the SW defect with boron and sulphur atoms (*i.e.*, creating SW-B and SW-S defects) reduces the band gap to 0.1 eV in both cases. The band gaps slightly differ from the values cited in the literature but these results depend on the concentration of defects on the surface.

The density of states of the periodic FePc/Gr systems (Fig. 5.8) and the projected density of states of the iron atom d-orbital in the FePc molecule (Fig. 5.9) indicate that the presence of the molecule does not change the band gap of graphene. The van der Waals interaction between FePc and graphene does not fundamentally disturb the electronic structure of pristine and defected graphene layers. In turn, various defects in graphene lead to redistributions of the density of states of the iron atom d-orbitals in the FePc, while not changing the total magnetic moment. It should be noted that in the case of the systems with boron doping in the pure graphene and in the graphene with the Stone-Wales defect, the contributions to the density of states originating from the d-orbital of the iron atom is observed near the Fermi energy. In such cases, a charge transfer occurs from the graphene layer to the FePc molecule. The d-orbital acts as an impurity state that is inside the band gap.

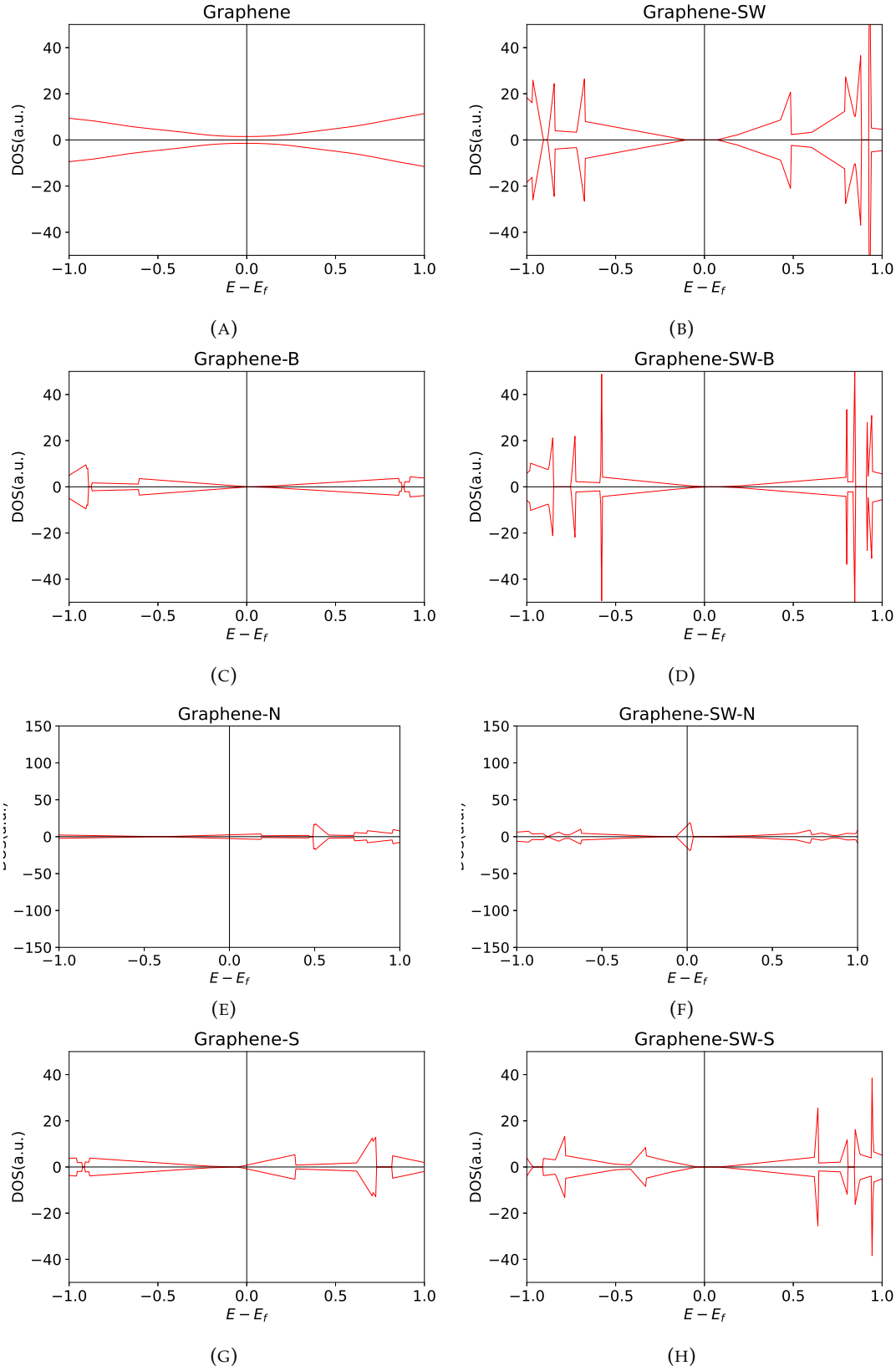

(A) (B) (C) (D) (E) (F) (G) (H)

FIGURE 5.7: Densities of states for studied pristine and defected graphene layers. The type of defect is listed above the frame in each panel.

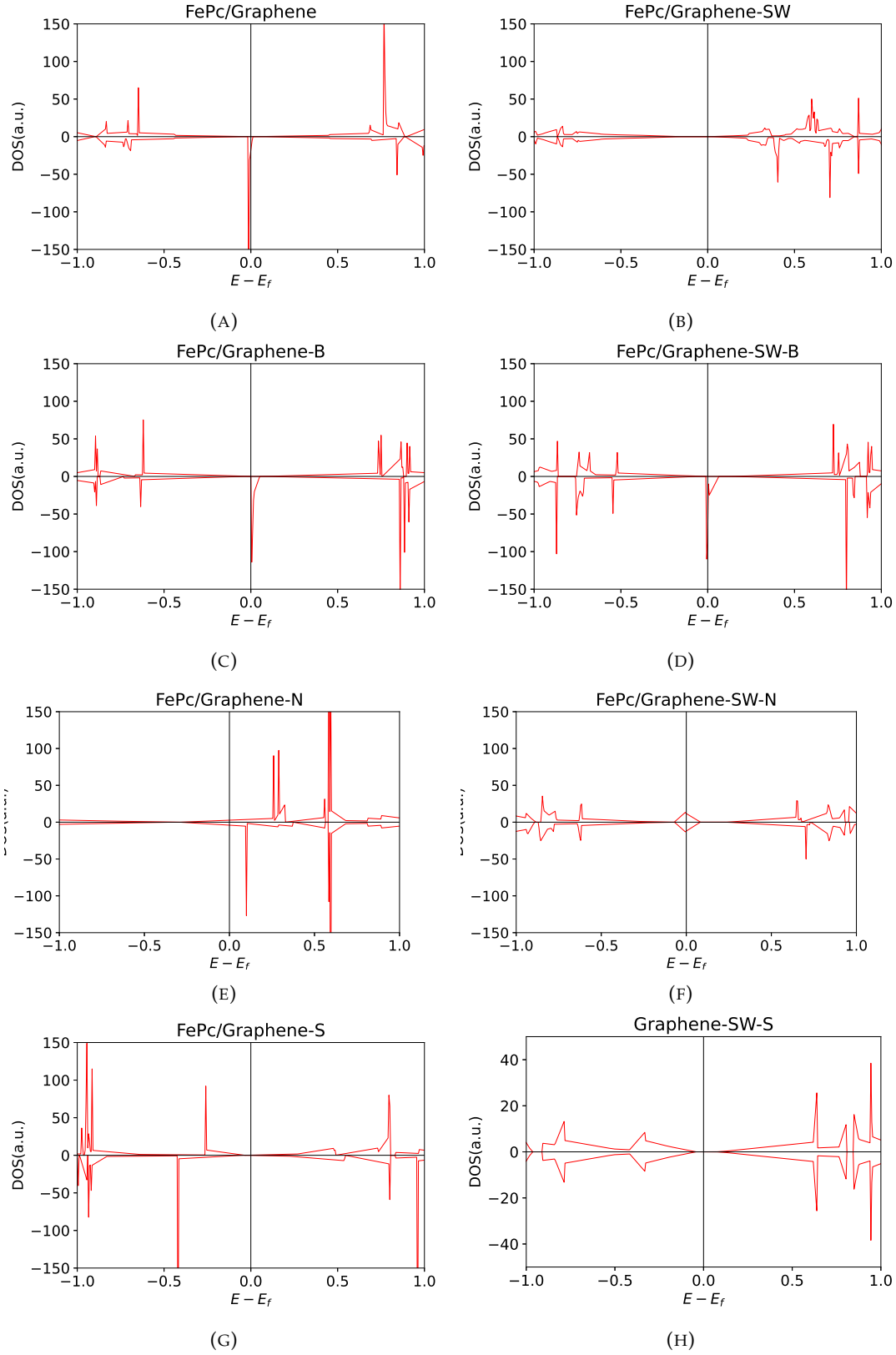

(A) (B) (C) (D) (E) (F) (G) (H)

FIGURE 5.8: Densities of states for studied hybrid systems consisting of FePc molecule adsorbed to pristine and defected graphene layers. The type of defect is listed above the frame in each panel.

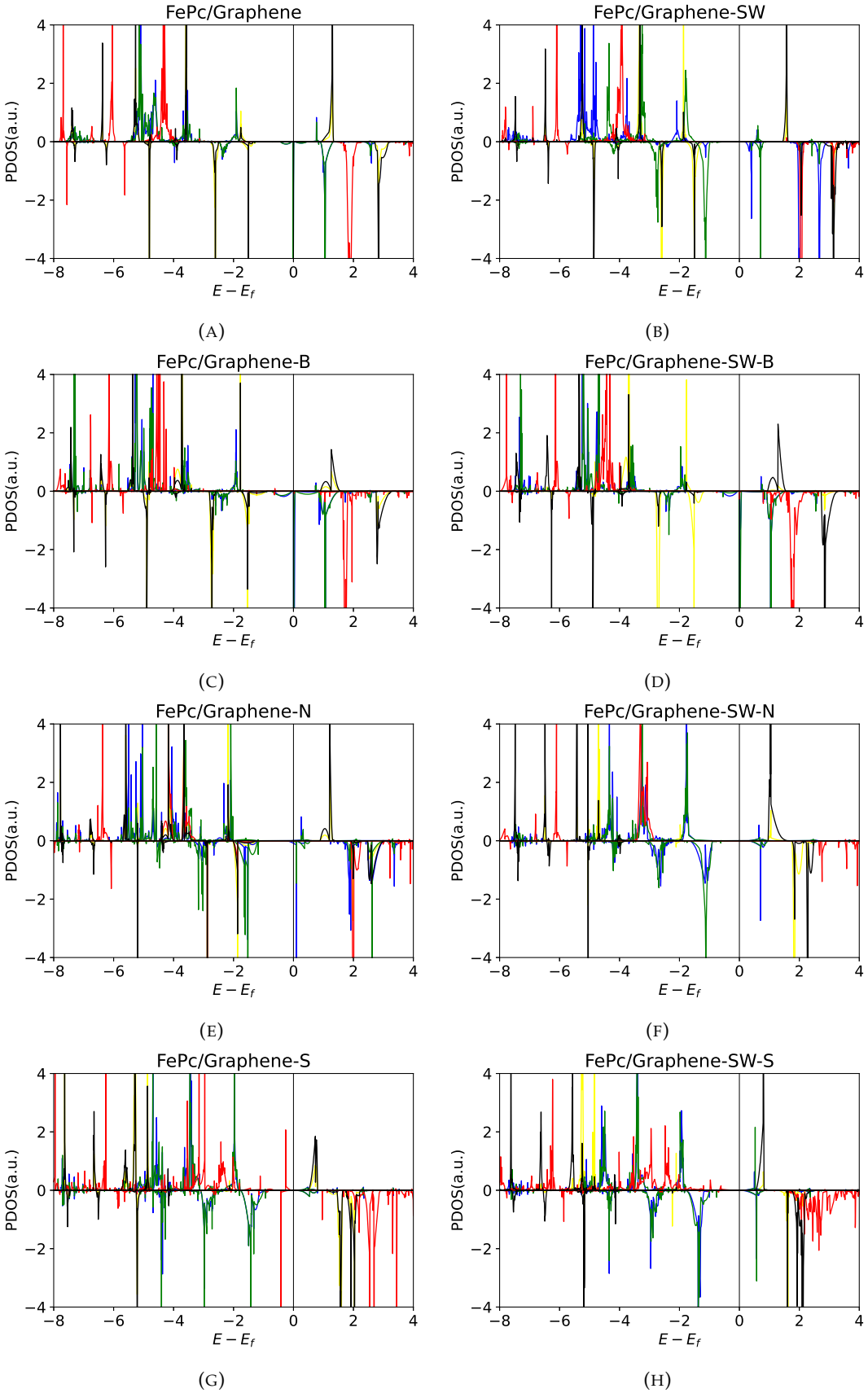

(A) (B) (C) (D) (E) (F) (G) (H)

FIGURE 5.9: Projected densities of states for the iron atom d-orbitals in studied FePc/Graphene layers listed above the frame in each panel (yellow - d_{xy}, blue - d_{xz}, green - d_{yz}, red - d_{z^2}, black - $d_{x^2-y^2}$). For clarity of the pictures, the gaussian broadening parameter of the order of the energy grid step (0.005 eV) has been chosen.

5.2.4 Spin Distribution in Clusters

In the case of the cluster approach, it is possible to track changes occurring in the distribution of atomic orbitals, since the wave functions are represented in the LCAO form. As a result, the d-shell of the iron atom in FePc retains its configuration ${d_{xy}}^2{d_{xz}}^2{d_{yz}}^1{d_{z^2}}^1{d_{x^2-y^2}}^0$ in the cases of the presence of the molecule on pure graphene, graphene with the Stone-Wales defect, and also in both cases of doping with boron and nitrogen atoms.

The case with a doped sulphur atom deserves a separate consideration. These systems were considered in singlet, triplet, and quintet states. Moreover, in each of these systems, there is no spin moment on the sulphur and iron atoms. As the multiplicity of the system increases, the spin moment is distributed on the graphene surface, and the total energy of the system increases. These results are inconsistent with the results we obtained with the periodic approach, but on the other hand similar results were obtained in another study.[38]

Also, existing studies of the solid-state structures of iron sulfide[113, 114, 115, 116, 117, 118] show that such compounds do not exhibit magnetic properties. In turn, the magnetic order of iron boride[113, 119] is ferromagnetic. These results suggest that the nature of the interaction of the FePc molecule with S-doped graphene is rather nonmagnetic, but this requires experimental studies and calculations based on the multiconfigurational approach.

Chapter 6

FePc/Pyrene: Multireference Studies

One of the serious deficiencies of the standard DFT theory is the fact that it is not applicable to the degenerated ground states of quantum systems, such as systems with unfilled shells of transition metals. In such cases, the Slater determinant used for the many-electron wave function in the Kohn-Sham realisation of DFT is not an eigenfunction of the systems $\hat{S}^2$ spin operator. Since magnetic features of the studied hybrid systems (such as e.g. anisotropy constants) are essential for their potential applications as memory cells, we decided to go beyond the standard DFT in this thesis and describe studied hybrid structures involving magnetic molecules on the ground of a so-called multireference theory. To realise these goals, we employ the complete active space self-consistent field (CASSCF) computational scheme in combination with second order n-electron valence state perturbation theory (NEVPT2) as implemented in the *ORCA* computational package. The standard CASSCF scheme reproduces the energies of the excited states rather inaccurately. Therefore, additional perturbation theory calculations by the NEVPT2 method are necessary.

Unfortunately, all multiconfigurational theories are computationally very demanding. Since we are not able to study within the NEVPT2 method so large systems as we have done employing the DFT computations, we have decided to investigate the FePc/Pyrene system, where four benzene rings of pyrene should mimic the graphene substrate.

The *ORCA* implementation of CASSCF is only for finite systems. Therefore, in the previous chapter, we performed a detailed analysis of the hybrid systems within DFT theory for various boundary conditions.

This analysis corroborates that all features concerning morphology and energetics of the systems remain mostly identical and independent of the boundary conditions used. Also, FePc/Pyrene system exhibits, at least qualitatively, properties analogous to the properties of hybrid systems where the FePc molecule is adsorbed at a larger number of hexagonal rings.

Below, we present details of these novel studies in the context of the hybrid systems of a magnetic molecule and a substrate.

6.1 Initial Guess

One of the most important aspects at the beginning of CASSCF calculations is the choice of the orbitals for the active space. In *ORCA* the default is “PModel” which uses a diagonalized LDA DFT matrix as an initial guess. It is also recommended to use “PAtom” which gives atomic orbitals with an extended Hückel like ordering.

These automatic models failed in searching the active space for the FePc-graphene system. However, "PAtom" gave good results for the pure FePc molecule.

Quasi-restricted orbitals from the DFT analysis could also be used as an initial guess. The initial orbitals were obtained from the results of DFT calculations with PBE functional. The first CASSCF calculation choses the orbitals close to the HOMO-LUMO gap as active. We are interested in the d-orbital static interaction, therefore, we chose missing d_{xy} and $d_{x^2-y^2}$ orbitals from internal and external orbitals manually. The choice of orbitals was non-obvious because there were no clean molecular orbitals corresponding to atomic d_{xy} and $d_{x^2-y^2}$ orbitals and it makes the study not reliable. Despite the facts that the ground state is correct ($d^2_{xy}d_{xz}^2d_{yz}^1d^1_{z^2}d^0_{x^2-y^2}$), the strong mixture of iron atomic orbitals with phthalocyanine molecular orbitals complicates the study of the system. First excited states of the molecule are singlet instead of triplet A_{2g} and E_g states. This is in disagreement to the previous studies of the molecule.[103] Moreover, during the FePc/Graphene and FePc/Pyrene analysis, it was not possible to identify all iron 3d-orbitals in molecular orbitals. Because of that we decided to employ a different procedure.

The method of constructing initial orbitals for further analysis that works quite well is so-called *the fragment derived guess*.[**aravena2019casscf**] This method assumes the fragmentation of the molecular complex into ligand, and metal centre parts. Molecular orbitals are obtained for each fragment, where ligand and metal orbitals are found using DFT and CASSCF methods, respectively. Then the resulting orbitals are merged for further calculations. This method allows for the use of orbitals based on pure metal once in the analysis.

The fragment derived guess works well for systems where a multiplicity of a ligand is odd. In this case, a first CASSCF calculation can be performed using only metal *d*-orbitals as active CAS(6,5), where 6 is a number of electrons and 5 is a number of orbitals. Then the active space can be expanded using the ligand orbitals to CAS(10,9). The difficulty is that the CASSCF method requires full occupation of core orbitals. It means that FePc/Pyrene systems with an odd number of electrons in defects (B- and N-dopings) can not be treated using the CASSCF method with only metal *d*-orbitals in the active space. The solution to this problem was the gradual inclusion of orbitals in space. After the fragment derived guess analysis, such systems were studied using CASSCF(5,5), where one electron was removed from the *d*-orbital active space. Then the active space was expanded systematically to CAS(7,6) $\rightarrow$ CAS(9,7) $\rightarrow$ CAS(9,8) $\rightarrow$ CAS(11,9). The results of final calculations usually show the occupation of iron *d*-orbitals as in the usual FePc molecule, and the auxiliary assumption of the removal of one electron from the iron *d*-shell disappeared. The results of the final calculations show that the auxiliary assumption about the removal of one electron from the iron *d*-shell has disappeared and the electron density in the *d*-shell is quantitatively similar to the electron density for the free standing FePc molecule.

6.2 FePc

The free standing FePc molecule has been studied using different complete active spaces: CAS(6,5) and CAS(10,9). In the first case, only iron *d*-orbitals are in the active space, in the second case two orbitals from the core space and two from set of valence orbitals are added. The active molecular orbitals for CAS(10,9) are shown in Fig. 6.1. The graphical comparison between iron *d*-orbitals energies in CAS(6,5) and CAS(10,9) is presented in Fig. 6.2. Unfortunately, the addition of energetically nearest ligand orbitals to the active space destroys the symmetry and d_{xz} and d_{yz} orbitals

are not degenerated anymore. Also, the expansion of CAS moves d_{xy} and $d_{x^2-y^2}$ apart. Energies of molecular electronic transitions (Table 6.1) decrease when the active space is expanded. During first transitions, the electron configuration changes only on the iron d-shell and the expansion of CAS does not change their order.

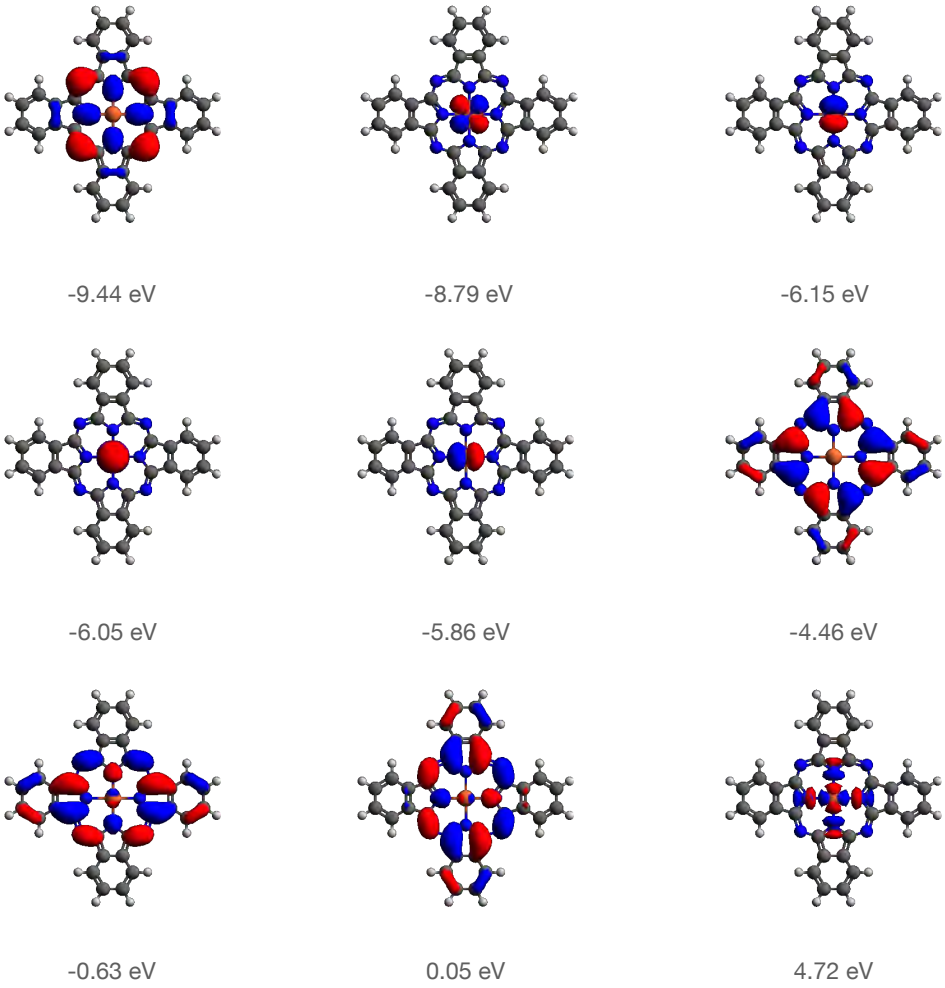

FIGURE 6.1: FePc active molecular orbitals in CAS(10,9) and their energies. Red and blue colours mean positive and negative charged densities, respectively.

6.3 FePc/Pyrene

Multi-reference calculations of the FePc/Pyrene hybrid system using CAS(6,5) were done only for the following forms of pyrene: pure pyrene, pyrene with the SW defect, S-doping, and the combined SW-S defect. The active molecular orbitals energies (energies of iron d-orbitals) are graphically shown in Fig. 6.3 and the description of molecular electronic transitions are in Table 6.2. The results with extended CAS(10,9) for the system with these defects and for FePc/Pyrene(-SW)-B and FePc/Pyrene(-SW)-N using CAS(11,9) are in Fig. 6.4 and Table 6.3. Views of 9 active molecular orbitals for FePc/Pyrene and all studied defects are presented in Figs. 6.5, 6.6,6.7, 6.8, 6.9, 6.10, 6.11, 6.12.

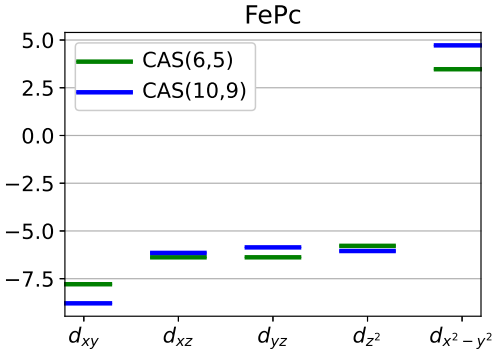

FIGURE 6.2: Energies (in eV) of the iron d-shell orbitals in the FePc molecule; green lines present the results using CAS(6,5), where all 5 orbitals in the active space are iron d-orbitals, blue lines correspond to the results using CAS(10,9) where 4 ligand orbitals were added.

	CAS(6,5)			CAS(10,9)		
System	ν	State	2S+1	ν	State	2S+1
FePc	—	$d^2_{xy}d^1_{xz}d^1_{yz}d^2_{z^2}d^0_{x^2-y^2}$	3		$d^2_{xy}d^1_{xz}d^1_{yz}d^2_{z^2}d^0_{x^2-y^2}$	3
	738	$d^2_{xy}d^1_{xz}d^2_{yz}d^1_{z^2}d^0_{x^2-y^2}$	3	615	$d^2_{xy}d^1_{xz}d^2_{yz}d^1_{z^2}d^0_{x^2-y^2}$	3
	738	$d^2_{xy}d^2_{xz}d^1_{yz}d^1_{z^2}d^0_{x^2-y^2}$	3	677	$d^2_{xy}d^2_{xz}d^1_{yz}d^1_{z^2}d^0_{x^2-y^2}$	3
	3307	$d^1_{xy}d^1_{xz}d^1_{yz}d^2_{z^2}d^1_{x^2-y^2}$	5	3226	$d^1_{xy}d^1_{xz}d^1_{yz}d^2_{z^2}d^1_{x^2-y^2}$	5
	4978	$d^1_{xy}d^1_{xz}d^2_{yz}d^1_{z^2}d^1_{x^2-y^2}$	5	4442	$d^1_{xy}d^1_{xz}d^2_{yz}d^1_{z^2}d^1_{x^2-y^2}$	5
	4978	$d^1_{xy}d^2_{xz}d^1_{yz}d^1_{z^2}d^1_{x^2-y^2}$	5	4531	$d^1_{xy}d^2_{xz}d^1_{yz}d^1_{z^2}d^1_{x^2-y^2}$	5

TABLE 6.1: FePc NEVPT2 transition energies ν (in cm^{-1}) relative to the ground state energy; d-orbital configurations of ground and excited states calculated using CAS(6,5) and CAS(10,9), and their multiplicities 2S+1.

In general, the presence of the usual pyrene molecule barely changes the electronic properties of FePc. The energies of iron d-orbitals in FePc/Pyrene do not change a lot by introducing the SW defect. Electron occupations remain the same for ground and the first five excited states, exactly as in the case of the pure FePc molecule. Molecular orbitals corresponding to pyrene are not inside the expanded active space CAS(10,9) and their energy levels are quite far from the expanded active space energy levels. It is only noticed that in the case of the SW defect, the transition energies to excited states slightly increase.

The FePc/Pyrene hybrid system with B-doped pyrene has a denser distribution of iron d-orbitals energies in comparison with the FePc/Pyrene with undoped pyrene. The d_{z^2} orbital is on the same energy level as d_{xy}. The boron atom has an unpaired electron in the ground state. First excited electronic states are characterised by the changing of the iron d-orbitals occupation, while electron occupation of the boron atom remains the same. The first excited state and the ground state have a small transition energy between each other and different multiplicities (the ground state is doublet $2S+1=2$ and the excited state is quartet $2S+1=4$). For the system with the SW defect, the states have the same iron d-orbital occupation $d^2_{xy}d^1_{xz}d^1_{yz}d^2_{z^2}d^0_{x^2-y^2}$ and $\nu = 26cm^{-1}$. The transition energy between these states is

quite small and it is hard to recognise the real ground state spin moment of the system (previous researchers predicted[38] the total magnetic moment equals 3 μ_B for FePc/Graphene-B periodic structure which corresponds to a quartet while we obtained doublet).In contrast to this, for pure FePc the transition energy between the states $d^2_{xy}d^1_{xz}d^1_{yz}d^2_{z^2}d^0_{x^2-y^2}$ with different multiplicities (3 and 1) is 11628 cm^{-1}.

The complexes with N-doped atoms exhibit similar behaviour, the complex without the SW defect has the same iron electron occupations $d^2_{xy}d^1_{xz}d^1_{yz}d^2_{z^2}d^0_{x^2-y^2}$ in the ground and first excited states, and the transition energy between them is just $25cm^{-1}$. The excitation energy of the complex with the SW defect is much higher. The nitrogen atom has an unpaired electron in the ground state and in first excited states by analogy with doped boron complexes. The SW defect changes the order of molecular orbitals energies corresponding to $d_{xz}d_{yz}d_{z^2}$ iron orbitals from ascending to descending. This can be associated with changes in geometry.

The doping of the pyrene molecule with sulphur atom also strongly changes the electronic properties of the FePc/Pyrene complex. The iron d_{z^2} orbital is not on the energy level of $d_{xz}d_{yz}$ anymore, and it is much higher. In turn, d_{xz} and d_{yz} orbitals become closer to d_{xy}. As a result, in the ground state, the iron d-shell has the occupation $d^2_{xy}d^2_{xz}d^2_{yz}d^0_{z^2}d^0_{x^2-y^2}$, and the ground state is not spin-polarised. The energy of the first excitation is quite high here in comparison with other studied cases, and the first excited state corresponds to a triplet. The first excitation energy differs a lot due to the presence of the SW defect (6514 cm^{-1} without the defect and 2520 cm^{-1} with it) and it should be visible well in an experiment.

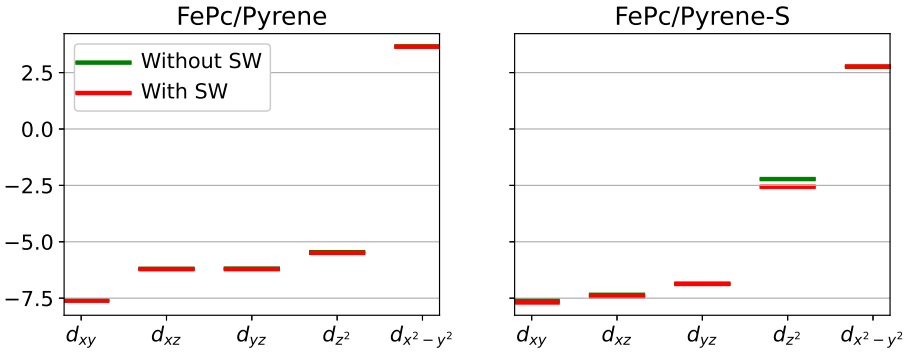

FIGURE 6.3: Energies (in eV) of the levels originating from Fe d-shell orbitals in FePc/Pyrene (left panel), and FePc/Pyrene-S, i.e., S-doped pyrene (right panel) hybrid structures. Calculations were performed employing CAS(6,5), where 5 orbitals in the active space are iron d-orbitals. Green and red lines correspond to pyrene without and with the SW defect, respectively.

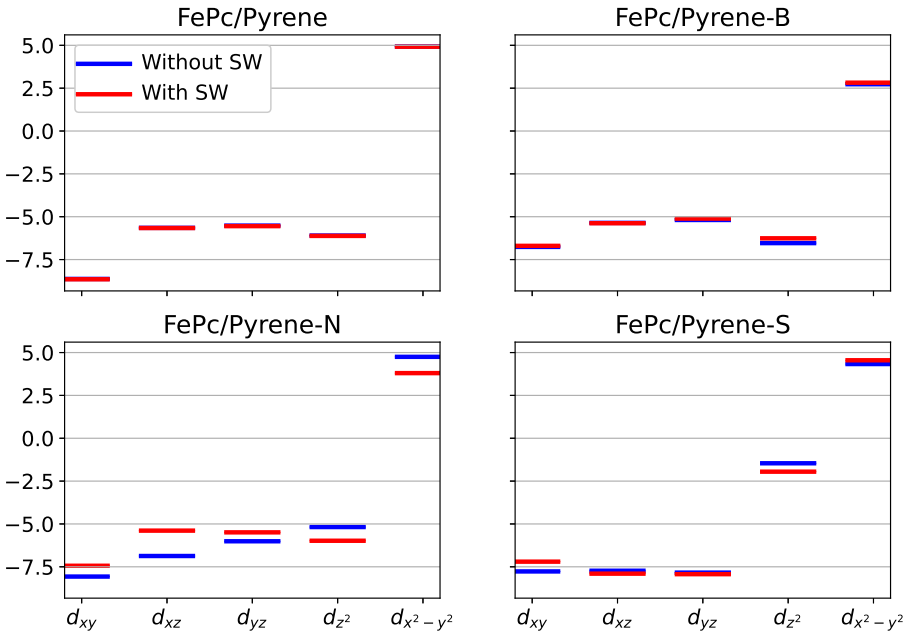

FIGURE 6.4: Energies (in eV) of the levels originating from Fe d-shell orbitals in FePc/Pyrene hybrid systems calculated using CAS(10,9) for FePc/Pyrene and FePc/Pyrene-S; CAS(11,9) for FePc/Pyrene-B and FePc/Pyrene-N. Five orbitals in the active space are iron d-orbitals and four orbitals are ligand ones. Blue and red lines correspond to pyrene without and with the SW defect, respectively.

The ground state of the FePc molecule is the triplet, and it does not change when the molecule is adsorbed to pyrene. The presence of the SW defect in the pyrene also does not change the spin state of the system. Performed NEVPT2 calculations show that studied systems with B- and N-doping have a doublet ground state, whereas systems with sulphur are singlet (Table 6.3). Since the zero field splitting effect appears only in systems with a triplet multiplicity and higher, zero field splitting parameters only for systems with triplet states (FePc, FePc/Pyrene, FePc/Pyrene-SW) are presented in Table 6.4. The FePc molecule has the zero field splitting axial component equals to $D = 90cm^{-1}$ and the transversal component $E = 0cm^{-1}$, while the active space consists of only iron d-shell orbitals. The expansion of the active space leads to the increase of the transversal component because new HOMO-LUMO ligand active orbitals break the D_{4h} symmetry of the active space. In FePc/Pyrene complexes pyrene presence lowers the zero field splitting parameter D by several cm^{-1} in comparison to the D value for the free standing FePc molecule. Also the value of the transversal component E increases owing to the reduced symmetry of the hybrid system.

	Without the SW defect			With the SW defect		
System	ν	State	2S+1	ν	State	2S+1
FePc-Pyrene	—	$Fe\left(d^2_{xy}d^1_{xz}d^1_{yz}d^2_{z^2}d^0_{x^2-y^2}\right)$	3	—	$Fe\left(d^2_{xy}d^1_{xz}d^1_{yz}d^2_{z^2}d^0_{x^2-y^2}\right)$	3
	176	$Fe\left(d^2_{xy}d^1_{xz}d^2_{yz}d^1_{z^2}d^0_{x^2-y^2}\right)$	3	185	$Fe\left(d^2_{xy}d^1_{xz}d^2_{yz}d^1_{z^2}d^0_{x^2-y^2}\right)$	3
	197	$Fe\left(d^2_{xy}d^2_{xz}d^1_{yz}d^1_{z^2}d^0_{x^2-y^2}\right)$	3	232	$Fe\left(d^2_{xy}d^2_{xz}d^1_{yz}d^1_{z^2}d^0_{x^2-y^2}\right)$	3
	3284	$Fe\left(d^1_{xy}d^1_{xz}d^1_{yz}d^2_{z^2}d^1_{x^2-y^2}\right)$	5	3310	$Fe\left(d^1_{xy}d^1_{xz}d^1_{yz}d^2_{z^2}d^1_{x^2-y^2}\right)$	5
	4379	$Fe\left(d^1_{xy}d^1_{xz}d^2_{yz}d^1_{z^2}d^1_{x^2-y^2}\right)$	5	4458	$Fe\left(d^1_{xy}d^1_{xz}d^2_{yz}d^1_{z^2}d^1_{x^2-y^2}\right)$	5
	4384	$Fe\left(d^1_{xy}d^2_{xz}d^1_{yz}d^1_{z^2}d^1_{x^2-y^2}\right)$	5	4463	$Fe\left(d^1_{xy}d^2_{xz}d^1_{yz}d^1_{z^2}d^1_{x^2-y^2}\right)$	5
FePc-Pyrene-S	—	$Fe\left(d^2_{xy}d^2_{xz}d^2_{yz}d^0_{z^2}d^0_{x^2-y^2}\right)$	1	—	$Fe\left(d^2_{xy}d^2_{xz}d^2_{yz}d^0_{z^2}d^0_{x^2-y^2}\right)$	1
	4217	$Fe\left(d^2_{xy}d^1_{xz}d^2_{yz}d^1_{z^2}d^0_{x^2-y^2}\right)$	3	2610	$Fe\left(d^2_{xy}d^1_{xz}d^2_{yz}d^1_{z^2}d^0_{x^2-y^2}\right)$	3
	4313	$Fe\left(d^2_{xy}d^2_{xz}d^1_{yz}d^1_{z^2}d^0_{x^2-y^2}\right)$	3	2782	$Fe\left(d^2_{xy}d^2_{xz}d^1_{yz}d^1_{z^2}d^0_{x^2-y^2}\right)$	3
	6683	$Fe\left(d^1_{xy}d^2_{xz}d^2_{yz}d^1_{z^2}d^0_{x^2-y^2}\right)$	3	5254	$Fe\left(d^1_{xy}d^2_{xz}d^2_{yz}d^1_{z^2}d^0_{x^2-y^2}\right)$	3
	8003	$Fe\left(d^1_{xy}d^1_{xz}d^2_{yz}d^1_{z^2}d^1_{x^2-y^2}\right)$	5	6453	$Fe\left(d^1_{xy}d^1_{xz}d^2_{yz}d^1_{z^2}d^1_{x^2-y^2}\right)$	5
	8104	$Fe\left(d^1_{xy}d^2_{xz}d^1_{yz}d^1_{z^2}d^1_{x^2-y^2}\right)$	5	6591	$Fe\left(d^1_{xy}d^2_{xz}d^1_{yz}d^1_{z^2}d^1_{x^2-y^2}\right)$	5

TABLE 6.2: NEVPT2 transition energies ν (in cm^{-1}), d-shell configurations, and state multiplicities 2S+1 for the ground and excited states of the studied FePc/Pyrene hybrid systems without the SW defect (left panel) and with the SW defect (right panel). All presented results were obtained employing CAS(6,5), where 5 orbitals in the active space are iron d-orbitals.

	Without the SW defect			With the Stone-Wales defect		
System	ν	State	2S+1	ν	State	2S+1
FePc-Pyrene	—	$Fe\left(d^2_{xy}d^1_{xz}d^1_{yz}d^2_{z^2}d^0_{x^2-y^2}\right)$	3	—	$Fe\left(d^2_{xy}d^1_{xz}d^1_{yz}d^2_{z^2}d^0_{x^2-y^2}\right)$	3
	188	$Fe\left(d^2_{xy}d^1_{xz}d^2_{yz}d^1_{z^2}d^0_{x^2-y^2}\right)$	3	255	$Fe\left(d^2_{xy}d^1_{xz}d^2_{yz}d^1_{z^2}d^0_{x^2-y^2}\right)$	3
	253	$Fe\left(d^2_{xy}d^2_{xz}d^1_{yz}d^1_{z^2}d^0_{x^2-y^2}\right)$	3	306	$Fe\left(d^2_{xy}d^2_{xz}d^1_{yz}d^1_{z^2}d^0_{x^2-y^2}\right)$	3
	3216	$Fe\left(d^1_{xy}d^1_{xz}d^1_{yz}d^2_{z^2}d^1_{x^2-y^2}\right)$	5	3242	$Fe\left(d^1_{xy}d^1_{xz}d^1_{yz}d^2_{z^2}d^1_{x^2-y^2}\right)$	5
	3955	$Fe\left(d^1_{xy}d^1_{xz}d^2_{yz}d^1_{z^2}d^1_{x^2-y^2}\right)$	5	4043	$Fe\left(d^1_{xy}d^1_{xz}d^2_{yz}d^1_{z^2}d^1_{x^2-y^2}\right)$	5
	4035	$Fe\left(d^1_{xy}d^2_{xz}d^1_{yz}d^1_{z^2}d^1_{x^2-y^2}\right)$	5	4081	$Fe\left(d^1_{xy}d^2_{xz}d^1_{yz}d^1_{z^2}d^1_{x^2-y^2}\right)$	5
FePc-Pyrene-B	—	$Fe(d^2_{xy}d^1_{xz}d^2_{yz}d^1_{z^2}d^0_{x^2-y^2})\ B\left(p^1_z\right)$	2	—	$Fe(d^2_{xy}d^1_{xz}d^1_{yz}d^2_{z^2}d^0_{x^2-y^2}\ B\left(p^1_z\right))$	2
	126	$Fe(d^2_{xy}d^1_{xz}d^1_{yz}d^2_{z^2}d^0_{x^2-y^2})\ B\left(p^1_z\right)$	4	26	$Fe(d^2_{xy}d^1_{xz}d^1_{yz}d^2_{z^2}d^0_{x^2-y^2})\ B\left(p^1_z\right)$	4
	724	$Fe(d^2_{xy}d^2_{xz}d^1_{yz}d^1_{z^2}d^0_{x^2-y^2})\ B\left(p^1_z\right)$	2	148	$Fe(d^2_{xy}d^1_{xz}d^2_{yz}d^1_{z^2}d^0_{x^2-y^2})\ B\left(p^1_z\right)$	2
	908	$Fe(d^2_{xy}d^1_{xz}d^1_{yz}d^2_{z^2}d^0_{x^2-y^2})\ B\left(p^1_z\right)$	2	164	$Fe(d^2_{xy}d^1_{xz}d^2_{yz}d^1_{z^2}d^0_{x^2-y^2})\ B\left(p^1_z\right)$	4
	1245	$Fe(d^2_{xy}d^1_{xz}d^2_{yz}d^1_{z^2}d^0_{x^2-y^2})\ B\left(p^1_z\right)$	4	252	$Fe(d^2_{xy}d^2_{xz}d^1_{yz}d^1_{z^2}d^0_{x^2-y^2})\ B\left(p^1_z\right)$	4
	1776	$Fe(d^2_{xy}d^2_{xz}d^1_{yz}d^1_{z^2}d^0_{x^2-y^2})\ B\left(p^1_z\right)$	4	280	$Fe(d^2_{xy}d^2_{xz}d^1_{yz}d^1_{z^2}d^0_{x^2-y^2})\ B\left(p^1_z\right)$	2
FePc-Pyrene-N	—	$Fe\left(d^2_{xy}d^1_{xz}d^1_{yz}d^2_{z^2}d^0_{x^2-y^2}\right)\ N\left(p^1_z\right)$	2	—	$Fe\left(d^2_{xy}d^1_{xz}d^2_{yz}d^1_{z^2}d^0_{x^2-y^2}\right)\ N\left(p^1_z\right)$	2
	25	$Fe\left(d^2_{xy}d^1_{xz}d^1_{yz}d^2_{z^2}d^0_{x^2-y^2}\right)\ N\left(p^1_z\right)$	4	329	$Fe\left(d^2_{xy}d^1_{xz}d^1_{yz}d^2_{z^2}d^0_{x^2-y^2}\right)\ N\left(p^1_z\right)$	2
	154	$Fe\left(d^2_{xy}d^2_{xz}d^1_{yz}d^1_{z^2}d^0_{x^2-y^2}\right)\ N\left(p^1_z\right)$	2	429	$Fe\left(d^2_{xy}d^1_{xz}d^2_{yz}d^1_{z^2}d^0_{x^2-y^2}\right)\ N\left(p^1_z\right)$	4
	421	$Fe\left(d^2_{xy}d^2_{xz}d^1_{yz}d^1_{z^2}d^0_{x^2-y^2}\right)\ N\left(p^1_z\right)$	4	472	$Fe\left(d^2_{xy}d^1_{xz}d^1_{yz}d^2_{z^2}d^0_{x^2-y^2}\right)\ N\left(p^1_z\right)$	4
	465	$Fe\left(d^2_{xy}d^1_{xz}d^2_{yz}d^1_{z^2}d^0_{x^2-y^2}\right)\ N\left(p^1_z\right)$	2	1238	$Fe\left(d^2_{xy}d^2_{xz}d^1_{yz}d^1_{z^2}d^0_{x^2-y^2}\right)\ N\left(p^1_z\right)$	2
	508	$Fe\left(d^2_{xy}d^1_{xz}d^2_{yz}d^1_{z^2}d^0_{x^2-y^2}\right)\ N\left(p^1_z\right)$	4	1335	$Fe\left(d^2_{xy}d^2_{xz}d^1_{yz}d^1_{z^2}d^0_{x^2-y^2}\right)\ N\left(p^1_z\right)$	4
FePc-Pyrene-S	—	$Fe\left(d^2_{xy}d^2_{xz}d^2_{yz}d^0_{z^2}d^0_{x^2-y^2}\right)$	1	—	$Fe\left(d^2_{xy}d^2_{xz}d^2_{yz}d^0_{z^2}d^0_{x^2-y^2}\right)$	1
	6514	$Fe\left(d^2_{xy}d^1_{xz}d^2_{yz}d^1_{z^2}d^0_{x^2-y^2}\right)$	3	2520	$Fe\left(d^2_{xy}d^1_{xz}d^2_{yz}d^1_{z^2}d^0_{x^2-y^2}\right)$	3
	6542	$Fe\left(d^2_{xy}d^2_{xz}d^1_{yz}d^1_{z^2}d^0_{x^2-y^2}\right)$	3	2615	$Fe\left(d^2_{xy}d^2_{xz}d^1_{yz}d^1_{z^2}d^0_{x^2-y^2}\right)$	3
	8885	$Fe\left(d^1_{xy}d^2_{xz}d^2_{yz}d^1_{z^2}d^0_{x^2-y^2}\right)$	3	4833	$Fe\left(d^1_{xy}d^2_{xz}d^2_{yz}d^1_{z^2}d^0_{x^2-y^2}\right)$	3
	10055	$Fe\left(d^1_{xy}d^1_{xz}d^2_{yz}d^1_{z^2}d^1_{x^2-y^2}\right)$	5	5972	$Fe\left(d^1_{xy}d^1_{xz}d^2_{yz}d^1_{z^2}d^1_{x^2-y^2}\right)$	5
	10109	$Fe\left(d^1_{xy}d^2_{xz}d^1_{yz}d^1_{z^2}d^1_{x^2-y^2}\right)$	5	6035	$Fe\left(d^1_{xy}d^2_{xz}d^1_{yz}d^1_{z^2}d^1_{x^2-y^2}\right)$	5

TABLE 6.3: NEVPT2 transition energies ν (in cm^{-1}), d-shell configurations, and state multiplicities 2S+1 for the ground and excited states of the studied FePc/Pyrene hybrid systems without the SW defect (left panel) and with the SW defect (right panel). All presented results were obtained employing CAS(10,9) for for FePc/Pyrene(-S) and CAS(11,9) for FePc/Pyrene-B(-N), where iron d-orbitals and closet HOMO and LUMO ligand state are in the active space.

	CAS(6,5)		CAS(10,9)	
System	D, cm^{-1}	E/D	D, cm^{-1}	E/D
FePc	90.0	0	91.6	0.06
FePc/Pyrene	85.1	0.1	87.8	0.13
FePc/Pyrene-SW	86.2	0.14	89.9	0.09

TABLE 6.4: FePc, FePc/Pyrene, and FePc/Pyrene-SW zero-field splitting parameters.

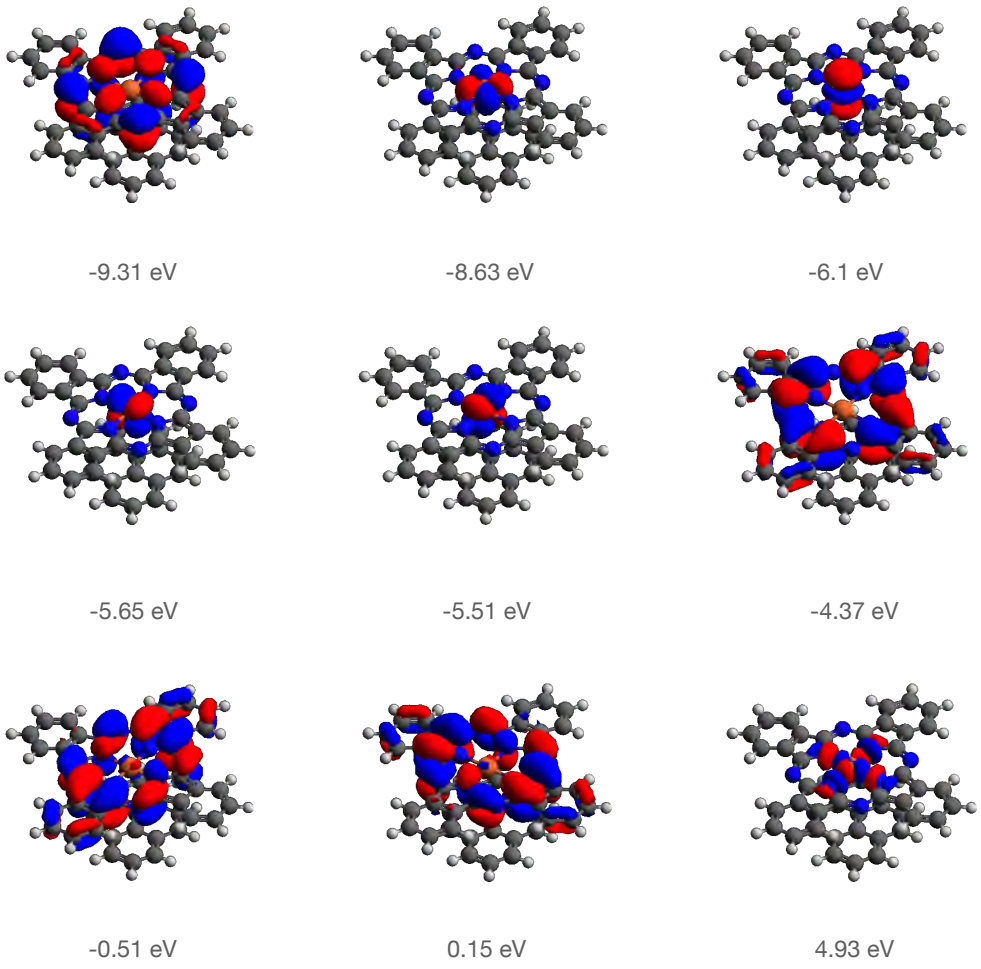

FIGURE 6.5: FePc/Pyrene active molecular orbitals in CAS(10,9) and their energies. Red and blue colours mean positive and negative charged densities, respectively.

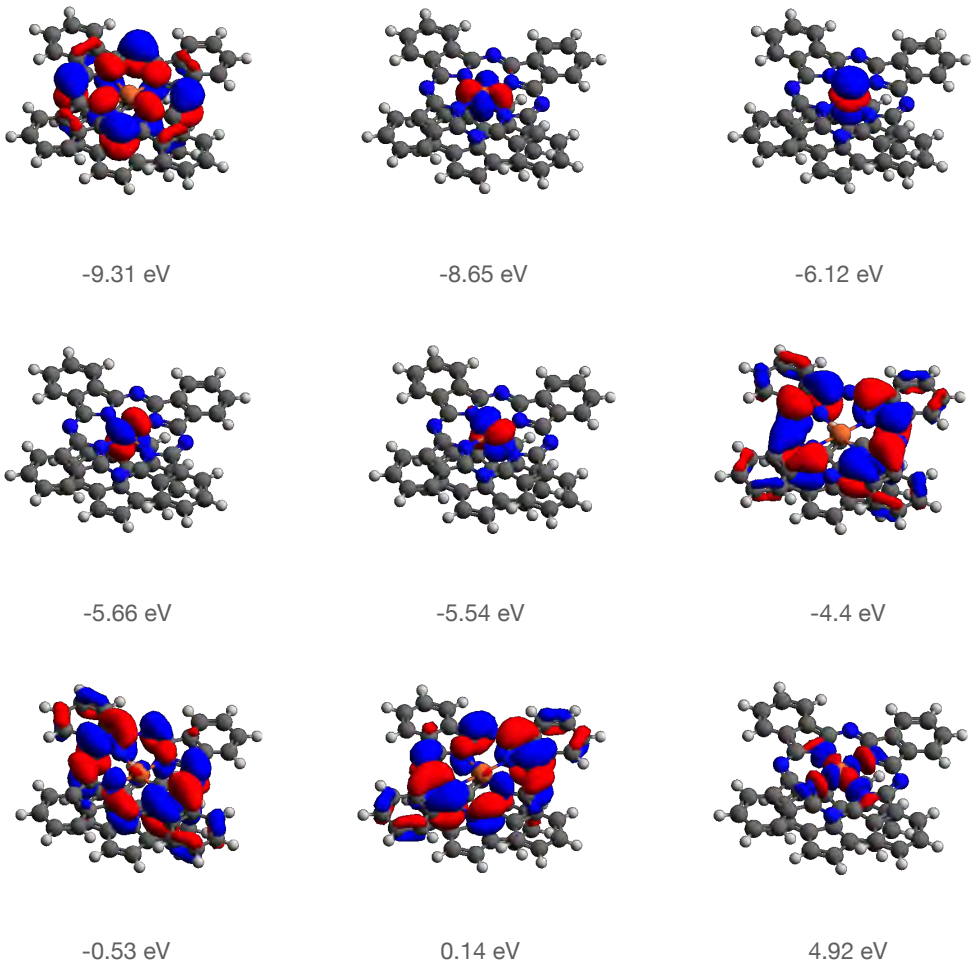

FIGURE 6.6: FePc/Pyrene-SW active molecular orbitals in CAS(10,9) and their energies. Red and blue colours mean positive and negative charged densities, respectively.

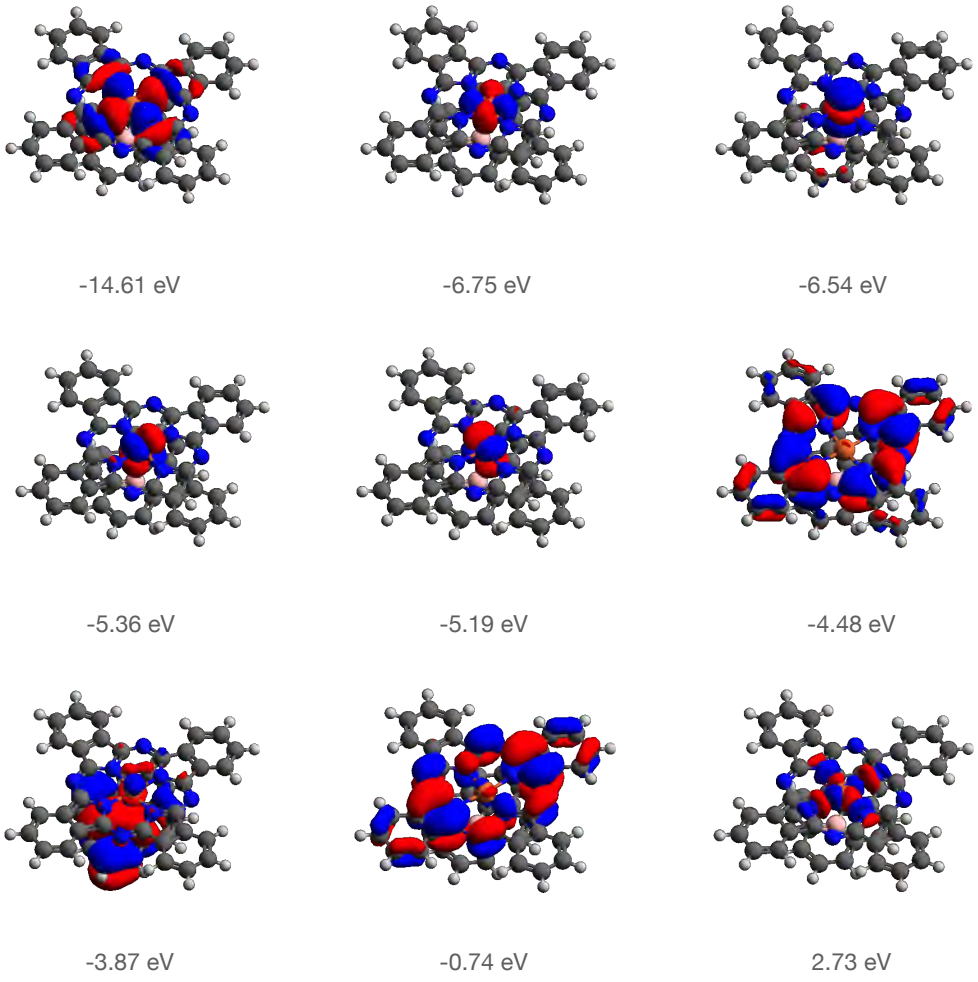

FIGURE 6.7: FePc/Pyrene-B active molecular orbitals in CAS(11,9) and their energies. Red and blue colours mean positive and negative charged densities, respectively.

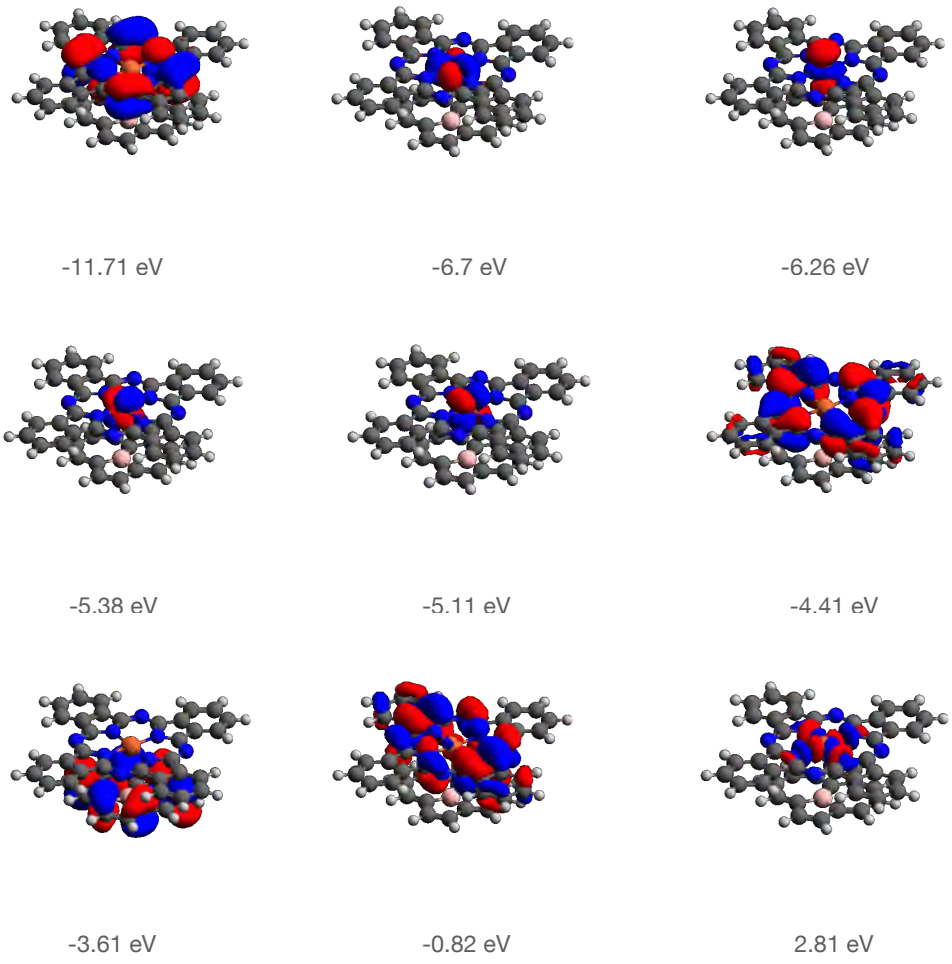

FIGURE 6.8: FePc/Pyrene-SW-B active molecular orbitals in CAS(11,9) and their energies. Red and blue colours mean positive and negative charged densities, respectively.

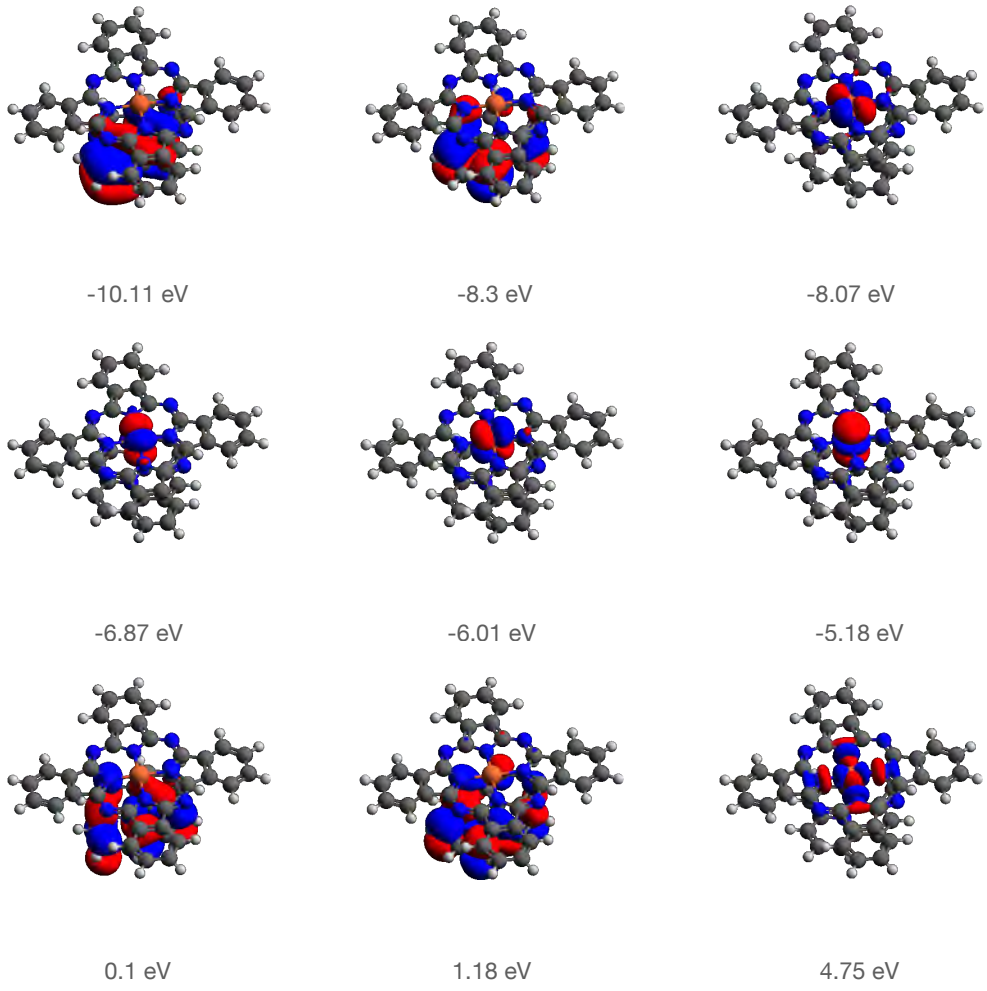

FIGURE 6.9: FePc/Pyrene-N active molecular orbitals in CAS(11,9) and their energies. Red and blue colours mean positive and negative charged densities, respectively.

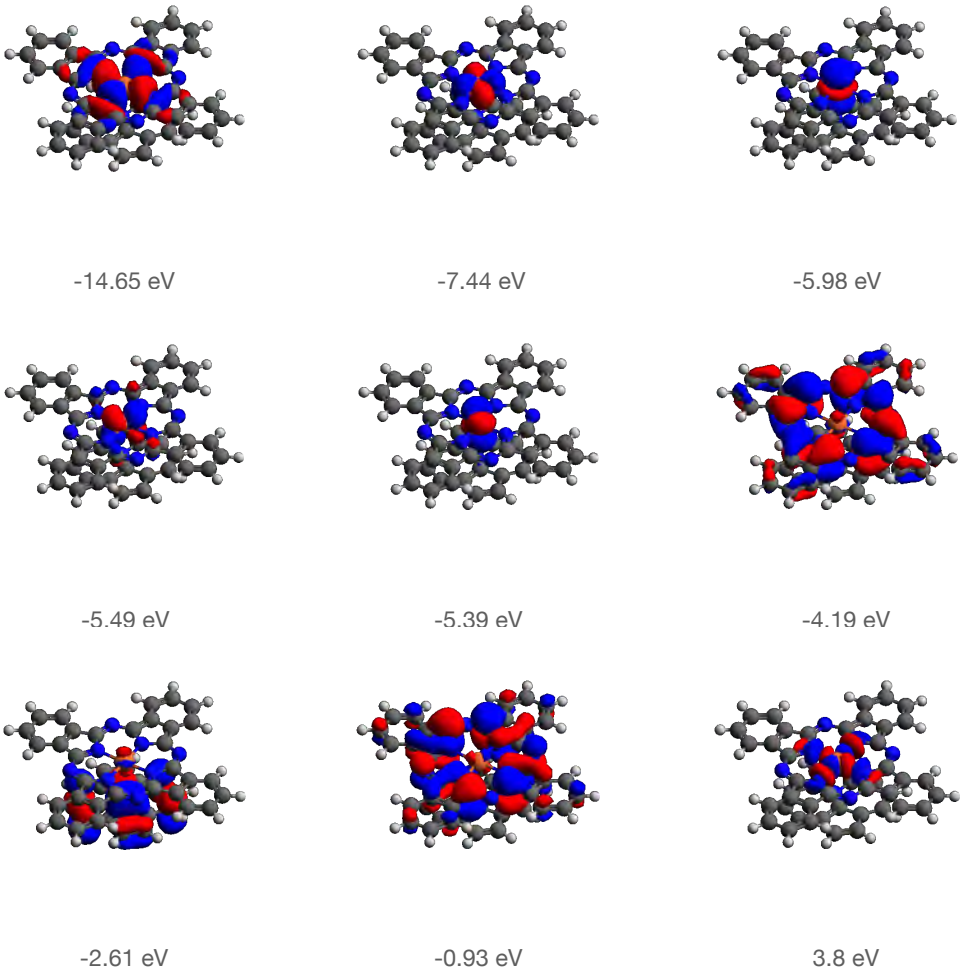

FIGURE 6.10: FePc/Pyrene-SW-N active molecular orbitals in CAS(11,9) and their energies. Red and blue colours mean positive and negative charged densities, respectively.

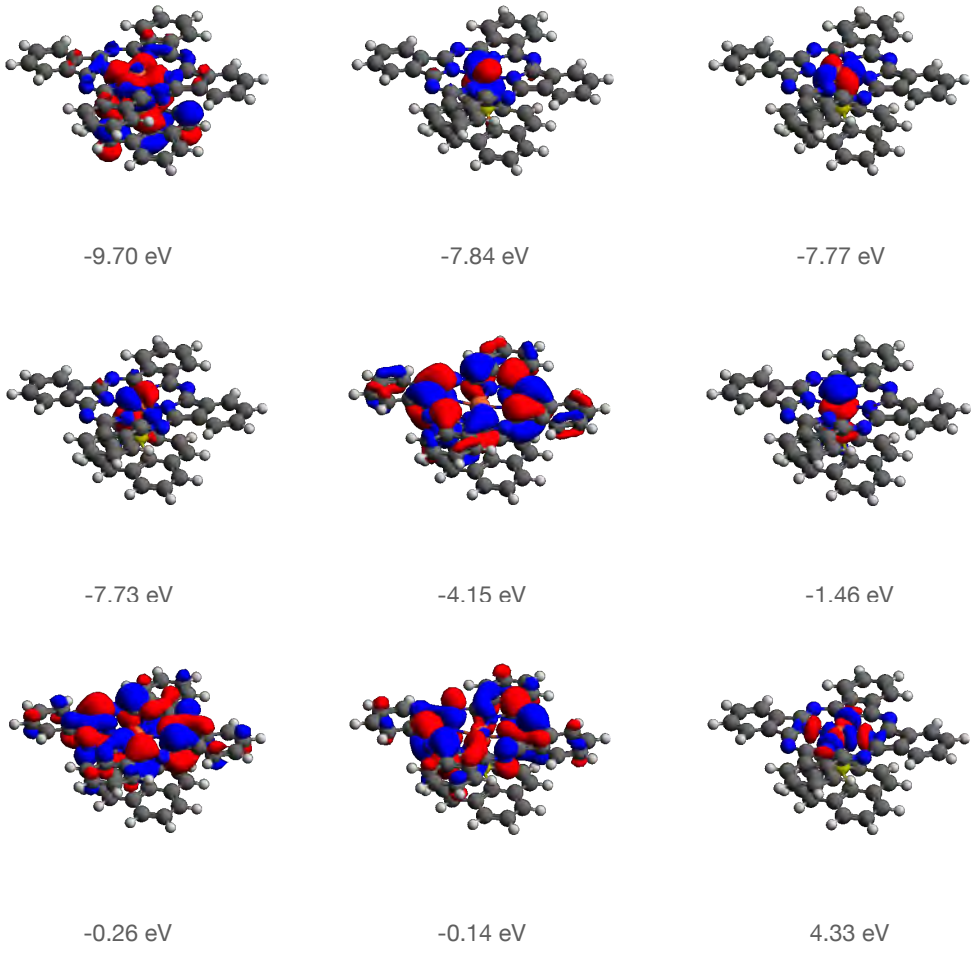

FIGURE 6.11: FePc/Pyrene-S active molecular orbitals in CAS(10,9) and their energies. Red and blue colours mean positive and negative charged densities, respectively.

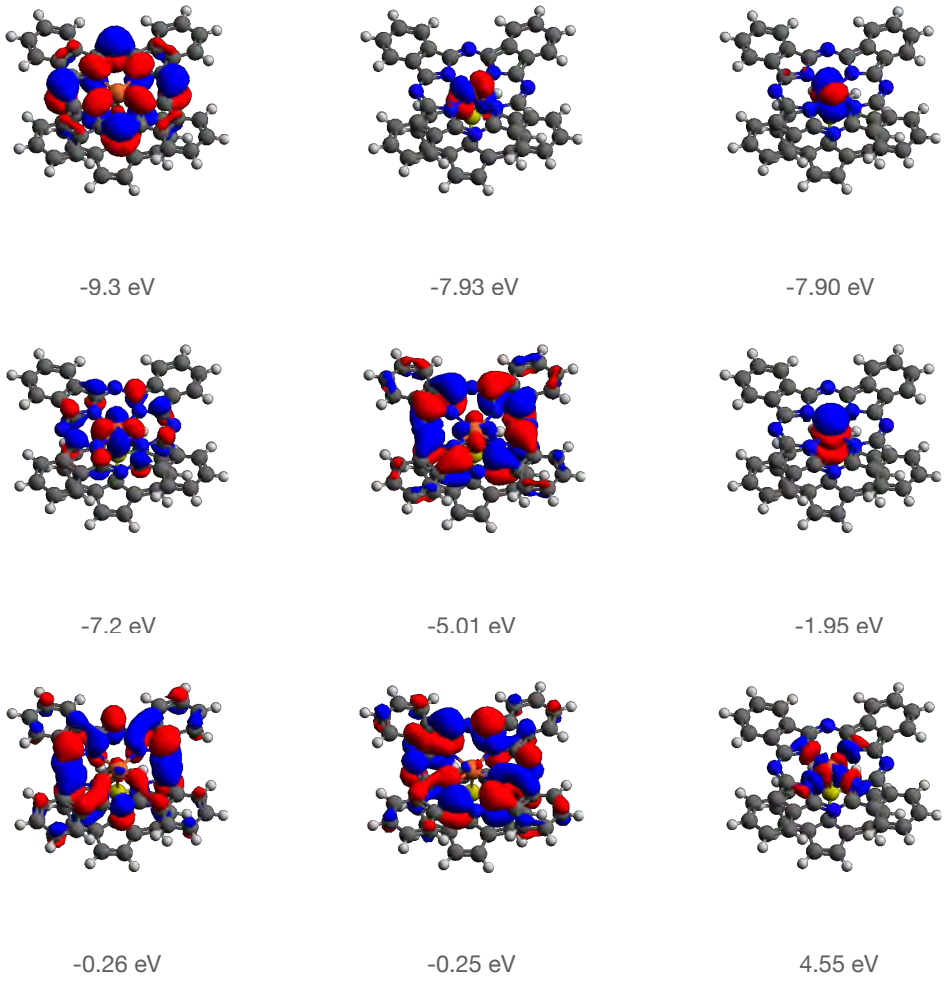

FIGURE 6.12: FePc/Pyrene-SW-S active molecular orbitals in CAS(10,9) and their energies. Red and blue colours mean positive and negative charged densities, respectively.

Chapter 7

Fe(Pc)/Ti_2C: DFT Analysis

In this chapter, we describe the results obtained for the hybrid system consisting of the FePc molecule adhered to the MXenes Ti_2C trilayer. Since Ti external layers are magnetic, here one can expect intriguing physics related to the magnetic interactions of Fe atom from phthalocyanine with Ti atoms from the substrate.

7.1 Geometric and Energy Characteristics

We start the discussion of this hybrid system by presenting the characterisation of its geometry and energetics as obtained in DFT supercell calculations.

The most energetically favourable position of the FePc molecule on the Ti_2C layer was initially found without taking into account the spin polarisation. To accelerate the finding of the optimised geometry of the hybrid system FePc/Ti_2C, we have performed the following procedures. We began with constructing a one-dimensional potential energy surface to search for a preliminary distance between the molecule and the surface. The molecule was positioned flat relative to the MXene layer. Based on these preliminary calculations, further optimisations were carried out at a height of 2.19 Å. After that, the positions of the molecule relative to the Ti_2C layer were selected (Fig. 7.1), in which the iron atom is located above the upper titanium atom (Up-Ti-Centre), above the carbon atom (C-Centre), and between the upper titanium atoms (Bridge). The position at which the iron atom is located above the lower titanium atom (Down-Ti-Centre) was excluded from consideration, since further optimisation during this case led to the Bridge-type geometry. In the selected positions, a one-dimensional potential energy surface was constructed with the coordinates of the molecule rotation around its axis. After finding the angle with the minimum energy of the system, finally, the geometry of the system was fully optimised by the computer code.

The performed procedure indicates that the Bridge position is the most energetically preferable, with the total energy being 0.13 eV lower than in the Up-Ti-Centre case, and 0.46 eV lower than the total energy of the hybrid system with the C-Center position of FePc. All further calculations were performed only for FePc in the Bridge position.

After optimisation (Fig. 7.2), the benzene rings of the FePc molecule are slightly bent from the MXnene surface, while the iron atom is located slightly below the average level of the molecule. The average distance between FePc and Ti_2C is 2.09 Å, while the Fe-Ti_2C distance is 2.03 Å. The adsorption energy of the molecule on a surface is about 20 eV, which is several times higher than the adsorption of FePc on other two-dimensional surfaces. This value, as well as the small distance between the molecule and the surface, may indicate that the interaction is no longer determined solely by the van der Waals interaction.

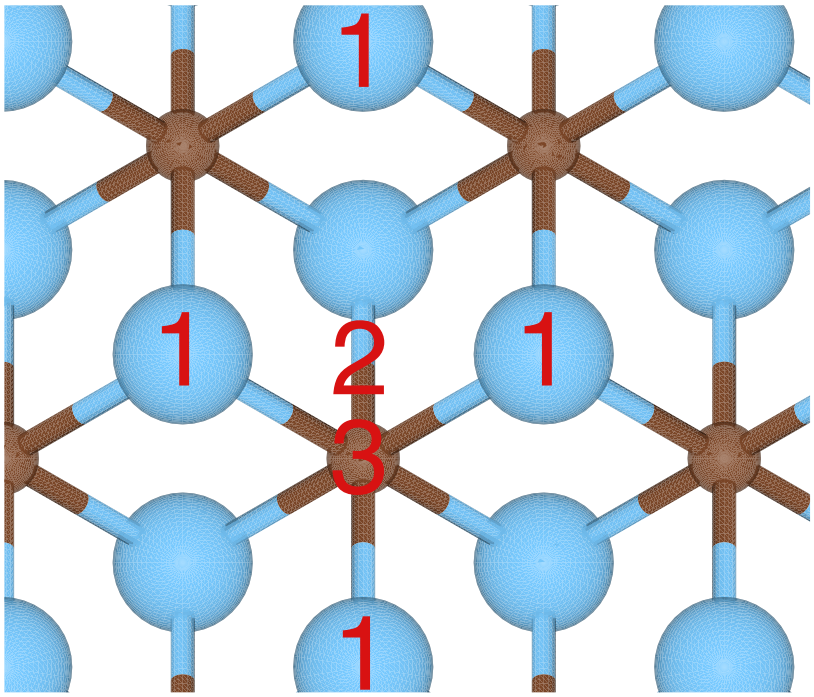

FIGURE 7.1: Considered points of the FePc adhesion to Ti_2C. Blue spheres indicate Ti atoms, brown spheres C atoms. The position of the iron atom is marked with a number: 1) Up-Ti-Centre, 2) Bridge, 3) C-Centre. The figure shows the Ti_2C layer in the projection on the xy-plane.

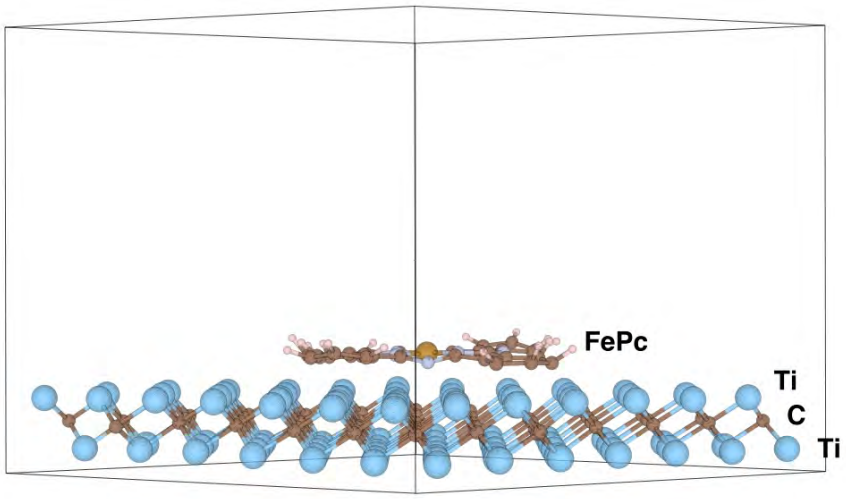

FIGURE 7.2: Side view of the FePc/Ti_2C hybrid system in the supercell used in the DFT calculations. The vacuum layer in the supercell is in proportion to the lateral dimensions of the supercell.

We consider also FePc/Ti_2C hybrid system with FePc molecule in its excited state and observe changes in the geometry of the system in comparison to the case when FePc is in its ground state. With the lengthening of the Fe-N bonds, the iron atom noticeably moved out of the plane of the molecule. The average distance between the FePc molecule and the top layer of Ti_2C is 2.08 Å, while the distance from the iron atom to Ti_2C is 2.36 Å, which is 0.33 Å longer than in the case of the ground state

molecule. This differs from the case of the free molecule, where the bond lengths are lengthened in the plane of the molecule.

7.2 Possible Orientations of Local Spin Polarisations

Taking into account the spin polarisation of this system leads to several possible magnetic configurations. The Ti_2C surface can be both ferromagnetic and antiferromagnetic, and the FePc molecule can have different directions of its magnetic moment vector relative to Ti_2C. In total, there are four different magnetic configurations for the FePc/Ti_2C hybrid system (Fig. 7.3). By initialising the initial magnetic moment in certain ways, the results of calculating the energy parameters showed that the cases with an antiferromagnetic orientation of the titanium layers are energetically more favourable. For the free standing Ti_2C, the energy difference between the ferromagnetic and antiferromagnetic states is 1.67 eV (for the considered size of the cell). The energies of FePc/Ti_2C systems with the ferromagnetic orientation of titanium layers turned out to be 0.8 eV higher. The exchange energy $E_e x = E_{Fe_{Up}} - E_{Fe_{Down}}$, the energy difference between the cases with the same initial Ti_2C magnetisation and different orientation of the iron atom in the FePc molecule, is 283 meV for the ferromagnetic case, 9 meV for the antiferromagnetic case, and 0.6 meV for the antiferromagnetic case with the molecule in the excited state.

The magnetic characteristics of the studied systems with the non-excited FePc molecule are shown in Table 7.1. In the calculations, a feature of the magnetisation of these systems is distinguished. The magnetic moment of a single FePc molecule is 2 μ_B. When the magnetic moment of a single molecule is reoriented, its value changes by $|4\mu_B|$ from -2μ_B to 2μ_B or vice versa. However, the table shows that the difference in total magnetisation between the cases of FUp (AFUp) and FDown (AFDown) is only $|2\mu_B|$. In this case, the spin density of the FePc molecule is concentrated on the iron atom, and the magnitude of the polarisation of the iron atom does not fundamentally change.

Studying the spin polarisation of atoms (Table 7.2) helps to understand the distribution of the magnetic moment in the systems. Atomic spin polarisations were calculated as the difference in the spin density on the atomic orbitals projections. There are cases in which the magnetic moments of the atoms of the upper titanium layer MXene and the iron atom in FePc are initially co-directed (cases FUp and AFDown). In these cases, the titanium atoms closest to the iron atom have practically no magnetic moment. It indicates that a ferromagnetic interaction between the top Ti_2C layer and the FePc iron atom takes place. The difference in polarisation of titanium atoms adjacent to the iron atom between the cases FUp (AFUp) and FDown (AFDown) nearly compensates for the difference between the sum of atomic polarisation of the entire layer in the same cases.

	Total Magnetisation, μ_B/cell	Absolute Magnetisation, μ_B/cell
FUp	67.63	72.92
FDown	65.42	72.65
AFUp	23.56	81.57
AFDown	21.56	81.29

TABLE 7.1: Magnetic characteristics of the FePc/Ti_2C hybrid system with various polarisation configurations (FUp, FDown, AFUp, and AFDown) as described in the main text and Fig. 7.3.

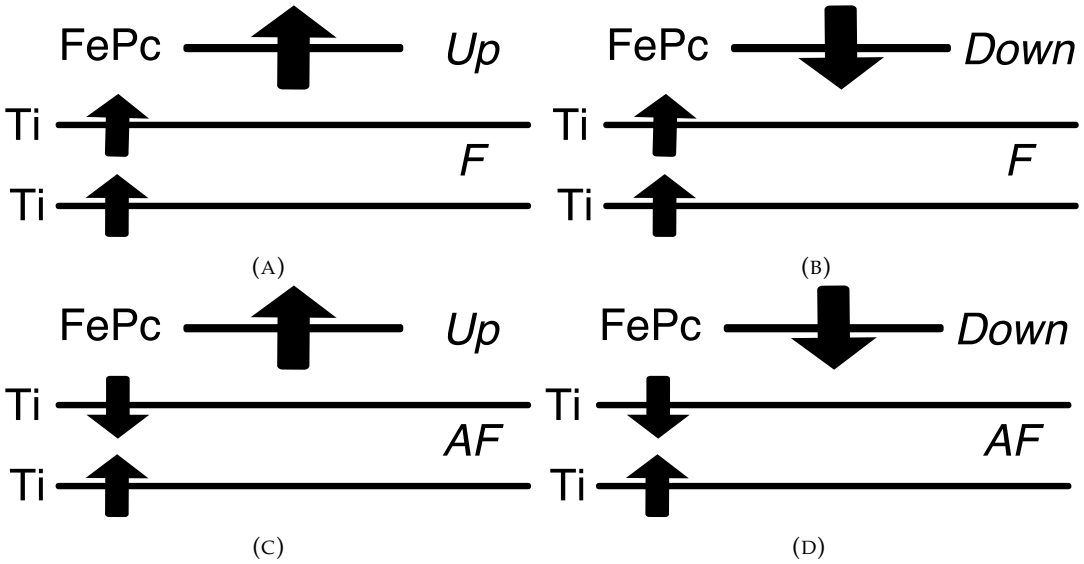

FIGURE 7.3: Schematic side view of the possible spin polarisation orientations in FePc molecule and Ti layers indicated as: A) FUp, B) FDown, C)AFUp, D)AFDown.

	Sum of Polarisations, a.u.	Sum of MXene Atomic Polarisations, a.u.	FePc Polarisation, a.u.	Fe Polarisation, a.u.	1st Ti Neighbours Polarisaiton, a.u.	2nd Ti Neighbours Polarisaiton, a.u.
FUp	61.36	59.96	1.4	1.24	-0.07	0.17
FDown	59.04	60.25	-1.21	-1.33	-0.29	0.64
AFUp	22.21	20.91	1.31	1.29	-0.47	-1.82
AFDown	20.36	21.52	-1.16	-1.33	-0.04	-1.16

TABLE 7.2: The spin polarisations in the FePc/Ti_2C hybrid system. The "1st Neighbours Polarisation" column shows the sum polarisation of 4 titanium atoms which are the nearest to the FePc iron atom. The "2st Neighbours Polarisation" column shows the sum polarisation of 14 top layer titanium atoms which are the nearest to the FePc iron atom.

The magnetic characteristics of FePc/Ti_2C with the excited state molecule are presented Table 7.3. Only the cases with the antiferromagnetic polarisation Ti_2C were studied, since they have lower energy compared to the cases with the ferromagnetic polarisation. The unobvious difference in the complete magnetization of systems with opposite orientations of the spin moment of the Fe atom, which was observed in the case with the ground state molecule, persisted in the case of the excited state. The difference between the excited states (S = 2, $\mu = 4\ \mu_B$) of the free standing FePc molecule with antiparallel spin orientations is $|8\mu_B|$, while for FePc/Ti_2C with antiparallel FePc spin orientations it is $|7\mu_B|$.

	Total Magnetisation, μ_B/cell	Absolute Magnetisation, μ_B/cell
AFUpEx	25.34	82.96
AFDownEx	18.31	83.89

TABLE 7.3: Magnetic characteristics of the FePc/Ti_2C hybrid systems with various polarisation configurations when the FePc molecule is in the considered excited state.

The results of the spin density projection onto the atomic orbitals for FePc/Ti_2C hybrid systems when the FePc molecule is in the excited state are presented in Table

7.4. Here, the "1st Ti Neighbours" atoms adjacent to the iron atom have spin polarisation if the iron atom and the Ti upper layer magnetisations are co-directed. Previously, for the same system with FePc in the ground state (Table 7.2) it was shown that the "1st Ti Neighbours" spin polarisation is practically absent. The described difference between systems in ground and excited FePc states can be explained by the fact that in the system with excited FePc the iron atom is above the FePc plane and, as a consequence, the interaction between the iron atom and the upper Ti_2C layer decreases.

	Sum of Polarisations, a.u.	Sum of MXene Atomic Polarisations, a.u.	FePc Polarisation, a.u.	Fe Polarisation, a.u.	1st Ti Neighbours Polarisaiton, a.u.	2st Ti Neighbours Polarisaiton, a.u.
AFUpEx	24.27	21.17	3.1	2.93	-0.34	-1.67
AFDownEx	16.55	20.37	3.82	-3.61	-0.47	-1.83

TABLE 7.4: The spin polarisations of groups of atoms in the FePc/Ti_2C hybrid system when the FePc molecule is in the excited state. The “1st Neighbours Polarisation” column shows the sum polarisation of 4 titanium atoms which are the nearest to the FePc iron atom. The “2st Neighbours Polarisation” column shows the sum polarisation of 14 top layer titanium atoms which are the nearest to the FePc iron atom.

7.3 Density of States Analysis

Before we discuss the density of states in the FePc/Ti_2C hybrid systems, let us have a look at the d-level splitting and the PDOS of the free standing FePc depicted in Fig. 7.4 and the DOS of Ti_2C with ferromagnetic and antiferromagnetic orderings of Ti layers as depicted in Fig. 7.5

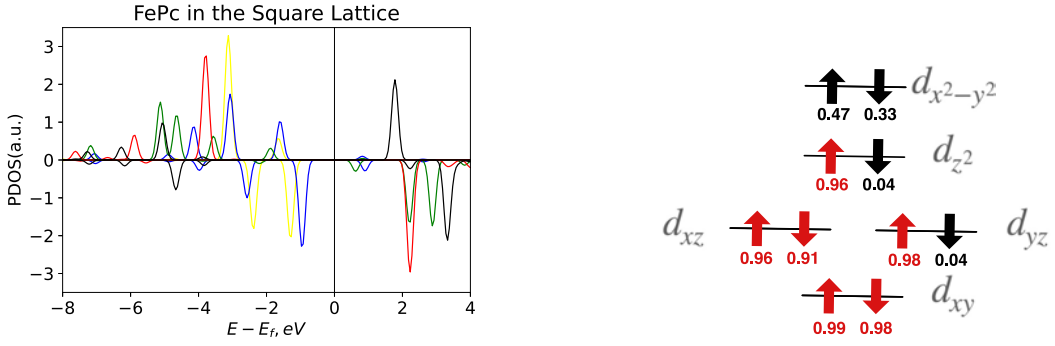

FIGURE 7.4: Analysis of the iron d-orbitals in FePc. (A) Spin resolved projected onto d-states density of states for FePc molecule indicated with different colours for five d-orbitals: yellow - d_{xy}, blue - d_{xz}, green - d_{yz}, red - d_{z^2}, black - $d_{x^2-y^2}$. (B) Scheme of energetically split d-orbitals in the crystal field of tetragonal symmetry. The Löwdin charges associated with each spin up and down d-orbital are given below the levels. The six orbitals with the highest charge (*i.e.*, occupation probability) are indicated in red colour.

In the DFT calculations for free standing FePc we employed square based supercell, which guarantees that the symmetry is really tetragonal. Since the symmetry of free standing FePc is tetragonal, and the symmetry of Ti_2C is trigonal, the symmetry of the hybrid system is very low, namely monoclinic. Therefore, the iron d_{xz} and

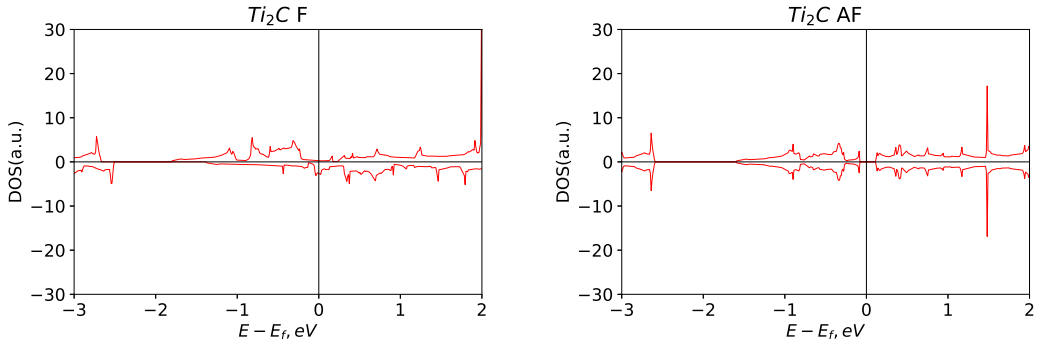

(A) (B)

FIGURE 7.5: Spin up & down densities of states for Ti_2C trilayer with (A) ferromagnetic, and (B) antiferromagnetic ordering of magnetic moments in the Ti sublayers. Note small band gap in Ti_2C with the antiferromagnetic ordering of Ti layers.

d_{yz} orbitals, which are energetically degenerated in the free standing FePc molecule, will split in the FePc/Ti_2C hybrid system.

In Fig. 7.4 it is clearly seen that the sum of both spin occupancies over the six most popular populated levels gives spin value S=1, whereas this value in the free Fe atom is S=2.

Concerning the electronic structure of Ti_2C, we point out that the structure with antiferromagnetic ordering of magnetic moments in Ti layers exhibits tiny band gap.

Now, we are in the position to perform an analysis of the DOS for all considered variants of the FePc/Ti_2C hybrid systems as defined and depicted in Fig. 7.3 and named FUp, FDown, AFUp, and AFDown. The results are presented in the series of figures: Fig. 7.6 for FUp and FDown hybrid systems; Fig. 7.7 for the AFUp and AFDown hybrid systems; Fig. 7.8 for the AFUp and AFDown hybrid systems with the FePc molecule in the excited state indicated as AFUpEx and AFDownEx.

At the first glance on Figs. 7.6, 7.7, and 7.8 one realises that all investigated FePc/Ti_2C hybrid structures are metallic in contrast to the Ti_2C with antiferromagnetic ordering of Ti layers that exhibits a small band gap.

At a closer look at projected densities of states for the studied hybrid systems (see Figs. 7.6, 7.7, and 7.8, panels (C) and (D)), one realises that the electronic energy levels originating from the iron *d*-orbitals are placed fairly close to the Fermi energy. The population analysis of the iron d-orbitals in the FUp, FDown, AFUp, and AFDown forms of the FePc/Ti_2C hybrid systems is schematically shown in Fig. 7.6E, 7.6F, 7.7E, 7.7F. The *d*-orbital populations of those systems with FePc in its ground state qualitatively coincide with the populations for the isolated FePc molecule (Fig. 7.4). For the molecule in the excited state (Fig. 7.8E, 7.8F), *i.e.*, for hybrid systems indicated as AFUpEx and AFDownEx, it can be seen that the upper orbital $d_{x^2-y^2}$ is populated by one electron. Also, in both ground and excited states, the d_{z^2} orbital is completely populated. The iron atom leaves the plane of the molecule, the ligand field changes, and the electronegative nitrogen atoms are no longer in the *xy*-plane. As a consequence, the d_{z^2} orbital becomes more energetically favourable.

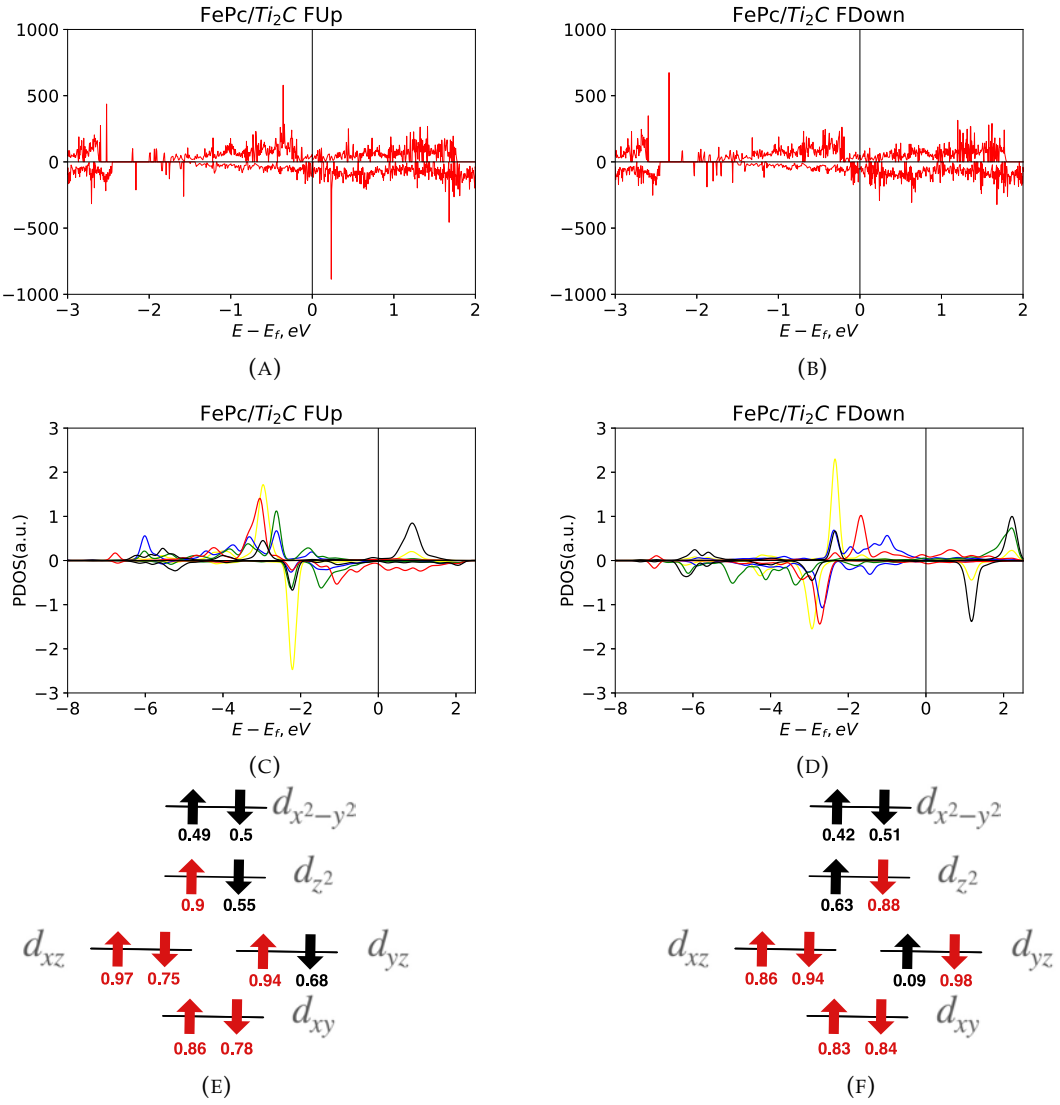

FIGURE 7.6: The electronic structure analysis of the FePc/Ti_2C systems *with the Ti_2C ferromagnetic configuration* FUp and FDown: total density of states for (A) iron spin up and (B) iron spin down cases, the iron d-orbital projected densities of states for (C) iron spin up and (D) iron spin down cases (yellow - d_{xy}, blue - d_{xz}, green - d_{yz}, red - d_{z^2}, black - $d_{x^2-y^2}$); Löwdin charges of each d-orbital component in the iron atom for (E) iron spin up and (F) iron spin down cases. The six orbitals with the highest occupation numbers are marked in red. For clarity of the PDOS pictures, the gaussian broadening parameter was taken to be equal to the energy grid step (0.005 eV).

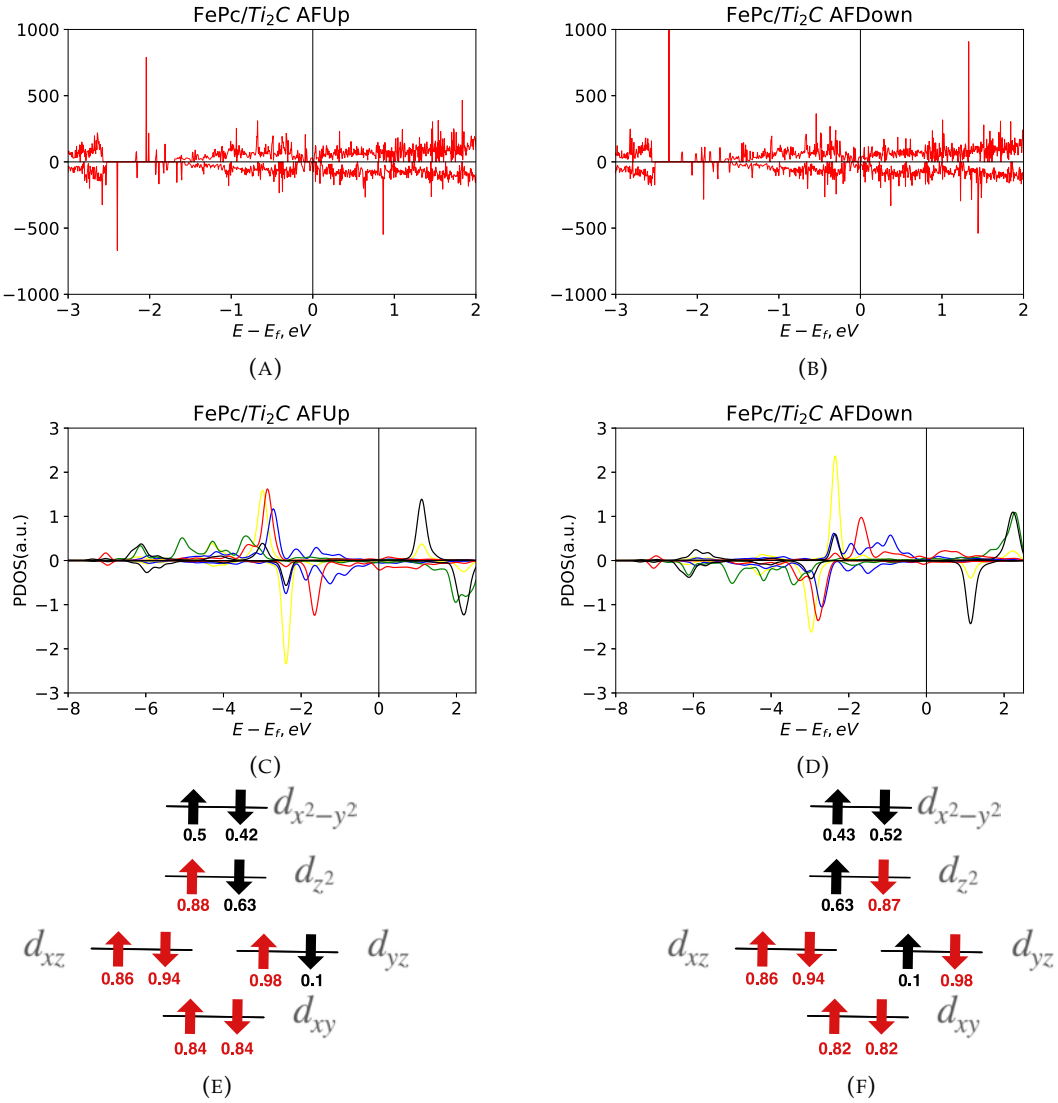

FIGURE 7.7: The electronic structure analysis of the FePc/Ti_2C systems *with the Ti_2C antiferromagnetic configuration* AFUp and AFDown: total density of states for (A) iron spin up and (B) iron spin down cases, the iron d-orbital projected densities of states for (C) iron spin up and (D) iron spin down cases (yellow - d_{xy}, blue - d_{xz}, green - d_{yz}, red - d_{z^2}, black - $d_{x^2-y^2}$); Löwdin charges of each d-orbital component in the iron atom for (E) iron spin up and (F) iron spin down cases. The six orbitals with the highest occupation numbers are marked in red. For clarity of the PDOS pictures, the gaussian broadening parameter was taken to be equal to the energy grid step (0.005 eV).

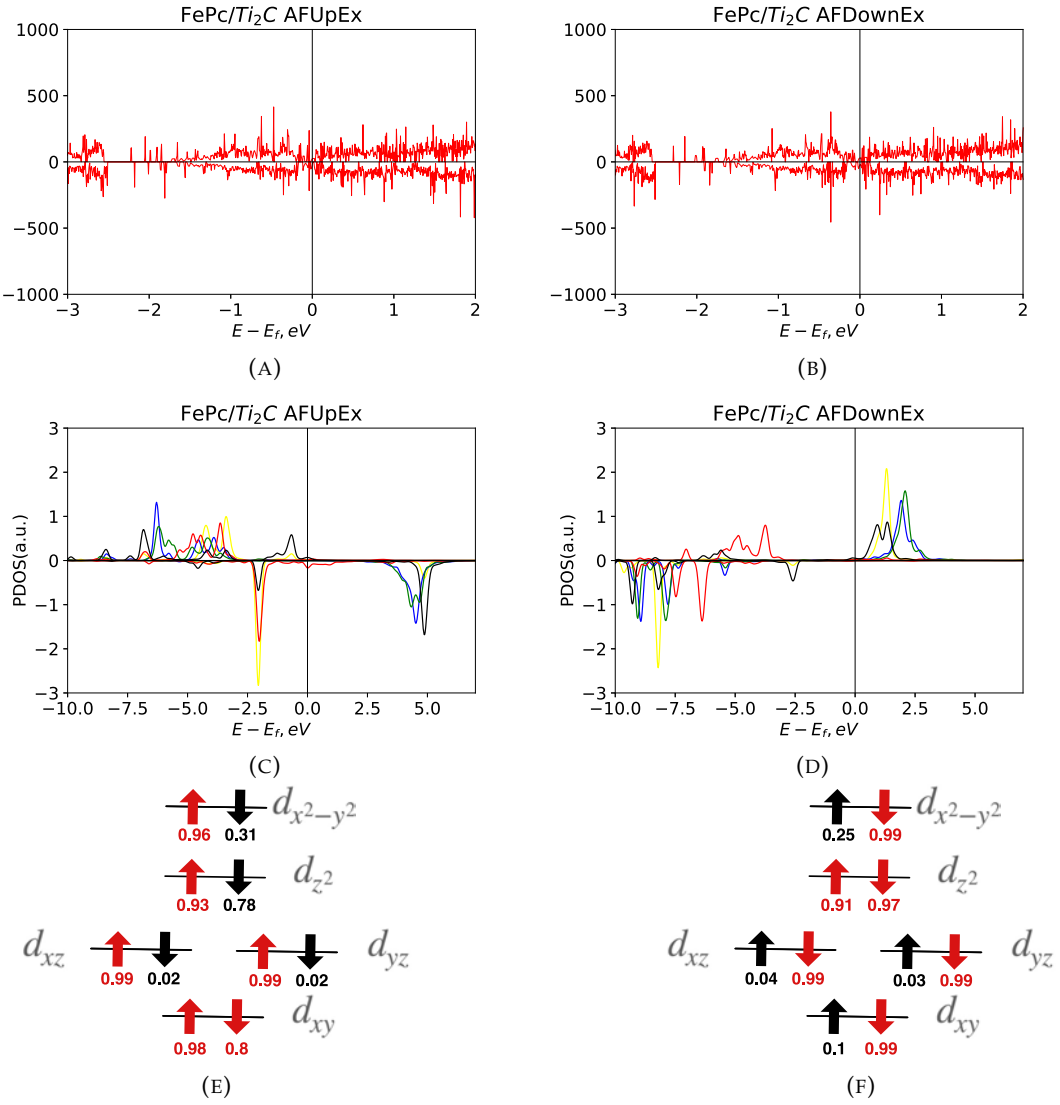

FIGURE 7.8: The electronic structure analysis of the FePc/Ti_2C systems *with the Ti_2C antiferromagnetic configuration and FePc in the excited state* AFUpEx and AFDownEx: total density of states for (A) iron spin up and (B) iron spin down cases, the iron d-orbital projected densities of states for (C) iron spin up and (D) iron spin down cases (yellow - d_{xy}, blue - d_{xz}, green - d_{yz}, red - d_{z^2}, black - $d_{x^2-y^2}$); Löwdin charges of each d-orbital component in the iron atom for (E) iron spin up and (F) iron spin down cases. The six orbitals with the highest occupation numbers are marked in red. For clarity of the PDOS pictures, the gaussian broadening parameter was taken to be equal to the energy grid step (0.005 eV).

7.4 Charge Transfer Analysis

The plots of the laterally averaged (*i.e.*, *xy*-integrated) charge density $\bar{\rho}_{charge}$ for FePc/Ti_2C are shown in Fig. 7.9. The total charge density integral over the unit cell was equal to the number of valence electrons in the cell. It is worth noting that the view of plots is practically identical for all considered types of hybrid systems, and the difference is not visible on the original scale. The charge densities of all systems near the Bader minimum are shown in the Fig. 7.9B. The 6-th order polynomial fitting was used to find the minimum for all configurations, and the charge transfer to the molecule is shown in Table 7.5.

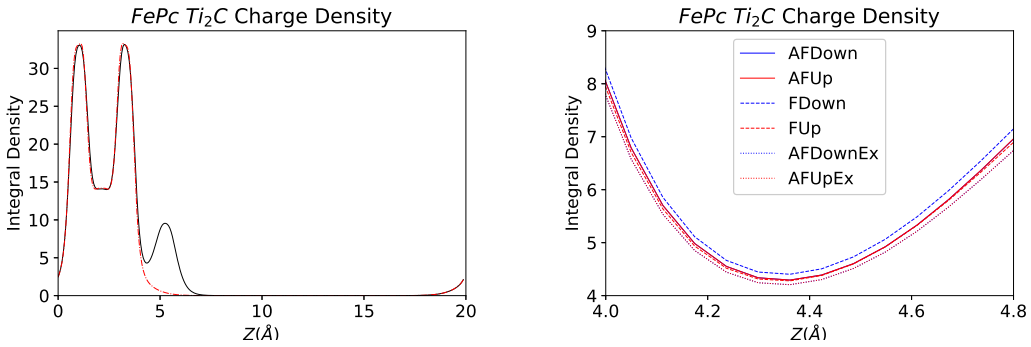

(A) (B)

FIGURE 7.9: The laterally averaged charge density of valence electrons (in units of $1/Å^3$) for the six types of the FePc/Ti_2C hybrid system: (A) black - the FePc/Ti_2C charge density, red dashed - the Ti_2C charge density; (B) close-up graph in the vicinity of minimum for all considered systems.

System	Charge transfer to FePc
AFDown	8.45
AFUp	8.45
FDown	8.4
FUp	8.77
AFDownEx	8.62
AFUpEx	8.74

TABLE 7.5: Charge transfer (in electrons) to the FePc molecule in the FePc/Ti_2C system with various magnetisation configurations.

To investigate the target of the charge transfer from Ti_2C to FePc the analysis of the projected density of states was done. This approach does not show the precise results of the charge transfer but can describe the Löwdin charge [120] difference for each atom in the FePc molecule. In Table 7.6, there are given mean and overall valence orbital charges for each type of atom in FePc. The results are shown for the free FePc molecule and for FePc in the FePc/Ti_2C hybrid system. The last column shows the mean charge transfer per atom (the difference between the atomic Löwdin charge in FePc/Ti_2C and FePc). This demonstrates that charge transfer occurs predominantly to carbon atoms.

The laterally averaged spin densities $\bar{\rho}_{spin}$ of the FePc/Ti_2C hybrid systems are shown in Figs. 7.10A and 7.10B, and compared to the laterally averaged spin densities for Ti_2C AF and F ordering of magnetisation in the Ti layers. The spin density

	Löwdin charge in pure FePc	Löwdin charge in FePc/Ti_2C	Charge transfer per atom
C	Mean = 3.971 (Sum = 127.084)	4.147 (132.713)	0.176
Fe	7.075	7.454	0.379
N	5.283 (42.266)	5.356 (42.849)	0.073
H	0.817 (13.068)	0.81 (12.962)	-0.006

TABLE 7.6: Löwdin charge for valence electrons in the free and adsorbed FePc molecule for each type of atom and the average charge transfer per atom for each type.

distributions in FePc/Ti_2C show a big decline in the upper-Ti layer. Also, two maximums in the vicinity of both titanium layers show the dominance of non-xy-plane d-orbitals (d_{xz}, d_{yz}, d_{z^2}) in the MXene formation.

The spin polarisation around FePc also splits into two maxima. In comparison, the spin density distribution for the free FePc molecule (fig. 7.10C) has a strong maximum in the centre of the molecule. This indicates that redistribution of spin polarisation occurs in the FePc molecule when it is attached to the MXene surface. Table 7.7 shows quantitative changes of iron d-orbital spin polarisation. This shows that the polarisation shifts from $d_{x^2-y^2}$ and d_{xy} orbitals to the non-plane orbitals.

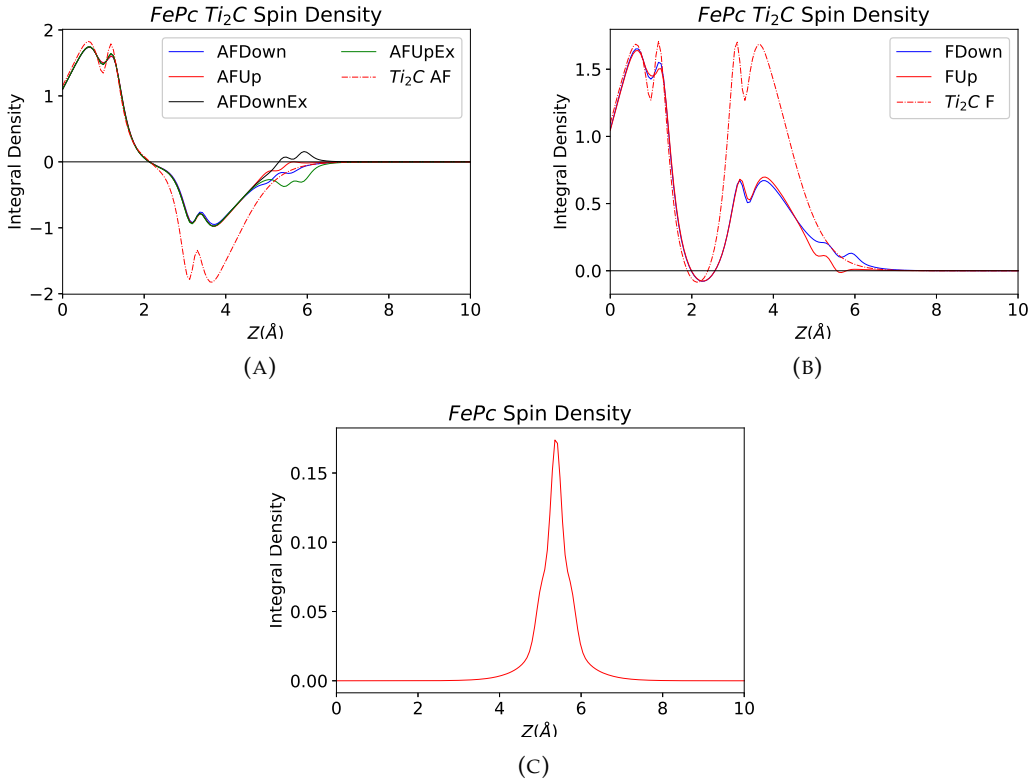

FIGURE 7.10: The laterally averaged spin density of valence electrons (in units of $1/Å^3$) for the FePc/Ti_2C hybrid systems in the (A) antiferromagnetic and (B) ferromagnetic Ti_2C configurations; (C) - the laterally averaged spin density of valence electrons (in units of $1/Å^3$) for the FePc molecule. The laterally averaged spin density for Ti_2C trilayer with AF and F ordering of magnetic moments in Ti layers is indicated, respectively, in panel (A) and (B) through red-dashed line.

	Fe in FePc	Fe in FePc/Ti_2C (AFDown)
d_{z^2}	0.94	-0.25
d_{xz}	0.06	-0.08
d_{yz}	0.05	-0.89
$d_{x^2-y^2}$	0.70	-0.09
d_{xy}	0.40	-0.01

TABLE 7.7: Spin polarisation of iron d-orbitals in the free-standing FePc and the FePc/Ti_2C hybrid system (AFDown case).

7.5 Fe/Ti_2C Analysis

Previously we described the magnetic interaction in the vicinity of the iron atom in the FePc/Ti_2C hybrid system. It was found that the iron's spin polarisation influences spin polarisations of neighbouring titanium atoms. A simpler model system with iron atom on the top of the Ti_2C surface (Fig. 7.11) can show this magnetic interaction clearer (without distortions induced by the FePc phthalocyanine ligand). The calculations were done only for the antiferromagnetic Ti_2C configuration where the iron spin moment is directed towards Ti_2C (FeUp, Fig. 7.12A) and in the opposite direction (FeDown, Fig. 7.12B).

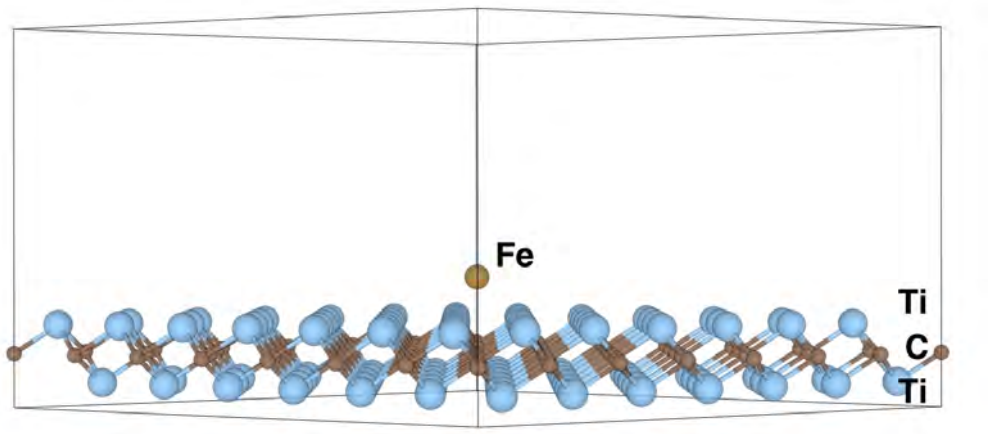

FIGURE 7.11: Side view of the Fe/Ti_2C system.

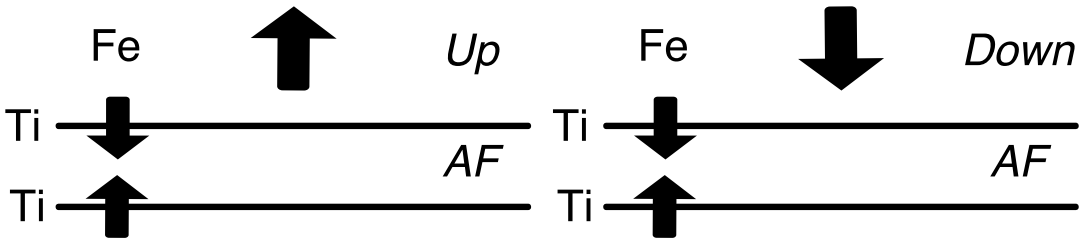

(A) (B)

FIGURE 7.12: Schematic side view of the magnetic moments ordering in the Fe/Ti_2C structures: (A) FeUp, (B) FeDown cases.

The computations for the Fe/Ti_2C system were done with the same 7x7 Ti_2C supercell, which was used in the studies of $FePc/Ti_2C$ systems. After preliminary optimisation, it was found that the configuration in which the iron atom is located above the middle of the triangle with titanium atoms of the upper layer at the vertices has the lowest energy. With this initial position, the optimisation of the iron atom on the antiferromagnetic Ti_2C layer was performed. The results of calculations for two cases in which the spin moment of the iron atom is directed towards and away from Ti_2C are presented in Table 7.8. Based on the data obtained, the upward orientation of the iron atom spin is more stable, although the distance of the atom to the layer increases. With this orientation, the iron atom practically does not influence the polarisation of the Ti_2C atoms. In the case of the downward orientation, the polarisation of titanium atoms - the nearest neighbours of the iron atom - is practically zero. This case is similar to the situation with the considered FePc molecule on Ti_2C where the magnetic orientations of FePc and the upper Ti_2C layer coincide. But in the case of a single iron atom, its second-row neighbours already have spin polarisation comparable to the rest of the titanium atoms in Ti_2C. The graphic results of the Löwdin analysis are presented in Figs. 7.13A and 7.13B.

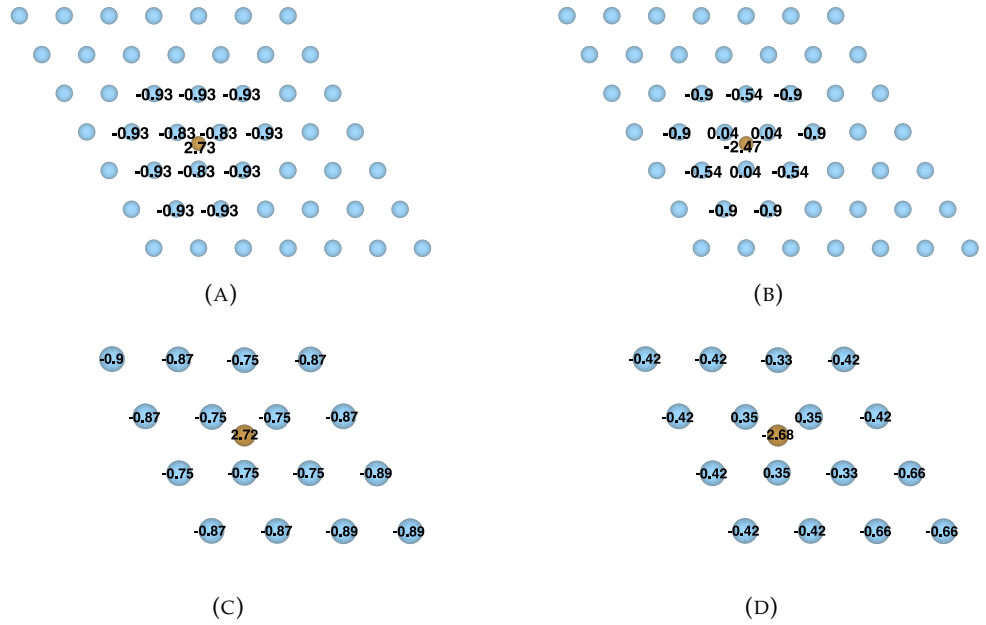

FIGURE 7.13: Spin polarisations of the iron atom and first layer Ti atoms in the Fe/Ti_2C system with the 7x7 Ti_2C supercell ((a) FeUp case, (b) FeDown case) and the 4x4 Ti_2C supercell ((c) FeUp case, (d) FeDown case).

		Adsorption Energy, eV	Fe height from Ti_2C, Å	μ(Fe)	mean $\mu(Ti_{bottom})$	$\mu(Ti_{Fe\ neigbours})$
7x7 Ti_2C supercell	FeUp	-4.02	1.83	2.73	0.95	-0.82
	FeDown	-3.59	1.77	-2.47	0.94	0.03
4x4 Ti_2C supercell	FeUp	-5.87	1.79	2.72	0.93	-0.75
	FeDown	-5.74	1.76	-2.67	0.76	0.35
Primitive Ti_2C cell	FeUp	-2.14	2.07	3.01	1.32	-0.59
	FeDown	-2.09	2.08	-2.96	0.76	0.42

TABLE 7.8: Geometric, electronic and magnetic characteristics of Fe/Ti_2C system in different cells.

The calculations with higher concentrations of iron atoms on the Ti_2C surface were done to compare the energetic and magnetic characteristics. In the cases where

4x4 Ti_2C supercell is used, the adsorption energy is about one and a half times higher but the atom-layer distance is similar to the 7x7 supercell case. A remarkable fact is that the magnetic moment of three titanium atoms, that are the neighbours of the iron atom, does not decay as in the 7x7 supercell case but changes its sign to the opposite. Also, the decrease of the bottom Ti layer spin density is observed in the FeDown case. Spin polarisations of the iron atom and top Ti_2C layer atoms are shown in Fig. 7.13C for the FeUp case and Fig. 7.13D for the FeDown case.

The Fe/Ti_2C complex with very high concentration of iron atoms, where an iron atom is on the top of each atom was also considered. In principle, here iron atoms are so close to each other that they form the additional Fe sublayer above MXene. The adsorption energy of the atom to the layer is two times lower and the atom-layer distance is 0.3 Å longer. In the FeDown case, the upper titanium layer magnetisation was flipped from down to up what changed the Ti_2C configuration from antiferromagnetic to ferromagnetic.

The electron density analysis of the Fe/Ti_2C system was done using the same techniques as in the case of FePc/Ti_2C hybrid system. The analysis was done for the system with one iron atom in the 4x4 MXene supercell. The vertical distributions of charge and spin densities are depicted in Fig. 7.14. Despite the fact that the iron atom does not really change the charge density distribution (Fig. 7.14B), it does influence the spin density distribution (Fig. 7.14A). The spin density distribution illustrates well the influence of the iron atom on its titanium neighbours. The iron "up" spin polarisation has almost no effect on the MXene spin density, while the "down" polarisation interacts with the nearest titanium atoms and flips their polarisation. Therefore, the spin density around the upper layer in Ti_2C drops.

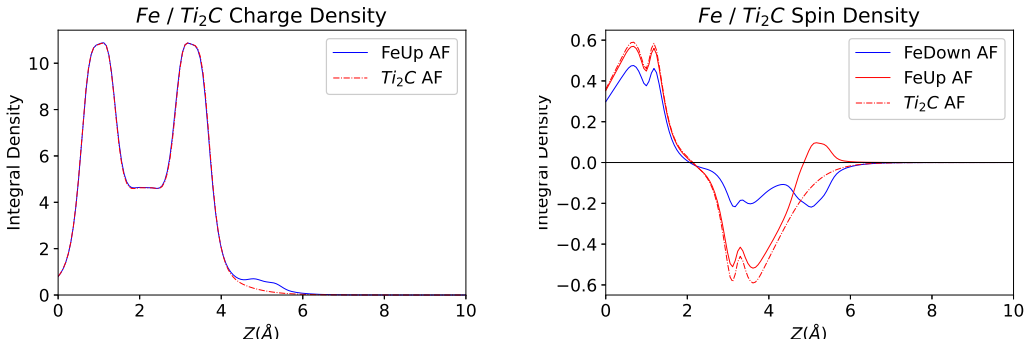

(A) (B)

FIGURE 7.14: The laterally averaged (a) charge and (b) spin densities of valence electrons (in units of $1/Å^3$) for the Fe/Ti_2C system.

To understand the source of the high adsorption energy of FePc on Ti_2C, the H_2Pc molecule was optimised on the same layer. Fig. 7.15 shows that two hydrogen atoms that substituted the iron atom are pushed off from the layer as an effect of the optimisation. The comparison of the geometric and energetic parameters (Table 7.9) shows that the adsorption energies of the H_2Pc and FePc on the layer are similar and the adsorption energy is not additive. The adsorption is mostly caused by adhesion of the Pc ligand to the Ti metallic layer rather than by adhesion of the iron atom.

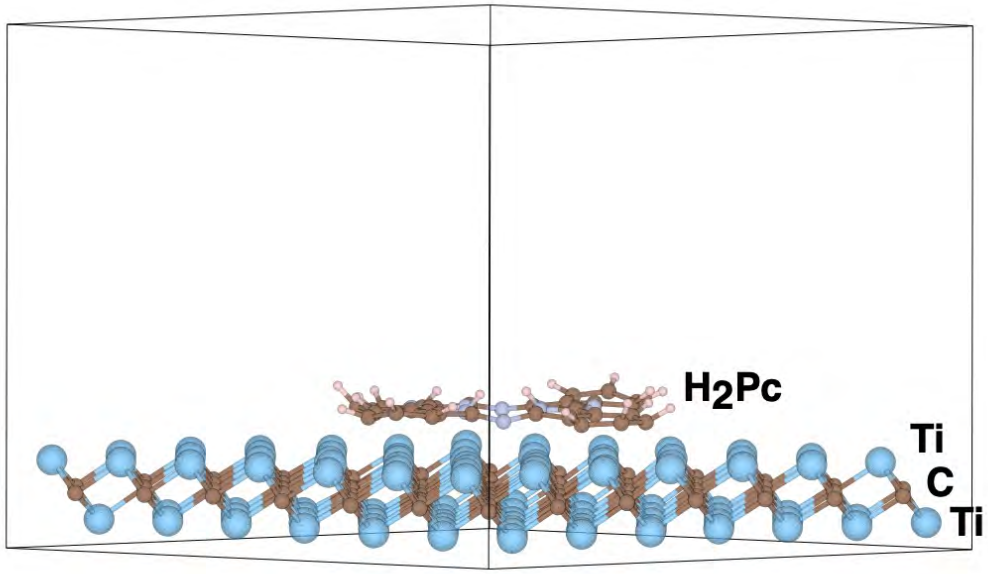

FIGURE 7.15: Side view of the H_2Pc/Ti_2C hybrid system.

	E_a, eV	Pc - Ti_2C dist, Å	Fe - Ti_2C dist, Å
H_2Pc/Ti_2C AF	-21.75	2.02	—
Fe/Ti_2C	-4.02	—	1,83 FeUp and 1,77 FeDown
FePc/Ti_2C	-21.88	2.09	2.03

TABLE 7.9: Comparison of energetic and geometric characteristics of H_2Pc, Fe and FePc on Ti_2C layer.

Chapter 8

Summary

The work done is quite pioneering. For the first time, the interaction of a TMPc molecule with a two-dimensional substrate has been studied using multiconfigurational methods of quantum chemistry. So far, our computational capabilities allow using only a limited area of the substrate's surface. In our case, we replaced the graphene surface with a small pyrene molecule. However, such a limited representation is sufficient to cover the area under the active Fe-N_4 centre of TMPc.

Calculations of the spin-polarised FePc molecule on the two-dimensional magnetic MXene material were also carried out. Our computational analysis showed the existence of several metastable magnetic configurations of this system. Such studies are still difficult to replicate experimentally, but our model shows which perspectives are open after developing studies with a pure non-functionalized MXene layer.

In the following subsections, the results obtained in this thesis are summarised in more detail, as well as further prospects for the study.

8.1 FePc/Graphene Hybrid System - Conclusions

- The interaction between the FePc molecule and the graphene substrate has been studied. The presence of FePc on the graphene layer does not significantly change the properties of both FePc and graphene despite their good van der Waals connection. The molecule on the top of the graphene layer does not open the band gap and the FePc iron *d*-shell does not significantly change its distribution in the FePc/Graphene hybrid system.

- Cluster representation of the graphene surface in the FePc/Graphene complex reproduces the results of the periodic model quite well. When using similar DFT parameters in the two models, the geometric and energy parameters differ insignificantly.

- The model with the pyrene molecule instead of the graphene sheet shows really similar geometry in the vicinity of the FePc's iron atom and it could be used in demanding multireference calculations.

- The presence of the Stone-Wales defect in graphene and pyrene barely changes the FePc adsorption parameters and the iron d-shell distribution. Previously,[40] it was found that the adsorption energy with the Stone-Wales defect differs by 6% for ZnPc and 10% for CuPc. Our suggestion is that the difference really depends on the calculation method and chosen DFT parameters.

- FePc/Pyrene complexes with B, N-doping and SW-B, SW-N combined defects have a really small energy difference between states with different multiplicities around the ground state. It was found, that the ground state is unstable and

the spin state of the system is subject to thermal fluctuations. Taking that into account, our results match the previous investigation.[38] While there were found only ground states of systems because of the one Slater determinant restriction, the behaviour of systems near the ground state was not taken into account. This restriction has been overcome in our studies by using multireference methods of calculation.

- On the contrary, the multireference analysis shows that FePc/Pyrene complexes with S-doping and combined SW-S defects have a big first excitation frequency. The FePc ground state and the ground state of the whole systems are not triplets but singlets, these defects make the complexes non-magnetic. The presence of the sulphur atom in graphene also sufficiently increases the FePc-graphene adsorption energy and the sulphur atom moves out of the graphene plane. The defects crucially change the morphology of the FePc/Graphene hybrid system; they modify the magnetic moment of the system, its geometry, and energetics parameters which should be clearly visible in experiments.

8.2 FePc/Ti_2C Hybrid System - Conclusions

- The early stage study of a TMPc molecule on a magnetic MXene layer has been made in the framework of the DFT theory. This investigation of the FePc/Ti_2C hybrid system can serve as a starting point for other similar studies of organometallic molecules on MXene layers.

- FePc adsorption to Ti_2C is much stronger compared to other 2D materials, such as MoS_2 and graphene.[34] Adsorption is no longer determined by the physical van der Waals interaction, but by chemical bonds between the carbon rings and the titanium surface. The iron atom makes a small contribution to adsorption.

- The exchange energy E_{ex}, *i.e.* the energy difference between the cases with the same initial Ti_2C magnetisation and different orientation of the iron atom in the FePc molecule, is 283 meV for the ferromagnetic case, 9 meV for the antiferromagnetic case, and 0.6 meV for the antiferromagnetic case with the molecule in the excited state. For the iron atom on the antiferromagnetic Ti_2C layer with the same supercell size, it is equal to 430 meV. The special thing about FePc is that by changing the spin orientation, the molecular geometry does not change, while in Fe/Ti_2C the flip of the spin orientation of the iron atom is associated with the movement of the iron atom along the z-axis.

- The ferromagnetic interaction between the iron atom (and the iron atom in FePc) and the upper Ti layer in MXene was found. When spin polarisations of the upper Ti layer in Ti_2C and the Fe atom are co-directed, titanium atoms closest to the iron atom have a tendency to flip their spin polarisation.

- Big charge transfer (about 8.5 $\bar{e}$) from Ti_2C to FePc is observed in the hybrid system. Most of this charge is transferred to FePc carbon atoms while about 0.38 electron is transferred to the iron atom. For comparison, charge transfer from the gold layer to the VPc molecule is just 0.62 $\bar{e}$.[102]

8.3 Perspectives

The study of magnetic molecules with an active FeN_4 centre on various surfaces is a fairly popular and versatile topic. We are sure that many more studies will be published, which will also develop further our research.

Our attempt to use multireference methods for systems consisting of the FePc molecule and the graphene surface shows that it is possible to study excited states of such hybrid systems on a high level of theory. The amount of RAM that we could use was limited, and our model is as good as it could be in such bounds. Better computational capabilities will make it possible to calculate similar structures with a more accurate basis set, as well as to increase the area of the graphene cluster.

Our work was rather devoted to studying the effect of graphene defects on the system, and we considered the system with only an iron atom at the centre of phthalocyanine. However, other transition metals deserve attention as well. In addition, there are many more graphene defects[121] whose influence is worth studying. Most of them cannot be reproduced on a pyrene molecule, so for this it is necessary to increase the area of the graphene cluster.

The study of the magnetic interaction of FePc with the Ti_2C layer also could be expanded on other TMPc molecules and MXene layers. The potential for MXene in the field of magnetic devices could be vast, while the research of magnetic hybrid structures with the MXene layer has just begun.

Our study can be improved if spin non-collinearity would be taken into account. We made an attempt to do it, but the results converged only in the case when there was one iron atom per MXene primitive cell, meaning full coverage of Ti layer by iron. In this case, taking into account the non-collinearity of spins does not provide any additional information, since as a result all the spins were directed along the z-axis. However, at lower iron concentrations on the surface, the picture may change.

Functionalised MXenes are of specific interest because such TMPc/MXene hybrid systems can be also studied experimentally.[26] While MXenes saturated with atmospheric functional groups usually do not possess magnetic order, they are of high interest as a fuel cell compound. It would be good to analyse both the interaction of the TMPc molecule with the functionalised MXene material and model such a system as a catalyst for redox reactions.

Bibliography

[1] Shubo Zhang. "Review of Modern Field Effect Transistor Technologies for Scaling". In: *Journal of Physics: Conference Series*. Vol. 1617. 1. IOP Publishing. 2020, p. 012054.

[2] George Christou et al. "Single-Molecule Magnets". In: *MRS Bulletin* 25.11 (2000), pp. 66–71.

[3] RP Linstead. "212. Phthalocyanines. Part I. A new type of synthetic colouring matters". In: *Journal of the Chemical Society (Resumed)* (1934), pp. 1016–1017.

[4] Keryn Lian et al. "Printed flexible memory devices using copper phthalocyanine". In: *Materials Science and Engineering: B* 167.1 (2010), pp. 12–16.

[5] C Barraud et al. "Phthalocyanine based molecular spintronic devices". In: *Dalton Transactions* 45.42 (2016), pp. 16694–16699.

[6] Marc Warner et al. "Potential for spin-based information processing in a thin-film molecular semiconductor". In: *Nature* 503.7477 (2013), pp. 504–508.

[7] Masamitsu Kaneko et al. "Fast response of organic photodetectors utilizing multilayered metal-phthalocyanine thin films". In: *Japanese Journal of Applied Physics* 42.4S (2003), p. 2523.

[8] SM Tadayyon et al. "CuPc buffer layer role in OLED performance: a study of the interfacial band energies". In: *Organic Electronics* 5.4 (2004), pp. 157–166.

[9] Xuanye Leng et al. "Introduction to two-dimensional materials". In: *Molecular interactions on two-dimensional materials*. World Scientific, 2022, pp. 1–41.

[10] Kostya S Novoselov et al. "Electric field effect in atomically thin carbon films". In: *science* 306.5696 (2004), pp. 666–669.

[11] Mohammed Yusuf et al. "A review on exfoliation, characterization, environmental and energy applications of graphene and graphene-based composites". In: *Advances in colloid and interface science* 273 (2019), p. 102036.

[12] Kian Ping Loh et al. "The chemistry of graphene". In: *Journal of Materials Chemistry* 20.12 (2010), pp. 2277–2289.

[13] Yuriy Dedkov et al. "Epitaxial graphene on metals". In: *Graphene Nanoelectronics*. Springer, 2011, pp. 189–234.

[14] Wataru Norimatsu and Michiko Kusunoki. "Epitaxial graphene on SiC {0001}: advances and perspectives". In: *Physical Chemistry Chemical Physics* 16.8 (2014), pp. 3501–3511.

[15] YI Zhang, Luyao Zhang, and Chongwu Zhou. "Review of chemical vapor deposition of graphene and related applications". In: *Accounts of chemical research* 46.10 (2013), pp. 2329–2339.

[16] Xiangping Chen, Lili Zhang, and Shanshan Chen. "Large area CVD growth of graphene". In: *Synthetic Metals* 210 (2015), pp. 95–108.

[17] Matthew J Allen, Vincent C Tung, and Richard B Kaner. "Honeycomb carbon: a review of graphene". In: *Chemical reviews* 110.1 (2010), pp. 132–145.

[18] Michael Naguib et al. "Two-dimensional nanocrystals produced by exfoliation of Ti_3AlC_2". In: *Advanced materials* 23.37 (2011), pp. 4248–4253.

[19] Jinbo Pang et al. "Applications of 2D MXenes in energy conversion and storage systems". In: *Chemical Society Reviews* 48.1 (2019), pp. 72–133.

[20] Zhongheng Fu et al. "Rational design of flexible two-dimensional MXenes with multiple functionalities". In: *Chemical Reviews* 119.23 (2019), pp. 11980–12031.

[21] Peng Lv, Yan-Li Li, and Jia-Fu Wang. "Monolayer Ti_2C MXene: Manipulating magnetic properties and electronic structures by an electric field". In: *Physical Chemistry Chemical Physics* 22.20 (2020), pp. 11266–11272.

[22] Jens Kügel et al. "Reversible magnetic switching of high-spin molecules on a giant Rashba surface". In: *npj Quantum Materials* 3.1 (2018), pp. 1–7.

[23] Sumanta Bhandary et al. "Graphene as a reversible spin manipulator of molecular magnets". In: *Physical review letters* 107.25 (2011), p. 257202.

[24] P Ferriani, S Heinze, and V Bellini. "Designing a molecular magnetic button based on 4d and 5d transition-metal phthalocyanines". In: *Scientific reports* 7.1 (2017), pp. 1–9.

[25] Brian CH Steele and Angelika Heinzel. "Materials for fuel-cell technologies". In: *Materials For Sustainable Energy: A Collection of Peer-Reviewed Research and Review Articles from Nature Publishing Group*. World Scientific, 2011, pp. 224–231.

[26] Zilan Li et al. "The marriage of the FeN_4 moiety and MXene boosts oxygen reduction catalysis: Fe 3d electron delocalization matters". In: *Advanced materials* 30.43 (2018), p. 1803220.

[27] Jong S Park and Dong Wook Chang. "Iron Phthalocyanine/Graphene Composites as Promising Electrocatalysts for the Oxygen Reduction Reaction". In: *Energies* 13.16 (2020), p. 4073.

[28] Joana MD Calmeiro, João PC Tomé, and Leandro MO Lourenço. "Supramolecular graphene–phthalocyanine assemblies for technological breakthroughs". In: *Journal of Materials Chemistry C* (2020).

[29] Dingling Yu and Xingquan He. "A novel iron(II) tetranitrophthalocyanine/graphene composite as the high-performance catalyst for the oxygen reduction reaction in an alkaline medium". In: *Applied Materials Today* 3 (2016), pp. 1–10.

[30] Rui-Xiang Wang et al. "Graphene-covered FePc as a model of the encapsulated type of catalyst for the oxygen reduction reaction". In: *Electrochemistry Communications* 112 (2020), p. 106670.

[31] Kejun Chen et al. "Iron phthalocyanine with coordination induced electronic localization to boost oxygen reduction reaction". In: *Nature communications* 11.1 (2020), pp. 1–8.

[32] Chenzhen Zhang et al. "Iron phthalocyanine and nitrogen-doped graphene composite as a novel non-precious catalyst for the oxygen reduction reaction". In: *Nanoscale* 4.23 (2012), pp. 7326–7329.

[33] Siqi Feng et al. "Phthalocyanine and metal phthalocyanines adsorbed on graphene: a density functional study". In: *The Journal of Physical Chemistry C* 123.27 (2019), pp. 16614–16620.

[34] Soumyajyoti Haldar et al. "Comparative study of electronic and magnetic properties of iron and cobalt phthalocyanine molecules physisorbed on two-dimensional MoS_2 and graphene". In: *Physical Review B* 98.8 (2018), p. 085440.

[35] Andrea Candini et al. "Ferromagnetic exchange coupling between Fe phthalocyanine and Ni (111) surface mediated by the extended states of graphene". In: *The Journal of Physical Chemistry C* 118.31 (2014), pp. 17670–17676.

[36] Bruno de la Torre et al. "Non-covalent control of spin-state in metal-organic complex by positioning on N-doped graphene". In: *Nature communications* 9.1 (2018), pp. 1–9.

[37] Yu Wang, Xiaoguang Li, and Jinlong Yang. "Electronic and magnetic properties of CoPc and FePc molecules on graphene: the substrate, defect, and hydrogen adsorption effects". In: *Physical Chemistry Chemical Physics* 21.10 (2019), pp. 5424–5434.

[38] Amrit Sarmah and Pavel Hobza. "Computational approach to understand the adsorption behavior of iron (II) phthalocyanine on the doped graphene surface". In: *The Journal of Physical Chemistry C* 123.11 (2019), pp. 6717–6724.

[39] AI Podlivaev and LA Openov. "Dynamics of the Stone-Wales defect in graphene". In: *Physics of the Solid State* 57.4 (2015), pp. 820–824.

[40] Carlos Uriel Mendoza-Domınguez and Vladimir A Basiuk. "Distortion and bonding strength of phthalocyanine molecules adsorbed on topological defects in graphene". In: *Materials Chemistry and Physics* 271 (2021), p. 124963.

[41] Sumanta Bhandary, Olle Eriksson, and Biplab Sanyal. "Defect controlled magnetism in FeP/graphene/Ni (111)". In: *Scientific reports* 3.1 (2013), pp. 1–6.

[42] Fenghe Duan et al. "Construction of the 0D/2D heterojunction of $Ti_{3a}C_2T_2$ MXene nanosheets and iron phthalocyanine quantum dots for the impedimetric aptasensing of microRNA-155". In: *Sensors and Actuators B: Chemical* 310 (2020), p. 127844.

[43] Yijing Gao et al. "Functionalization Ti_3C_2 MXene by the adsorption or substitution of single metal atom". In: *Applied Surface Science* 465 (2019), pp. 911–918.

[44] Hedda Oschinski, Ángel Morales-Garcıa, and Francesc Illas. "Interaction of First Row Transition Metals with M_2C (M= Ti, Zr, Hf, V, Nb, Ta, Cr, Mo, and W) MXenes: A Quest for Single-Atom Catalysts". In: *The Journal of Physical Chemistry C* 125.4 (2021), pp. 2477–2484.

[45] Bin Huang et al. "Single atom-supported MXene: how single-atomic-site catalysts tune the high activity and selectivity of electrochemical nitrogen fixation". In: *Journal of Materials Chemistry A* 7.48 (2019), pp. 27620–27631.

[46] Di Zhao et al. "MXene (Ti_3C_2) vacancy-confined single-atom catalyst for efficient functionalization of CO_2". In: *Journal of the American Chemical Society* 141.9 (2019), pp. 4086–4093.

[47] Qing Wan, Shunning Li, and Jian-Bo Liu. "First-principle study of Li-ion storage of functionalized Ti2C monolayer with vacancies". In: *ACS applied materials & interfaces* 10.7 (2018), pp. 6369–6377.

[48] Jens Brede et al. "Atomic-Scale Spintronics". In: *Handbook of Spintronics*. Ed. by Yongbing Xu, David D. Awschalom, and Junsaku Nitta. Dordrecht: Springer Netherlands, 2016, pp. 757–784. ISBN: 978-94-007-6892-5.

[49] Alexander A Khajetoorians et al. "Detecting excitation and magnetization of individual dopants in a semiconductor". In: *Nature* 467.7319 (2010), pp. 1084–1087.

[50] Bruno Chilian et al. "Experimental variation and theoretical analysis of the inelastic contribution to atomic spin excitation spectroscopy". In: *Physical Review B* 83.19 (2011), p. 195431.

[51] Michael Schüler et al. "Functionalizing Fe adatoms on Cu (001) as a nano-electromechanical system". In: *New Journal of Physics* 19.7 (2017), p. 073016.

[52] Bence Lazarovits et al. "Magnetic properties of finite Fe chains at fcc Cu (001) and Cu (111) surfaces". In: *Physical Review B* 68.2 (2003), p. 024433.

[53] Florian Ellinger, Cesare Franchini, and Valerio Bellini. "Magnetic 3d adatoms on free-standing and Ni (111)-supported graphene". In: *Physical Review Materials* 5.1 (2021), p. 014406.

[54] Piotr Błoński and Jürgen Hafner. "Density-functional theory of the magnetic anisotropy of nanostructures: an assessment of different approximations". In: *Journal of physics: Condensed matter* 21.42 (2009), p. 426001.

[55] Corina Etz et al. "Magnetic properties of single atoms of Fe and Co on Ir (111) and Pt (111)". In: *Physical Review B* 77.18 (2008), p. 184425.

[56] T Balashov et al. "Magnetic anisotropy and magnetization dynamics of individual atoms and clusters of Fe and Co on Pt (111)". In: *Physical review letters* 102.25 (2009), p. 257203.

[57] Brian Kiraly et al. "An orbitally derived single-atom magnetic memory". In: *Nature communications* 9.1 (2018), pp. 1–8.

[58] Fabian D Natterer et al. "Reading and writing single-atom magnets". In: *Nature* 543.7644 (2017), pp. 226–228.

[59] Jianzhuang Jiang. *Functional phthalocyanine molecular materials*. Vol. 135. Springer, 2010.

[60] Daniel S Levine et al. "CASSCF with extremely large active spaces using the adaptive sampling configuration interaction method". In: *Journal of chemical theory and computation* 16.4 (2020), pp. 2340–2354.

[61] Alexandra Siklitskaya et al. "Lerf–Klinowski-type models of graphene oxide and reduced graphene oxide are robust in analyzing non-covalent functionalization with porphyrins". In: *Scientific reports* 11.1 (2021), pp. 1–14.

[62] Qingxiao Zhou et al. "Effect of coexistence of defect and dopant on the quantum capacitance of graphene-based supercapacitors electrodes". In: *Applied Surface Science* 510 (2020), p. 145448.

[63] E. Schrödinger. "An Undulatory Theory of the Mechanics of Atoms and Molecules". In: *Physical Review* 28.6 (Dec. 1, 1926), pp. 1049–1070.

[64] Max Born and Robert Oppenheimer. "Zur quantentheorie der molekeln". In: *Annalen der physik* 389.20 (1927), pp. 457–484.

[65] J. C. Slater. "The Self Consistent Field and the Structure of Atoms". In: *Physical Review* 32.3 (Sept. 1, 1928), pp. 339–348.

[66] D. R. Hartree. "The Wave Mechanics of an Atom with a Non-Coulomb Central Field. Part II. Some Results and Discussion". In: *Mathematical Proceedings of the Cambridge Philosophical Society* 24.1 (Jan. 1928), pp. 111–132. ISSN: 1469-8064, 0305-0041.

[67] V. Fock. "Näherungsmethode zur Lösung des quantenmechanischen Mehrkörperproblems". In: *Zeitschrift für Physik* 61.1 (Jan. 1, 1930), pp. 126–148. ISSN: 0044-3328.

[68] B. Roos. "A New Method for Large-Scale Cl Calculations". In: *Chemical Physics Letters* 15.2 (Aug. 1, 1972), pp. 153–159. ISSN: 0009-2614.

[69] Per Siegbahn et al. "A Comparison of the Super-CI and the Newton-Raphson Scheme in the Complete Active Space SCF Method". In: *Physica Scripta* 21.3-4 (1980), pp. 323–327. ISSN: 1402-4896.

[70] Björn O. Roos, Peter R. Taylor, and Per E. M. Sigbahn. "A Complete Active Space SCF Method (CASSCF) Using a Density Matrix Formulated Super-CI Approach". In: *Chemical Physics* 48.2 (May 15, 1980), pp. 157–173. ISSN: 0301-0104.

[71] Per E. M. Siegbahn et al. "The Complete Active Space SCF (CASSCF) Method in a Newton–Raphson Formulation with Application to the HNO Molecule". In: *The Journal of Chemical Physics* 74.4 (Feb. 15, 1981), pp. 2384–2396. ISSN: 0021-9606.

[72] C. Angeli et al. "Introduction of N-Electron Valence States for Multireference Perturbation Theory". In: *The Journal of Chemical Physics* 114.23 (June 15, 2001), pp. 10252–10264. ISSN: 0021-9606.

[73] P. Hohenberg and W. Kohn. "Inhomogeneous Electron Gas". In: *Physical Review* 136 (3B Nov. 9, 1964), B864–B871.

[74] Mel Levy. "Elementary Concepts in Density Functional Theory". In: *Theoretical and Computational Chemistry*. Ed. by J. M. Seminario. Vol. 4. Recent Developments and Applications of Modern Density Functional Theory. Elsevier, Jan. 1, 1996, pp. 3–24.

[75] W. Kohn and L. J. Sham. "Self-Consistent Equations Including Exchange and Correlation Effects". In: *Physical Review* 140 (4A Nov. 15, 1965), A1133–A1138.

[76] AI Liechtenstein, Vladimir I Anisimov, and Jan Zaanen. "Density-functional theory and strong interactions: Orbital ordering in Mott-Hubbard insulators". In: *Physical Review B* 52.8 (1995), R5467.

[77] Matteo Cococcioni and Stefano de Gironcoli. "Linear Response Approach to the Calculation of the Effective Interaction Parameters in the LDA+U Method". In: *Physical Review B* 71.3 (Jan. 18, 2005), p. 035105.

[78] DR Hamann, M Schlüter, and C Chiang. "Norm-conserving pseudopotentials". In: *Physical Review Letters* 43.20 (1979), p. 1494.

[79] David Vanderbilt. "Soft self-consistent pseudopotentials in a generalized eigenvalue formalism". In: *Physical review B* 41.11 (1990), p. 7892.

[80] Peter E Blöchl. "Projector augmented-wave method". In: *Physical review B* 50.24 (1994), p. 17953.

[81] Rodney J Bartlett and Monika Musiał. "Coupled-cluster theory in quantum chemistry". In: *Reviews of Modern Physics* 79.1 (2007), p. 291.

[82] Max Dion et al. "Van der Waals density functional for general geometries". In: *Physical review letters* 92.24 (2004), p. 246401.

[83] Kyuho Lee et al. "Higher-accuracy van der Waals density functional". In: *Physical Review B* 82.8 (2010), p. 081101.

[84] Yan Zhao and Donald G Truhlar. "A new local density functional for main-group thermochemistry, transition metal bonding, thermochemical kinetics, and noncovalent interactions". In: *The Journal of chemical physics* 125.19 (2006), p. 194101.

[85] Stefan Grimme et al. "A consistent and accurate ab initio parametrization of density functional dispersion correction (DFT-D) for the 94 elements H-Pu". In: *The Journal of chemical physics* 132.15 (2010), p. 154104.

[86] Axel D Becke and Erin R Johnson. "Exchange-hole dipole moment and the dispersion interaction revisited". In: *The Journal of chemical physics* 127.15 (2007), p. 154108.

[87] Alexandre Tkatchenko and Matthias Scheffler. "Accurate molecular van der Waals interactions from ground-state electron density and free-atom reference data". In: *Physical review letters* 102.7 (2009), p. 073005.

[88] Paolo Giannozzi et al. "QUANTUM ESPRESSO: a modular and open-source software project for quantum simulations of materials". In: *Journal of physics: Condensed matter* 21.39 (2009), p. 395502.

[89] David C Langreth and MJ Mehl. "Beyond the local-density approximation in calculations of ground-state electronic properties". In: *Physical Review B* 28.4 (1983), p. 1809.

[90] John P Perdew, Kieron Burke, and Matthias Ernzerhof. "Generalized gradient approximation made simple". In: *Physical review letters* 77.18 (1996), p. 3865.

[91] Vladimir I Anisimov, Ferdi Aryasetiawan, and AI Lichtenstein. "First-principles calculations of the electronic structure and spectra of strongly correlated systems: the LDA+ U method". In: *Journal of Physics: Condensed Matter* 9.4 (1997), p. 767.

[92] Iulia Emilia Brumboiu et al. "Ligand Effects on the Linear Response Hubbard U: The Case of Transition Metal Phthalocyanines". In: *The Journal of Physical Chemistry A* 123.14 (2019), pp. 3214–3222.

[93] Frank Neese. "The ORCA program system". In: *Wiley Interdisciplinary Reviews: Computational Molecular Science* 2.1 (2012), pp. 73–78.

[94] Frank Neese. "Software update: the ORCA program system, version 4.0". In: *Wiley Interdisciplinary Reviews: Computational Molecular Science* 8.1 (2018), e1327.

[95] Florian Weigend and Reinhart Ahlrichs. "Balanced basis sets of split valence, triple zeta valence and quadruple zeta valence quality for H to Rn: Design and assessment of accuracy". In: *Physical Chemistry Chemical Physics* 7.18 (2005), pp. 3297–3305.

[96] Holger Kruse and Stefan Grimme. "A geometrical correction for the inter- and intra-molecular basis set superposition error in Hartree-Fock and density functional theory calculations for large systems". In: *The Journal of chemical physics* 136.15 (2012), 04B613.

[97] Chiara Ricca et al. "B, N-Codoped graphene as catalyst for the oxygen reduction reaction: Insights from periodic and cluster DFT calculations". In: *Journal of computational chemistry* 39.11 (2018), pp. 637–647.

[98] Frank Neese et al. "Efficient, approximate and parallel Hartree–Fock and hybrid DFT calculations. A 'chain-of-spheres' algorithm for the Hartree–Fock exchange". In: *Chemical Physics* 356.1-3 (2009), pp. 98–109.

[99] Celestino Angeli et al. "Introduction of n-electron valence states for multireference perturbation theory". In: *The Journal of Chemical Physics* 114.23 (2001), pp. 10252–10264.

[100] Andrea Dal Corso. "Pseudopotentials periodic table: From H to Pu". In: *Computational Materials Science* 95 (2014), pp. 337–350.

[101] Richard FW Bader. "A quantum theory of molecular structure and its applications". In: *Chemical Reviews* 91.5 (1991), pp. 893–928.

[102] Manel Mabrouk and Jacek A Majewski. "Stability, electronic structure, and magnetic moment of Vanadium phthalocyanine grafted to the Au (111) surface". In: *Computational and Theoretical Chemistry* (2021), p. 113319.

[103] Tom Ichibha et al. "New insight into the ground state of FePc: A diffusion monte carlo study". In: *Scientific reports* 7.1 (2017), pp. 1–6.

[104] Dario Campisi and Alessandra Candian. "Do defects in PAHs promote catalytic activity in space? Stone–Wales pyrene as a test case". In: *Physical Chemistry Chemical Physics* 22.12 (2020), pp. 6738–6748.

[105] Xiuguang Shi et al. "NBN unit functionalized pyrene derivatives with different photophysical and anti-counterfeiting properties". In: *Journal of Photochemistry and Photobiology A: Chemistry* 412 (2021), p. 113206.

[106] Zhiqiang Liu and Todd B. Marder. "BN versus CC: How Similar Are They?" In: *Angewandte Chemie International Edition* 47.2 (2008), pp. 242–244.

[107] AI Podlivaev and LA Openov. "Out-of-plane path of the Stone–Wales transformation in graphene". In: *Physics Letters A* 379.30-31 (2015), pp. 1757–1761.

[108] LA Openov and AI Podlivaev. "Interaction of the Stone-Wales defects in graphene". In: *Physics of the Solid State* 57.7 (2015), pp. 1477–1481.

[109] Zhansheng Lu et al. "Sulfur doped graphene as a promising metal-free electrocatalyst for oxygen reduction reaction: a DFT-D study". In: *RSC advances* 7.33 (2017), pp. 20398–20405.

[110] A Johll Harman and Low Raelynn. "Density functional theory study of metal adatoms at or near a stone-wales defect in graphene". In: *Procedia Engineering* 93 (2014), pp. 2–7.

[111] LS Panchakarla et al. "Synthesis, structure, and properties of boron-and nitrogen-doped graphene". In: *Advanced Materials* 21.46 (2009), pp. 4726–4730.

[112] Dacheng Wei et al. "Synthesis of N-doped graphene by chemical vapor deposition and its electrical properties". In: *Nano letters* 9.5 (2009), pp. 1752–1758.

[113] Anubhav Jain et al. "Commentary: The Materials Project: A materials genome approach to accelerating materials innovation". In: *APL Materials* 1.1 (2013), p. 011002. ISSN: 2166532X.

[114] Xiaofang Lai et al. "Observation of superconductivity in tetragonal FeS". In: *Journal of the American Chemical Society* 137 (2015), pp. 10148–10151.

[115] E.F. Bertaut, P. Burlet, and J. Chappert. "Sur l'absence d'ordre magnetique dans la forme quadratique de FeS". In: *Solid State Communications* 3 (1965), pp. 335–338.

[116] K.K. Kwon et al. "Magnetic ordering in tetragonal FeS: evidence for strong itinerant spin fluctuations". In: *Physical Review, Serie 3. B - Condensed Matter (18,1978-)* 83 (2011), pp. 064402-1-064402–7.

[117] M. Uda. "The structure of tetragonal FeS". In: *Zeitschrift fuer Anorganische und Allgemeine Chemie (1950) (DE)* 361 (1968), pp. 94–98.

[118] R.A. Berner. "Tetragonal iron sulfide". In: *Science* 137 (1962), pp. 669–669.

[119] A.N. Kolmogorov et al. "New superconducting and semiconducting Fe-B compounds predicted with an ab initio evolutionary search". In: *Physical Review Letters* 105 (2010), pp. 217003-1-217003–4.

[120] Per-Olov Löwdin. "On the non-orthogonality problem connected with the use of atomic wave functions in the theory of molecules and crystals". In: *The Journal of Chemical Physics* 18.3 (1950), pp. 365–375.

[121] Wenchao Tian et al. "A review on lattice defects in graphene: types, generation, effects and regulation". In: *Micromachines* 8.5 (2017), p. 163.